UNICAMP

UNIVERSIDADE ESTADUAL DE CAMPINAS
Faculdade de Engenharia Mecânica

Renato Fuzaro Miotto

Investigation of dynamic stall through high fidelity numerical simulations and data-driven techniques

Investigação de estol dinâmico através de simulações numéricas de alta fidelidade e técnicas orientadas por dados

CAMPINAS
2022

RENATO FUZARO MIOTTO

Investigation of dynamic stall through high fidelity numerical simulations and data-driven techniques

Investigação de estol dinâmico através de simulações numéricas de alta fidelidade e técnicas orientadas por dados

Thesis presented to the School of Mechanical Engineering of the University of Campinas in partial fulfillment of the requirements for the degree of Doctor in Mechanical Engineering, in the area of Thermal and Fluids.

Tese apresentada à Faculdade de Engenharia Mecânica da Universidade Estadual de Campinas como parte dos requisitos exigidos para a obtenção do título de Doutor em Engenharia Mecânica, na área de Térmica e Fluidos.

Orientador: William Roberto Wolf

ESTE EXEMPLAR CORRESPONDE À VERSÃO FINAL DA TESE DEFENDIDA PELO ALUNO RENATO FUZARO MIOTTO, E ORIENTADA PELO PROF. DR. WILLIAM ROBERTO WOLF.

Assinatura do Orientador

____

Campinas
2022

Ficha catalográfica
Universidade Estadual de Campinas
Biblioteca da Área de Engenharia e Arquitetura
Elizangela Aparecida dos Santos Souza - CRB 8/8098

M669i

Miotto, Renato Fuzaro, 1991-
Investigation of dynamic stall through high fidelity numerical simulations and data-driven techniques / Renato Fuzaro Miotto. – Campinas, SP : [s.n.], 2022.

Orientador: William Roberto Wolf.
Tese (doutorado) – Universidade Estadual de Campinas, Faculdade de Engenharia Mecânica.

1. Aerodinâmica. 2. Fluidodinâmica computacional. 3. Análise modal. 4. Redes neurais convolucionais. 5. Helicopteros - Aerodinâmica. I. Wolf, William Roberto, 1980-. II. Universidade Estadual de Campinas. Faculdade de Engenharia Mecânica. III. Título.

Informações para Biblioteca Digital

Título em outro idioma: Investigação de estol dinâmico através de simulações numéricas de alta fidelidade e técnicas orientadas por dados
Palavras-chave em inglês:
Aerodynamics
Computational fluid dynamics
Modal analysis
Convolutional neural networks
Helicopter aerodynamics
Área de concentração: Térmica e Fluídos
Titulação: Doutor em Engenharia Mecânica
Banca examinadora:
William Roberto Wolf [Orientador]
Bruno Souza Carmo
Rafael dos Santos Gioria
Daniel Sampaio Souza
Elmer Mateus Gennaro
Data de defesa: 16-08-2022
Programa de Pós-Graduação: Engenharia Mecânica

Identificação e informações acadêmicas do(a) aluno(a)
- ORCID do autor: 0000-0002-7813-8873
- Currículo Lattes do autor: http://lattes.cnpq.br/3760865706899923

UNIVERSIDADE ESTADUAL DE CAMPINAS
FACULDADE DE ENGENHARIA MECÂNICA

TESE DE DOUTORADO ACADÊMICO

Investigation of dynamic stall through high fidelity numerical simulations and data-driven techniques

Investigação de estol dinâmico através de simulações numéricas de alta fidelidade e técnicas orientadas por dados

Autor: Renato Fuzaro Miotto

Orientador: William Roberto Wolf

A Banca Examinadora composta pelos membros abaixo aprovou esta tese:

Prof. Dr. William Roberto Wolf
Universidade Estadual de Campinas

Prof. Dr. Bruno Souza Carmo
Universidade de São Paulo

Prof. Dr. Rafael dos Santos Gioria
Universidade de São Paulo

Prof. Dr. Daniel Sampaio Souza
Universidade Estadual Paulista

Prof. Dr. Elmer Mateus Gennaro
Universidade Estadual Paulista

A Ata da defesa com as respectivas assinaturas dos membros encontra-se no processo de vida acadêmica do aluno.

Campinas, 16 de Agosto de 2022.

Acknowledgments

My dearest thanks-for-everything to my family.

I am eternally grateful to my advisor Prof. William Wolf for the infinite hours devoted to all his students, including me. His professionalism and guidance are values that I will carry along in my scientific career.

A special thanks to my friends and colleagues in UNICAMP during all these years. Cristiano Pimenta (Peppa), Tulio Ricciardi, Diogo Pitz, Luiz Schiavo, Hugo Lui (Slui), Victor Zucatti (Vitão), Gabriel Nogueira (Bibi), Jean Ribeiro, Brener d'Lelis and Lucas Mascagni will always be remembered for all their help and fellowship within the laboratory.

I am sincerely grateful to Prof. Datta Gaitonde for his mentoring and support during my stay at The Ohio State University. Special thanks to Rajesh Ranjan, S. Unnikrishnan, Vilas Shinde, Chitrarth Prasad, Parshwanath Doshi, Surya Chakrabarti and Hemanth Goparaju for the fruitful work-related discussions.

I thank the members of my thesis committee, Profs. Bruno Souza Carmo, Rafael dos Santos Gioria, Daniel Sampaio Souza and Elmer Mateus Gennaro for their time and insights regarding this work. I also wish to thank Profs. Daniel Sampaio Souza and Elmer Mateus Gennaro for their time and contribution in the qualifying exam.

I acknowledge CENAPAD-SP (project 551), CEPID-CeMEAI (cluster Euler), LNCC (project SimTurb, cluster Santos Dumont) and the Ohio Supercomputer Center for providing the computational resources necessary to accomplish this research. This work was supported by Fundação de Amparo à Pesquisa do Estado de São Paulo, FAPESP, under grants No. 2013/08293-7, 2017/10795-1, 2019/02335-6 and 2021/06448-0, and by Conselho Nacional de Desenvolvimento Científico e Tecnológico, CNPq, under grants No. 407842/2018-7 and 308017/2021-8.

Resumo

O início e a evolução do vórtice de estol dinâmico (DSV, do inglês *dynamic stall vortex*) são analisados por meio de simulações de grandes escalas de um aerofólio SD7003 em movimento de *plunge* periódico em um escoamento com número de Reynolds $\mathrm{Re} = 6 \times 10^4$. Interações entre as instabilidades de Kelvin-Helmholtz que se propagam a montante e uma camada de cisalhamento formada no bordo de ataque do aerofólio desencadeiam a separação do escoamento. A primeira instabilidade parece estar relacionada com as ondas acústicas geradas no bordo de fuga devido ao desprendimento inicial de vórtices. Dois números de Mach do escoamento livre ($M_\infty = 0.1$ e 0.4) são empregados para examinar as diferenças do escoamento devido às variações de compressibilidade. A existência de um tempo comum para as perturbações acústicas em ambos os escoamentos sugere uma possível invariância do número de Mach para o nascimento da instabilidade de Kelvin-Helmholtz. O aumento da compressibilidade, no entanto, induz flutuações mais precoces na direção da envergadura, maior tridimensionalidade do escoamento e um DSV mais fraco e difuso, que é formado mais a jusante do bordo de ataque e tem menor tempo de residência. Para melhor caracterizar o início do DSV, dois critérios empíricos são avaliados: o parâmetro de sucção do bordo de ataque (LESP, do inglês *leading edge suction paramenter*) e a altura da camada de cisalhamento normal à corda. Os resultados demonstram uma maior robustez deste último parâmetro com relação às variações do número de Mach. Uma decomposição modal, realizada tanto com a decomposição em modos dinâmicos (DMD) clássica quanto com sua variante multi-resolução (mrDMD), destaca as principais tendências e demonstra a capacidade do mrDMD de extrair estruturas do escoamento fisicamente significativas relacionadas ao início do estol. Essa caracterização detalhada da camada de cisalhamento pode ser usada para uma exploração sistemática de estratégias de controle de escoamentos para aerofólios não-estacionários.

No presente trabalho, também realizamos simulações de grandes escalas (LES) para investigar a equivalência *pitch-plunge* de um aerofólio SD7003 submetido a movimentos de rampa constantes para um número de Reynolds $\mathrm{Re} = 6 \times 10^4$. A equivalência é construída com base no ângulo de ataque efetivo geométrico de acordo com a teoria de aerofólios finos quasi-estacionários. Duas taxas de descida (ou *pitch up*/arfagem) são analisadas para diferentes números de Mach para se investigar os efeitos da compressibilidade na evolução do DSV. Durante o início do DSV e seu transporte ao longo da superfície do aerofólio, notáveis semelhanças são encontradas entre *pitch* e *plunge* em termos de topologia do escoamento, coeficientes aerodinâmicos e assinaturas de pressão na parede e coeficientes de atrit. No entanto, essa semelhanças cessam em condições de alto carregamento à medida que o DSV se torna mais suscetível às peculiaridades do movimento do aerofólio, manifestado por diferentes vórtices de borda de fuga (TEVs, do inglês *trailing-edge vortices*). O emprego uma correção para o efeito de cambagem aparente induzida por rotação presente no caso de pitching, que resulta da teoria de aerofólio fino quasi-estacionário, melhora a concordância entre *pitch* e *plunge*, no entanto, não é suficiente assimilar seus sistemas de ponta de fuga díspares. Os resultados também demonstram que o ângulo limite no qual a equivalência *pitch-plunge* permanece válida diminui para números de Mach mais altos.

Por fim, propomos um *framework* em que os dados de simulações numéricas são aproveitados para extrair informações relevantes de visualizações experimentais. Para tanto, o bloco convolucional de uma rede InceptionV3 pré-treinada é utilizado para construir um modelo de regressão que vincula o mapa de coeficiente de pressão aos coeficientes aerodinâmicos do aerofólio. A rede neural convolucional (CNN, do inglês *Convolutional Neural Network*) resultante interpreta corretamente os atributos presentes na imagem do escoamento usada como entrada. Aspectos da generalização do modelo são discutidos e o desempenho do campo de velocidade como entrada para o modelo é avaliado. Os resultados mostram que a pressão é preferível à velocidade quando se trata de construir nosso modelo de regressão. No entanto, demonstramos que a velocidade pode ser usada para sintetizar qualquer quantidade física correspondente através de uma abordagem de tradução de imagem para imagem. Aqui, o mapeamento entre o campo de coeficiente de velocidade e pressão é usado como exemplo.

Palavras-chave: Estol dinâmico, dinâmica dos fluidos computacional, decomposição modal de escoamentos, redes neurais convolucionais.

Abstract

The onset and evolution of the dynamic stall vortex (DSV) are analyzed by means of large eddy simulations (LES) of an SD7003 airfoil undergoing periodic plunging motion in a transitional Reynolds number flow ($\mathrm{Re} = 6 \times 10^4$). Interactions between upstream propagating Kelvin-Helmholtz instabilities and a shear layer formed at the leading edge trigger flow separation. The former appear to be related to acoustic waves scattered at the trailing edge due to initial vortex shedding. Two freestream Mach numbers ($M_\infty = 0.1$ and 0.4) are employed to examine the flow differences due to compressibility variations. The existence of a common timing for the acoustic perturbations in both flows suggests a possible Mach number invariance for the birth of the Kelvin-Helmholtz instability. Increasing compressiblity, however, induces earlier spanwise fluctuations, higher flow three-dimensionality and a weaker and more diffuse DSV, which is formed further downstream of the leading edge and has lower residency time. In order to better characterize the onset of the DSV, two empirical criteria are assessed: the leading edge suction parameter (LESP) and the chord-normal shear layer height. Results demonstrate a higher robustness of the latter with respect to Mach number variations. Modal decomposition, performed with both the classical dynamic mode decomposition (DMD) and its multi-resolution variant (mrDMD), highlights key trends and demonstrates the capacity of the mrDMD to extract physically meaningful flow structures related to the stall onset. Such detailed characterization of the shear layer can be used for a systematic exploration of flow control strategies for unsteady airfoils.

In the present work, we also perform LES to investigate the pitch-plunge equivalence of an SD7003 airfoil undergoing constant ramp motions at Reynolds number $\mathrm{Re} = 6 \times 10^4$. The equivalence is constructed based on the geometric effective angle of attack according to the quasi-steady thin-airfoil theory. Two rates of descent (or pitch up) are analyzed for different Mach numbers in order to investigate the effects of compressibility on the evolution of the DSV. During the onset of the DSV and its transport along the airfoil surface, remarkable similarities are found between pitch and plunge in terms of flow topology, aerodynamic loads and signatures of wall pressure and friction coefficients. However, these flow similarities cease at high-load conditions as the DSV becomes more susceptible to the peculiarities of the airfoil motion, manifested here by different trailing-edge vortices (TEVs). Employing a correction for the rotation-induced apparent camber effect present in the pitching case, which results from the quasi-steady thin-airfoil theory, improves the agreement between pitch and plunge. However, it is not sufficient to assimilate their disparate trailing-edge systems. Results also demonstrate that the limit angle at which pitch-plunge equivalence remains valid decreases for higher Mach numbers.

Finally, we propose a framework whereby numerical simulation data is leveraged to extract relevant information from experimental visualizations. To this end, the convolutional block of pre-trained InceptionV3 network is used to build a regression model that links the map of pressure coefficient to aerodynamic coefficients of the airfoil. The resulting convolutional neural network (CNN) correctly interprets the attributes present in the input flow image. Aspects of the generalization of the model are discussed and the performance of the velocity field as input is assessed. Results show that pressure is preferable to velocity when it comes to building our regression model. Nonetheless, we demonstrate that the velocity can be used to synthesize any corresponding physical quantity through an image-to-image translation approach. Here, the mapping between velocity and pressure coefficient field is used as example.

Keywords: Dynamic stall, computational fluid dynamics, flow modal decomposition, convolutional neural networks.

Contents

1 Introduction

Wings or blades subjected to a large transient increase in effective angle of attack, whether due to some maneuver or an unsteady incoming flow, exhibit a flow condition referred to as dynamic stall. This condition is frequently associated with an increase in unsteady loading that leads to large torsional forces and mechanical vibrations (Corke and Thomas, 2015; Eldredge and Jones, 2019). Dynamic stall influences the performance and fatigue life of several mechanical systems, such as helicopter rotors, wind turbines and flapping wing aerial vehicles, and understanding this phenomenon is of paramount importance to predict performance parameters and improving the design of the mentioned engineering systems (Corke and Thomas, 2015; Buchner *et. al*, 2018; Fouest and Mulleners, 2022).

Extensive studies of airfoils undergoing sinusoidal pitch motions have been carried out by aeroelasticians and dynamic stall researchers, specially aiming for flow conditions of helicopter rotor flight (Carta, 1979). However, a renewed interest in unsteady low Reynolds number aerodynamics has emerged due to applications in small and micro unmanned aerial vehicles (UAVs) and small wind turbines, some of which are inspired by the demonstrated success of natural fliers (Shyy *et. al*, 2007). Novel bio-inspired turbines, for example, use the motion of a flapping foil to drive a generator, by which power is typically extracted from the plunging motion (Young *et. al*, 2014).

Another intriguing aspect of the low Reynolds aerodynamics of plunging motions was recently brought up by Gursul and Cleaver (2019). They found that, in a periodically plunging airfoil, the leading-edge vortex can adversely affect thrust generation, going against what is commonly suggested in the literature of flapping wings (Anderson *et. al*, 1998; Wu *et. al*, 2020). In addition to its impact on flight stability and performance, the dynamic stall vortex (DSV) can also cause fatigue problems due to the increased unsteady loads that lead to large torsional forces and mechanical vibrations on the blade. These drawbacks offer scope for a myriad of flow control studies focusing on the leading edge (Lombardi *et. al*, 2013; Beahan *et. al*, 2014; Müller-Vahl *et. al*, 2016; Ramos *et. al*, 2019). Particularly, Chandrasekhara (2007) discusses that above a threshold level, the vorticity coalesces into a vortex whose behaviour cannot be controlled. Hence, understanding the flow physics near the leading edge is crucial to the effectiveness of control strategies that mitigate the formation of the DSV.

The present work seeks to elucidate the onset mechanisms of dynamic stall occurring on a periodically plunging airfoil, which is more closely related to the emulation of gust effects or flapping wings. In addition, we also assess in what sense pitch and plunge can be taken as equivalent. The importance of this study lies on the scarce research on dynamic stall for plunging airfoils, especially at low and moderate Reynolds numbers. Although one could establish a relationship between the study of pitch-plunge equivalence and the onset mechanisms in periodically plunging airfoils, these topics will be treated as separate problems in what follows. Throughout the work, data-driven techniques are applied in order to better understand the physical phenomena involved. In this sense, machine learning is applied for developing surrogate models and extracting features from high-fidelity simulation data.

1.1 Dynamic stall onset

The main characteristics of dynamic stall are considered to be well established, specially for deep stall conditions. However, the underlying mechanisms of flow separation are still a topic of research. One of the reasons for this is the poor understanding of the viscous effects in unsteady aerodynamics, which are hampered not only by the inherently complex flow dynamics, but also by the influence of multiple interrelated parameters such as compressibility, transition and airfoil geometry. Moreover, the amplitude, frequency and type of airfoil motion also play a key role on the onset of dynamic stall.

Depending on the preceding factors, the dynamic stall inception exhibits different phenomena such as shear layer instabilities (Mulleners and Raffel, 2012), transition to turbulence (Ekaterinaris and Platzer, 1998), laminar separation bubble bursting (Visbal, 2014), shock-induced separation (Bowles *et. al*, 2012; Corke and Thomas, 2015), boundary layer separation (Gupta and Ansell, 2020) and airfoil-vortex interactions (Jones and Cetiner, 2021). For low Mach numbers, when shock waves are absent, the onset mechanism of dynamic stall may involve a bubble burst and its subsequent breakdown owing to strong adverse pressure gradients typically found along the airfoil leading edge (McAlister and Carr, 1979; Doligalski *et. al*, 1994; Lee and Gerontakos, 2004). In a classical description of the phenomenon, a leading edge vortex is formed after a boundary layer flow reversal that moves upward from the trailing edge to the leading edge over the airfoil suction side (McAlister and Carr, 1979; Doligalski *et. al*, 1994; Lee and Gerontakos, 2004).

Several experimental investigations performed in the past years have provided a significant amount of information on the overall flow features and aerodynamic coefficients observed during the dynamic stall process and its incipient moment. Experimental techniques such as flow visualizations (McAlister and Carr, 1979), force measurements (Strickland and Graham, 1987; Jumper *et. al*, 1987), surface pressure and hot-film measurements (Lorber and Carta, 1988; Lee and Gerontakos, 2004; Gardner *et. al*, 2014b), interferometric techniques (Chandrasekhara *et. al*, 1994), and particle image velocimetry (Mulleners and Raffel, 2012; Pruski and Bowersox, 2013) have been applied to investigate dynamic stall. Attempts to reproduce and describe dynamic stall by computational means were also carried out by several groups and a review is provided by Ekaterinaris and Platzer (1998).

Examples of simulations include 2D studies at laminar (Visbal and Shang, 1989; Choudhuri *et. al*, 1994; Choudhuri and Knight, 1996) and transitional/turbulent (Ekaterinaris *et. al*, 1995; Sangwan *et. al*, 2017) Reynolds numbers, some of them also accounting for different compressible regimes. For high Reynolds number flows, numerical studies have traditionally employed turbulence models partially corrected by the incorporation of empirical transitional models to obtain an effective eddy viscosity. Recently, Sangwan *et. al* (2017) performed a 2D simulation without any transition or turbulence model to capture the physics of the dynamic stall process. These authors observed that, for an increasing Mach number, the cycle hysteresis in the fluid dynamic forces and moments is attenuated, reducing the vulnerability to stall flutter but also attaining similar maximum load coefficients, what is a favorable behavior to helicopter designers. In addition, a change in the dynamic stall vortex mechanism along with multiple shock formations was observed at freestream Mach number $M_\infty = 0.5$.

Reynolds-averaged Navier-Stokes (RANS) computations, and their unsteady counterpart (URANS), have been employed for probing massively separated flows. These techniques should be used with a judicious choice of proper turbulence models. Although continually employed (Costes *et. al*, 2015; Kaufmann *et. al*, 2017), these formulations cannot be expected to truly predict the dynamic stall phenomenon given the complex flow physics at play near the leading edge. In particular, viscous mechanisms such as the development of the boundary layer, incipient separation and noise generation (Nagarajan *et. al*, 2006a) that occur in dynamic stall are hardly characterized from a RANS perspective, although advances are being made in this area (see Bernardos *et. al* (2019) for instance). Similar limitations also apply to experimental studies that rely on flow visualizations or low spatio-temporal resolution techniques. The lack of information about the events occurring inside the boundary layer end up limiting the exploration of active flow sensing, control strategies and the development of new turbulence and reduced-order models for dynamic stall.

With recent progress in numerical methods and the increase in computational power, high-fidelity numerical simulations can be used as a predictive tool in the design stage. In this sense, wall-resolved large eddy simulations (wrLES) are increasingly being used to address the onset of dynamic stall at a broad range of Reynolds numbers, providing essential information about the boundary layer dynamics, including its separation. Motivated by micro air vehicle applications, the first investigations of dynamic stall under a transitional flow regime using implicit large eddy simulations (ILES) were presented by Visbal (2009, 2011) for a periodically plunging airfoil. Visbal observed that, at low Reynolds numbers ($\mathrm{Re} = O\left(10^4\right)$), transition effects played a critical role in the leading edge vortex dynamics and, in turn, to the aerodynamic coefficients, even when the incipient separation and DSV formation were initially laminar. The leading edge vortices were found to experience an abrupt breakdown into fine-scale turbulence due to spanwise instabilities. This resulted in a subsequent vorticity cancellation that led to a rapid reduction of the maximum values of phase-averaged vorticity. These investigations were further extended to higher Reynolds numbers ($\mathrm{Re} = 2 \times 10^5$ and 5×10^5) for a constant pitching rate motion by Visbal (2014), where it was found that the onset of dynamic stall was characterized by the presence of a laminar separation bubble (LSB) near the leading edge.

Just recently, the importance of the LSB on the dynamic stall onset could be verified. This difficulty stems from the small spatial scales associated with the LSB and from the high sensitivity of the phenomenon to the state of the boundary layer. Benton and Visbal (2018a) observed through the use of wall-resolved ILES that, when the separated flow at the trailing edge moves upstream and reaches the LSB, bubble bursting is triggered. The bursting, in turn, results in the formation of a small leading edge vortex that rolls up the separated flow to develop the dynamic stall vortex. By using high-frequency flow actuation, they demonstrated the role of the LSB on the onset of dynamic stall, showing that when its presence is overshadowed by the actuator, the classic trailing edge stall takes place with a dynamic stall vortex originating only near the mid-chord.

As an extension of the previously mentioned work, Benton and Visbal (2018b) conducted a parametric study of pitching parameters for NACA0009 and NACA0012 airfoils to understand the role of the LSB and the sensitivity of the pitching motion on the dynamic stall process. They concluded that, although the flow is dominated by the reversed flow, the LSB is a key factor for the development of the leading edge vortex, highlighting the implications of not resolving the transitional features of the flow in a numerical simulation. Also, they attribute the variability in the location and timing of the dynamic stall vortex to the delay between the LSB and its interaction with the upstream propagation rate of the turbulent separation.

A wide range of control approaches has been investigated to mitigate or fully suppress the formation of the stall vortex by both active and passive means. Usually, these efforts were targeted primarily in the reduction of the unsteady fluctuations of lift and pitching moment, while avoiding the loss of mean lift. Inspired by the boundary layer theory of Prandtl (Prandtl, 1904), particular attention was historically given to constant suction (Karim and Acharya, 1994) and blowing (Gardner *et. al*, 2014a) as flow control concepts. In these applications, when the jet momentum from the constant blowing exceeds a critical value, an offset of the adverse pressure gradient that would otherwise promote separation is observed. Zero-net-mass-flux excitation, which relies on the amplification of periodic disturbances through a Kelvin–Helmholtz instability mechanism, has also been shown to effectively suppress the formation of dynamic stall (Greenblatt and Wygnanski, 2001). Recently, high-fidelity simulations performed by

Ramos *et. al* (2019) for a plunging SD7003 wing section under a $\mathrm{Re}_c = 6 \times 10^4$ and $M_\infty = 0.1$ showed an effective frequency range in which the actuation exhibits a more pronounced disruption of the dynamic stall vortex.

The present work seeks to elucidate the onset mechanisms of dynamic stall occurring on a periodically plunging airfoil. The present wrLES methodology (see discussion on § 2.1) is able to resolve the flow features of the unsteady separation; such a level of understanding is a prerequisite to the systematic exploration of flow control strategies for unsteady airfoils. To this end, the same configuration from Visbal (2011) is employed here since it serves as a starting point in terms of validation. However, different analyses are carried out in the present work which include a detailed inspection of the boundary layer characteristics, besides the onset and evolution of the DSV. Moreover, differences in phenomenology due to Mach number variations are examined by considering the time-variations of lift, drag and pitching moment coefficients, including their connection with the instantaneous flowfield and instabilities that initiate the formation of the DSV, as discussed in § 3.1. A detailed analysis of the physical processes related to the dynamic stall onset is provided in § 3.2. Although different compressible regimes are studied, aspects of shock-induced separation are not present in the flows of interest here since they would alter the underlying onset mechanisms. For a comprehensive parametric study of compressibility effects on dynamic stall, the reader is referred to Bowles (2012); Bowles *et. al* (2012); Corke and Thomas (2015); Sangwan *et. al* (2017), and Benton and Visbal (2020).

1.1.1 Empirical criteria for dynamic stall onset

Given our interest in the DSV inception, the present analysis can benefit from the incorporation of indicators of flow separation. Over several decades, researchers recognized the importance of the flow parameters at the leading edge as a factor in the DSV initiation (Evans and Mort, 1959; Ekaterinaris and Platzer, 1998; Ramesh *et. al*, 2018). These parameters serve as indicators of massive flow separation, allowing the construction of dynamic stall models (Ramesh *et. al*, 2014; Eldredge and Jones, 2019) and the definition of control strategies for mitigation of the DSV (Chandrasekhara, 2007; Sedky *et. al*, 2020b). A particular flow parameter that gained popularity recently is that from Ramesh *et. al* (2014), termed the leading edge suction parameter (LESP). By calculating the first term A_0 of the Fourier series for the distribution of a vortex sheet along the camber line using thin airfoil theory, the previous authors observed that the airfoil can support a maximum amount of leading edge suction. When this limit is exceeded, vorticity is released from the leading edge giving rise to the dynamic stall vortex.

For a specific airfoil shape and flow Reynolds number, the LESP threshold has a constant value, regardless of motion kinematics, as long as there is no trailing edge flow separation. Under this assumption of attached flow, the instantaneous value of the LESP can be calculated from unsteady airfoil theory (Ramesh *et. al*, 2014), what makes it of particular interest for reduced order modeling. However, since most occurrences of dynamic stall exhibit some degree of trailing edge separation and flow reversal, researchers are focused on better understanding the behavior of this parameter (Narsipur *et. al*, 2020; Hirato *et. al*, 2021). In addition, different onset criteria and thoughts about the criticality of the flow parameters have emerged in the literature. For instance, He *et. al* (2020) studied the influence of trailing edge flap kinematics on the critical values and timing of the LESP and suggested that the dynamic stall development is governed by characteristic stall delays rather than a critical LESP threshold. Deparday and Mulleners (2019) observed that the critical values of the chord-normal shear layer height and the airfoil circulation were invariant with respect to the airfoil motion and, thereby, served as better indicators of the dynamic stall onset. However, the effects of compressibility on the applicability and reliability of these criteria were not assessed. Moreover, the shear layer height criterion was never applied for airfoils under ramp conditions, where the effective angle of attack increases with a constant rate. In § 4.6, an assessment of the LESP and chord-normal shear layer height criteria is presented to characterize onset of the DSV for a periodic plunging airfoil. Both indicators of DSV onset are evaluated from the context of compressibility to verify their validity range.

1.1.2 Flow modal analysis

Modal decomposition techniques are also applied in the context of dynamic stall to offer a global perspective of the frequency dynamics in a spatially organized manner. These can eventually provide suitable actuation parameters for flow control. The benefits of the dynamic mode decomposition (DMD) (Schmid, 2010; Tu *et. al*, 2014) was shown by Dunne *et. al* (2016) for the identification of the time scales associated with dynamic stall. Mohan *et. al* (2016) combined the proper orthogonal decomposition (POD) with DMD to identify transient energetic flow structures relevant to dynamic stall. However, in their analysis, no attention was given to the inception of the unsteady separation, and this work seeks to fill this gap. Hence, DMD and its multi-resolution variant (mrDMD) (Kutz *et. al*, 2016) are used in § 4.7 to identify and characterize the spatial structures that appear at specific frequencies during the onset of dynamic stall, including compressibility effects. We show that there is considerable advantage in applying the mrDMD due to the highly transient nature of the problem, where different events have time scales that vary widely. This technique is able to represent the transient or intermittent dynamics that the standard DMD fails to capture.

Other modal decomposition techniques have also been employed to investigate the dynamic stall process. For instance, the empirical mode decomposition (EMD) was used by Ansell and Mulleners (2020) to extract physically meaningful intrinsic mode functions and by Gupta and Ansell (2020) to identify the spectra of the velocity fluctuations near the leading edge. Coleman *et. al* (2019) applied the parametric modal decomposition (PMD), which provides globally optimized modes across the entire parameter space of a series of experiments, and Melius *et. al* (2016) applied POD to identify and quantify relevant flow features related to the DSV. However, it is important to mention that one of the main focus of the present study is on dynamic stall onset, which is a phenomenon occurring at a short temporal scale. Hence, the mrDMD is the method of choice since it is capable of extracting meaningful flow features at particular temporal windows. To the authors' knowledge, this is the first time that the mrDMD is applied in the context of dynamic stall.

1.2 Pitch-plunge equivalence

Aimed to better understand the increased torsional motions encountered on flexible blades, the helicopter industry concentrated efforts to generate a substantial body of data for airfoils oscillating in pitch about the quarter-chord (Carta, 1979). As a consequence, research on dynamic stall for plunging airfoils is more scarce, especially at low and moderate Reynolds numbers.

Historically, the lack of experimental results for plunging airfoils entailed the usage of pitching data to predict plunging responses. The validity of the assumptions made to sustain such motion interchange was questioned by Carta (1979) after noticing occasional discrepancies between them, particularly at high-load conditions. It was postulated that the pitch-plunge mismatch upon departure from small-amplitude linearizations was caused by the distinct dynamic stall breakdown processes. Later on, Ericsson (1995) attributed the variations in the aerodynamic response to the differences in the so-called moving-wall effects. The relative importance of different flow physics contributions to the pitch-plunge equivalence was brought out by McGowan *et. al* (2011) in going from quasi-steady thin-airfoil theory to Theodorsen's model. In this manner, the effects of noncirculatory contributions and wake vorticity could be included, and a limit for when linear predictions remain valid in massively unsteady flows was proposed. In a similar fashion, a new equivalence criterion based on the unsteady lifting line theory (Bird and Ramesh, 2021) was explored by Bird and Ramesh (2018), whereby accurate results were produced for high amplitude oscillations. Expanding on past studies that have examined only linear superposition of pitch and plunge motions, Elfering and Granlund (2020) analysed airfoils undergoing surge–pitch–plunge combinations using the Greenberg lift equation (Greenberg, 1947) to account for the phase shift between the sinusoidal combinations of these motions. Baik *et. al* (2012), in turn, studied the role of Reynolds number, reduced frequency and Strouhal number on the aerodynamics of pitching and plunging flat-plate airfoils. Efforts to determine pitch-plunge equivalence for three-dimensional problems are also arising. Recently, Bird and Ramesh (2018) extended the 2D lift-based approaches from McGowan *et. al* (2011) to finite wings employing unsteady lifting line theory, Theodorsen-based strip theory, and simulations of the Navier-Stokes equations.

Most studies in the context of pitch-plunge equivalence are devoted to predicting plunging response based on tables of existing pitching data, which predominantly use periodically oscillating airfoils. Under periodic motion, vortices that are being advected downstream with the flow interact with the trailing edge, leading to a change in the airfoil circulation and affecting the subsequent stages of the flow dynamics Corke and Thomas (2015); Darakananda and Eldredge (2019). In order to suppress the additional complexities of periodic motion history effects, constant rate pitching motion has been widely used to investigate the dynamic stall inception (Lorber and Carta, 1988; Benton and Visbal, 2018b,a; Visbal and Garmann, 2018). Studies of large amplitude constant pitch rate setups find application in fixed wing aircraft under drastic gust load scenarios (Ol *et. al*, 2009; Fouest *et. al*, 2021). In this sense, Schreck *et. al* (2002) and Eldredge *et. al* (2009) investigated the influence of pitch rate and Reynolds number on the formation of the leading-edge vortex (LEV). These studies were later extended to include the effects of pitch pivot point location by Granlund *et. al* (2013); Yu and Bernal (2017), and Yu *et. al* (2018). The role of a laminar separation bubble on stall onset was analyzed for pitch ramp airfoils by Benton and Visbal (2018a, 2019b,a) and Gupta and Ansell (2019), and the effects of compressibility on the bubble bursting and the subsequent development of the dynamic stall vortex (DSV) were studied by Chandrasekhara *et. al* (1994) and Benton and Visbal (2020). The existence of flow three-dimensionality in both the LEV and trailing-edge vortex (TEV) was also examined considering pitch ramp maneuvers (Buchner *et. al*, 2012; Yu and Bernal, 2017).

To investigate the pitch-plunge equivalence problem of ramp configurations, Ol *et. al* (2009) conducted a water tunnel experiment and performed 2D vortex-particle simulations and observed that the equivalence fails due to different TEVs. In fact, the peculiarities of the trailing-edge dynamics have also been reported in other cases besides the ramp motion (Ol *et. al*, 2008; Rival and Tropea, 2010; Prangemeier *et. al*, 2010; Baik *et. al*, 2012; Lee *et. al*, 2022). Naturally, the mismatch between pitch and plunge under certain conditions resulted in questioning the validity of the effective angle of attack definition (McGowan *et. al*, 2008; Ol *et. al*, 2008). Recently, Visbal and Garmann (2022) attributed the differences between pitch and plunge to the rotation-induced apparent camber effect. After subtracting this contribution from the pitching airfoil, the previous authors were able to reconcile lift and moment coefficients for periodic maneuvers. However, there is still an open question whether this correction is sufficient to establish a pitch/plunge motion equivalence for ramp maneuvers and high effective angles of attack. Addressing this question is important as it dictates the extent to which dynamic stall is mostly influenced by geometric effects. Such level of understanding of the phenomena can, in principle, help to improve existing models. For instance, Darakananda and Eldredge (2019) presented an efficient two-dimensional vortex model for real-time flow estimation and found good agreement with simulations of highly unsteady airfoils. They highlighted the importance of accounting for viscous mechanisms and the interplay between LEV and TEV on the flow dynamics, which could be incorporated to their model using data-driven techniques.

Due to its easy interpretability, several authors (Ol *et. al*, 2009; Baik *et. al*, 2012; Sedky *et. al*, 2020a; Visbal and Garmann, 2022) have used the geometrical effective angle of attack to study different airfoil kinematics, even in cases where the assumptions involved in the derivation from quasi-steady thin-airfoil theory (inviscid, incompressible, attached flows, small angles, thin airfoil, and small camber) are violated. A number of recently developed theories of unsteady aerodynamics (Ramesh, 2020; Bird and Ramesh, 2021; Taha and Rezaei, 2019, 2022) make the usage of a pure-geometrical criterion far from adequate; they are, nevertheless, encouraging and indicative of possible fruitful exploration of better criteria to be used from here on. In this context, a comparison of the equivalence using the expressions from Bird and Ramesh (2018), Ramesh (2020), Xu and Lagor (2021) and Taha and Rezaei (2019, 2022) is highly desirable. However, the objective of the present work is not to look for the best equivalence criterion. Instead, here we assess the validity of a simple criterion based on the geometric effective angle of attack due to its easy interpretability and its high adoption in the literature. This is motivated by the abstraction of the airfoil kinematics into a ramp-type motion, which builds upon the work of Ol *et. al* (2009). Here, high-fidelity simulations are employed to extend the analyses to a higher Reynolds number, where the flow is turbulent. An assessment of compressibility effects is also presented, differently from other studies.

One of the purposes of this study is to address the pitch-plunge equivalence problem through an assessment of airfoil kinematics and Mach number variations that lie beyond the assumptions of previous work that considered incompressible potential flows (McGowan *et. al*, 2011; Bird and Ramesh, 2018; Baik *et. al*, 2012; Ol *et. al*, 2009). A natural step to facilitate the understanding of pitch-plunge equivalence in this case is to simplify the airfoil kinematics into a constant-ramp motion, where the induced angle of attack of the plunging configuration matches the geometric angle of attack of the equivalent pitching case. Two rates of descent (or pitch up) are analyzed together with the effects of compressibility for an SD7003 airfoil at $Re = 6 \times 10^4$. For a given Mach number, different maneuvers are simulated starting from the exact same steady solution, thereby minimizing possible variations due to different initial conditions. The pitch-plunge equivalence is then investigated through a comparison of aerodynamic coefficients, instantaneous pressure distributions, visualization of flow topologies and friction coefficient maps. The frequency and spatial information provided by flow modal decomposition techniques could eventually be used to provide suitable actuation parameters for flow control. In this work, dynamic mode decomposition (DMD) (Schmid, 2010; Tu *et. al*, 2014) and its multi-resolution variant (mrDMD) (Kutz *et. al*, 2016) are chosen to identify and characterize the spatial structures that appear at specific frequencies during the onset of dynamic stall.

1.3 Surrogate models using deep learning

Unsteady aerodynamic loads generated during dynamic stall play a critical role in determining both the mechanical life span and performance of unsteady lifting devices such as helicopter rotors and wind turbine blades. To control these loads, it is required both an understanding of the unsteady flow conditions as well as providing mechanisms for prescribing the ensuing flow-wing interactions. However, the temporal and spatial complexity of unsteady separated flows renders them difficult to fully characterize and understand. It comes as no surprise that, thus far, unsteady separated flows have defied obtaining general analytical solutions.

Although potentially accurate, numerical simulations of unsteady separated flows require large amounts of computational time. Experiments are also complex and time consuming. As such, the broad parameter space encompassed by unsteady separated flows hamper exhaustive characterization by computational or experimental means. This precludes prediction and control across the broad range of conditions likely to be encountered in the flight regime. Fortunately, the emerging of machine (deep) learning techniques could provide more ideas for leveraging models. The era of big data and the significantly improved computing power have laid a good foundation for applying machine learning techniques to complex problems. Therefore, the provided massive labeled flowfield data makes it promising to expand these techniques to unsteady fluid mechanics applications.

Since the 1990s, researchers have shown that neural networks can predict flowfield evolution under static (Linse and Stengel, 1993; Ha, 1995) and dynamic conditions (Faller *et. al*, 1994; Schreck *et. al*, 1995), and also construct accurate models and efficient real-time control strategies for highly time-dependent, unsteady separated flows such as those encountered in dynamic stall problems (Kawthar-Ali and Acharya, 1996). Overall, these early attempts demonstrate the capacity of neural networks to model aerodynamic coefficients from simulated flight-test data with a few number of hidden layers and nodes when compared to the current state-of-the-art network architectures. Despite their success, deep neural networks were mostly abandoned in the early 2000s due to the unstable gradients observed as the algorithm progresses down to the lower layers. It was only after Glorot and Bengio (2010) that some light was shed on the causes of the unstable gradients, making deep learning popular again.

In recent years, machine learning has emerged as a promising technique for various applications in fluid mechanics, like turbulence modeling (Ling *et. al*, 2016; Wu *et. al*, 2018; Maulik *et. al*, 2019; Duraisamy *et. al*, 2019; Ahmed *et. al*, 2021), reduced order modeling (Rowley and Dawson, 2017; Lui and Wolf, 2019; Wang *et. al*, 2019; Eivazi *et. al*, 2020; Fukami *et. al*, 2021), flow control (Raibaudo *et. al*, 2020; Zhou *et. al*, 2020; Cornejo Maceda *et. al*, 2021), among others. To mention a few examples, Lui and Wolf (2019) presented a numerical methodology for construction of reduced order models of fluid flows through the combination of flow modal decomposition and nonlinear regression analysis. Their approach allowed the prediction of the flow field beyond the training window and with larger time increments than those used by the full order model. Kochkov *et. al* (2021), in turn, used deep learning inside traditional fluid simulations to improve both accuracy and speed even on examples very different from the training data. Their method uses machine learning to interpolate better at a coarse scale, achieving the same accuracy as traditional finite difference/finite volume methods, but with a much coarser resolution. As a result, they were capable of expanding the Pareto frontier of efficient simulation in CFD. Complementary information on the use of machine learning for fluid dynamics can be found in many recent reviews (see Brunton *et. al* (2020); Willard *et. al* (2022); Rabault *et. al* (2020); Pandey *et. al* (2020); Fukami *et. al* (2020); Kou and Zhang (2021) and Brunton (2021) for instance).

It is still unclear how far the applications of machine learning in fluid mechanics can reach. Above all, more studies need to be carried out to determine the applicability and reliability of machine learning in fluid mechanics, not only on turbulence modeling (Kutz, 2017), but also on feature characterization, reduced order modeling, and flow control. For instance, in a myriad of engineering situations, we often hope to establish a model capable of predicting load conditions around structures through flow features detection or *vice versa*. For this reason, in the present work, we focus on the relationship between the flow structure and the concerned flow statistics.

Success on ImageNet Classification[1] with convolutional neural networks (CNNs) makes them an interesting technique due to its fewer connections and parameters (Krizhevsky *et. al*, 2012). CNNs have been successfully applied to identify features in fluid flows by Strofer *et. al* (2019). Jin *et. al* (2018) designed a CNN architecture to predict the velocity field around a cylinder using measurements of the surface pressure as input. Ye *et. al* (2020) used the classical simple network LeNet-5 to predict the pressure on a cylinder from the velocity distributions along its wake. CNNs were also shown

---

[1] ImageNet is a large database of images classified into many classes, commonly used to evaluate computer vision systems

to be viable alternatives for detecting shock waves, with less time consumption than traditional methods (Liu *et. al*, 2019). This class of network was also employed in a new technique to extract underlying flow features from the original flow field data, as proposed by Obayashi *et. al* (2021). These authors made use of the nonlinear decomposition from the CNN process to extract flow features different from those of proper orthogonal decomposition in each mode. Guastoni *et. al* (2021) and Güemes *et. al* (2021) used CNNs to predict two-dimensional instantaneous velocity-fluctuation fields at different wall-normal locations from wall measurements.

The studies mentioned above demonstrate the possibilities that CNNs exhibit in the detection of features in fluid mechanics. For this reason, here, we chose this class of artificial neural network to study the flowfields from our numerical simulations. Different CNN architectures are employed in the hope of finding the mapping relation between the flow structures and the underlying airfoil responses. Dynamic stall is taken here as an example since the flow has a common structure owning certain complexity as well. Despite that, the concepts applied herein can be easily extended to other branches of fluid mechanics where a regression task is involved. That said, based on any fluid property from the unsteady flowfield, the network between the existing flow structures and some concerned flow feature is constructed. This CNN-based deep learning method, then, links the map of fluid property to the aerodynamic coefficients, which represents the feature learned from the flow field.

Quantifying the flow dynamics in engineering systems is the centerpiece of this work and the aforementioned CNN method is only one step towards this goal. Here, we aim at reusing or transferring information from previously learned tasks to extract quantitative information from available flow visualizations. Despite substantial advances in experimental fluid mechanics, the use of measurements to reliably infer fluid properties, like density, velocity, pressure or stress fields, is not a straightforward task. This information, though, comes natural to CFD practitioners. So, in our study, we address the question of using the information learned from numerical simulation datasets to extract fluid properties from experiments that until then would be very complicated or even impossible to obtain.

Pressure is a good example of thermodynamic quantity that plays a key role in fluid mechanics. It is of utmost importance in aerodynamic load prediction, noise generation, flow instability and turbulence, among others. The increase of time resolution in velocity field measurements during the last decade has opened the path to obtaining instantaneous pressure fields by combining the experimental data with the governing equations (van Oudheusden, 2013; van Gent *et. al*, 2017). But often, the available high-speed cameras and lasers for Particle Image Velocimetry (PIV) do not offer a high enough sampling frequency for flows of practical interest, which hinders this approach. In case of poor time resolution, the pressure field can be obtained by solving a Poisson equation if the flow is incompressible. But still, the missing time information poses specific constraints in the boundary conditions (Van der Kindere *et. al*, 2019; Chen *et. al*, 2022).

Recent developments on machine learning have recently been paving the way to new interesting research avenues without the need of time-resolved field measurements to estimate pressure. Using velocity-probe measurements with high sampling frequency, Jin *et. al* (2020) combined POD with recurrent neural networks to reconstruct the spatial distribution of velocity, retrieving the time resolution from PIV. Raissi *et. al* (2020) used a physics-informed neural network (PINN) to construct computationally efficient and fully differentiable surrogates for velocity and pressure fields from the transport of passive scalars. Their technique allows the extraction of quantitative information from available flow visualizations such as the transport of dye or smoke in physical systems and contrast agents in biological systems. PINNs were also used to quantify velocity and pressure fields from tomographic background oriented Schlieren (Cai *et. al*, 2021) and PIV images (Wang *et. al*, 2022).

The quest to amplify the scope of information extracted in experimental fluid mechanics is one of the major pursuits of the current work. But differently from the cited references, here, we propose a framework whereby numerical simulation data is leveraged to extract relevant information from experimental visualizations. From the theoretical standpoint, the flowfield represented in the input image is already a result of the Navier-Stokes equations. Even though the prior knowledge of the Navier-Stokes equations introduces an effective regularization mechanism in the training of neural networks (Raissi *et. al*, 2019), no physical information had to be inferred to the CNN to accomplish the purpose of our work. Results show that the neural network can successfully predict the pressure field or any other fluid property from velocity inputs. Wang *et. al* (2019) show that forecasting future dynamics can benefit from physical guidance, but predicting future frames is not the scope of our work. Here, we seek to extract more information from already existing experimental imaging data.

1.4 Objectives and thesis outline

The primary objective of this work is to study the onset and evolution of the DSV for a transitional Reynolds number flow ($\text{Re} = 6 \times 10^4$), also examining the differences in phenomenology due to compressibility variations. Although compressibility effects are present in many cases of dynamic stall, they have been little studied. Such level of understanding of the onset mechanisms and state of the boundary layer is paramount for designing effective control strategies to mitigate dynamic stall. For this task, initially, an SD7003 airfoil under periodically plunging motion is considered at freestream Mach numbers $M_\infty = 0.1$ and 0.4. Then, the airfoil kinematics is modified to address the pitch-plunge equivalence problem. Such study can be considered as a second objective from this thesis, and it is motivated by the need for outlining the limits at which dynamic stall is mostly influenced by geometric effects. Finally, another objective of this work consists in developing novel strategies of reduced order modeling and feature extraction from the high fidelity dynamic stall datasets. For this, machine learning appears as a natural candidate.

The first/present chapter of this thesis presented a literature review of several studies on dynamic stall, including both numerical simulations and experiments. An overview of different modal decomposition techniques applicable in the context of dynamic stall as well as onset criteria of DSV were presented. These topics play a key role in the characterization of dynamic stall. In this chapter, we also introduced the pitch-plunge equivalence problem and how it fits into the context of using already existing data for an intended aerodynamic purpose. Then, the last part of the literature review discussed emerging machine learning researches applied to fluid mechanics as well as past studies carried out on dynamic stall in the late 1990s.

The second chapter describes the theoretical formulation and the numerical methods employed herein to compute the flow fields. The computations are performed with an in-house Navier-Stokes solver written in generalized curvilinear coordinates in fully contravariant form. Theoretical implications of this contravariant notation are presented and a new formulation is proposed (see Appendix A). Post-processing techniques are discussed for the unsteady flows at hand. These include the standard DMD algorithm and its multi-resolution variant, and some empirical criteria for assessing dynamic stall onset.

The third chapter is dedicated to the analysis of the onset of dynamic stall. We simulate an SD7003 airfoil undergoing periodic plunging motion following earlier studies as they serve as benchmark for validation. However, in contrast to these works, we focus on the incipient moment of the flow separation while accounting for compressibility effects. In this sense, earlier spanwise fluctuations and higher flow three-dimensionality are observed in the higher compressible regime. Despite that, an apparent Mach number invariance seems to exist during the birth of the Kelvin-Helmholtz instability that precedes the dynamic stall onset. The separation, in turn, follows the van-Dommelen-Shen process and the robustness of some empirical separation criteria to compressibility variations is assessed. Finally, in this chapter, modal decomposition analyses are carried out aiming to extract the embedded dynamics associated with the separation process and their respective frequency content. This level of understanding of the onset phenomenon is crucial for the design of effective flow control strategies to mitigate the DSV formation. In this scenario, finding a proper algorithm capable of extracting physically meaningful flow structures marks an important milestone in the overall context of this thesis.

The fourth chapter of this thesis refers to the pitch-plunge equivalence problem. Here, the airfoil and flow conditions are kept the same as in the previous chapter (Reynolds and Mach numbers, and the static angle of attack) and only the motion prescribed by the airfoil is changed. The equivalence is constructed based on the geometric effective angle of attack according to the quasi-steady thin-airfoil theory. Flow topology, aerodynamic loads and signatures of wall pressure and friction coefficients are then compared on a time-wise basis for pitching and plunging airfoils under constant ramp motions. It is important to mention, however, that the flow topology and onset mechanisms of the cases simulated in this chapter are completely different from those in the previous one. Changing the airfoil kinematics from periodical to ramp-type motion drastically change the flow topology and, hence, the overall results. In this chapter, we demonstrate that the LEV is strongly driven by the rate of change of the effective angle of attack, but we also reinforce the need for a more rigorous definition of the effective angle of attack that takes into account the trailing-edge dynamics and compressibility effects.

Finally, the fifth chapter presents a CNN-based surrogate model developed to predict the aerodynamic coefficients from images of the flow field. The network is capable of identifying relevant flow features present in the image and associate them to the airfoil response. Preliminary results demonstrate that the model is effective in interpolating between flow parameters. Now, research is being done to verify the extrapolation capacity of the model. In addition to this regression task, we propose a model that generates synthetic images of any fluid property of interest given an input image. Preliminary results demonstrated in this chapter show that this is indeed a promising topic for future exploration.

The overall conclusions and findings of this work as well as suggestions for future work are provided in the last chapter of the thesis.

1.5 Contributions of the present work

The main findings of the work are summarized below:

- *Detailed description of the separation process for a dynamic stall configuration:* For the periodic plunging motion, it is shown that the separation process contains two stages: the first being composed by Kelvin-Helmholtz instabilities and the second being a secondary instability that obeys the van Dommelen and Shen model. Results suggest a possible Mach number invariance for the birth of the Kelvin-Helmholtz instability, which appears to be connected to the acoustics at the trailing-edge. Increasing compressiblity, however, induces earlier spanwise fluctuations, higher flow three-dimensionality, and a weaker and more diffuse DSV, with lower residency time.

- *Exploration of the mrDMD algorithm in dynamic stall applications:* To the authors' knowledge, this is the first time that the multi-resolution DMD (mrDMD) is applied to a problem of dynamic stall. As shown in the results, the mrDMD technique overcomes the standard DMD, especially when transient or intermittent events such as dynamic stall onset are to be investigated.

- *Assessment of the robustness of empirical criteria to compressibility variations:* To the authors' knowledge, this is the first time that the robustness of the leading-edge suction parameter (LESP) and of the chord-normal shear layer height technique is assessed under different compressible regimes. Results demonstrate a higher robustness of the latter with respect to Mach number variations. Moreover, in the present analysis, we take advantage of the numerical simulation data to propose a new numerical procedure to calculate the chord-normal shear layer height.
- *Pitch-plunge equivalence for ramp motion airfoils:* We draw on the geometric effective angle of attack to investigate the pitch-plunge equivalence problem for constant ramp motions. With this simple kinematics, we show that the LEV formation and its subsequent evolution is strongly driven by geometric effects. However, this simplistic criterion is not sufficient to maintain the equivalence beyond the point when the TEV system begins. We also report an earlier equivalence breakdown with increasing compressibility due to lower DSV residency time.
- *Investigation of the rotational pseudo-forces:* With the airfoil pitching up at a constant angular velocity, the angular acceleration term vanishes. This condition simplifies the problem and opens for the possibility of exploring how each pseudo-force contributes to the flow dynamics. A detailed explanation around the subject is given, and we conclude that the contribution of the non-inertial forces to the momentum equation is negligible suggesting that the evolution of the DSV is dominated by the apparent camber effect.
- *Development of CNN regression models:* We build a CNN model that predicts the airfoil response based on relevant features extracted from the input image. Provided that the covariance shift is small between the images generated from numerical simulations and those obtained experimentally, this model could potentially be used as a substitute for sensors in experimental campaigns.
- *Image-to-image translation as generators of synthetic fluid properties:* In order to amplify the scope of information extracted in experimental fluid mechanics, we propose a framework whereby numerical simulation data is leveraged to extract relevant information from experimental visualizations. In particular, we uniquely treat the image semantic segmentation as an image-to-image translation task that infers semantic labels of structures from the input images in a supervised way. Given

an input image of velocity, the resulting model generates synthetic images of any corresponding fluid property of interest.

1.6 List of publications

The publications of the present dynamic stall studies include:

- Preliminary results of the pitch-plunge equivalence problem were presented in the AIAA Aviation 2021 Forum (Miotto *et. al*, 2021a).
- Final results of the pitch-plunge equivalence problem were submitted for publication in the AIAA Journal (currently under review).
- Preliminary results of the periodically moving airfoils were presented in the AIAA Scitech 2021 Forum (Miotto *et. al*, 2021b).
- Preliminary results of the periodically moving airfoils were presented in the 18th Brazilian Congress of Thermal Sciences and Engineering (ENCIT) 2020 (Miotto and Wolf, 2020).
- Final results of the periodically moving airfoils were published in the Journal of Fluid Mechanics (Miotto *et. al*, 2022).

Additional studies published during the PhD include:

- Studies on installed jet noise were published in the Journal of the Acoustical Society of America (Nogueira *et. al*, 2019).
- Studies on leading-edge noise prediction based on Amiet's theory were published in the AIAA Journal (Miotto *et. al*, 2018b).
- Preliminary results of the leading-edge noise prediction studies were published in the 2018 AIAA/CEAS Aeroacoustics Conference (Miotto *et. al*, 2018a).

Preliminary results of the periodically moving airfoils were also presented in:

- The Direct In-person Colloquium on Vortex Dominated Flows (DisCoVor) (2022, Villars-sur-Ollon, Switzerland).
- The Remote Colloquium on Vortex Dominated Flows (ReCoVor) (2021, Online).
- The Army Research Office (ARO) Dynamic Stall Workshop (2019, Georgia Institute of Technology).
- 72nd Annual Meeting of the APS Division of Fluid Dynamics (2019, Seattle)

1.7 Useful links and supplemental movies

Supplemental movies can be found in:

- Movies related to Chapter 3:
  `https://doi.org/10.1017/jfm.2022.165` (see "Supplementary materials" section)
- Movies related to Chapter 4:
  `https://drive.google.com/drive/folders/10xs7t7MEJrdjJjD2A31Fu-UPpzCZxzCs?usp=sharing`

PyDMD project that implements the Dynamic Mode Decomposition algorithm and its variants can be found in `https://mathlab.github.io/PyDMD/`.

2 Methodology

In this chapter we describe the numerical methods used in our in-house LES solver and the post-processing techniques employed to study the current flows. This includes the definitions of the leading-edge suction parameter and chord-normal shear layer height; the modal analysis algorithms, and the neural networks used herein.

Appendix A contains a dedicated space for discussing the formulation implemented in our LES solver since the present approach is not commonly seen in standard CFD codes. Here, the Navier-Stokes equations are cast in a fully tensorial form. For that reason, the tensor formalism is presented in the Appendix A along with an alternative formulation that better relates our approach with standard CFD codes.

2.1 Numerical solution of the aerodynamic field

Simulations of dynamic stall are conducted solving the compressible Navier-Stokes equations. The SD7003 airfoil is selected for the present study because of its better suitability to low Reynolds number applications. An O-type grid is employed along the airfoil and, hence, the equations are solved in a general curvilinear coordinate system. In order to resolve the most energetic flow scales, large eddy simulations are performed without the explicit use of a subgrid scale (SGS) model. Hence, to control high-frequency numerical instabilities that would be damped by an SGS model, a sixth-order compact high-wavenumber filter (Lele, 1992) is applied with a proper treatment of wall boundaries (Visbal and Gaitonde, 2002). The transfer function associated with such filters has been shown to provide an approximation to SGS models (Mathew *et. al*, 2003). The implicit LES methodology is chosen based on extensive results presented by Visbal and co-authors (Visbal, 2011, 2014; Benton and Visbal, 2018b,a; Visbal and Garmann, 2018; Benton and Visbal, 2020).

The flow equations are solved using a staggered grid approach as presented by Nagarajan *et. al* (2003). Therefore, the numerical methodology employed in the spatial discretization combines the application of sixth-order accurate compact schemes for calculation of derivatives and interpolations on the collocated and staggered grids. The time integration is performed using an explicit third-order compact storage Runge-Kutta scheme (Wray, 1986) in regions away from solid boundaries. Near the airfoil surface, an implicit second-order Beam-Warming scheme (Beam and Warming, 1978) is applied to overcome the stiffness problem typical of boundary layer grids. Sponge layers and characteristic boundary conditions based on Riemann invariants are applied along the farfield boundaries and adiabatic no-slip boundary conditions are used at solid boundaries. The present flows are three-dimensional, but a periodic boundary condition is enforced along the spanwise direction. Despite being three-dimensional, most of the results are presented in terms of spanwise-averaged quantities to improve the flow statistics.

2.1.1 Governing equations

The compressible Navier-Stokes equations are solved in nondimensional form and in a non-inertial frame of reference. The characteristic length, velocity components, density, pressure, and temperature values used in the nondimensionalization procedure are given, respectively, by the airfoil chord c, freestream speed of sound a_∞, freestream density ρ_∞, $\rho_\infty a_\infty^2$, and $(\gamma-1)T_\infty$. Here, T_∞ is the freestream temperature and γ is the ratio of specific heats. In a non-inertial Cartesian system attached to the airfoil, the equations are written as

$$\frac{\partial \rho}{\partial t} + \mathrm{div}\,(\rho \boldsymbol{u}') = 0 \ , \tag{2.1}$$

$$\frac{\partial(\rho \boldsymbol{u}')}{\partial t} + \mathrm{div}\,(\rho \boldsymbol{u}'\boldsymbol{u}' + p\mathbf{I} - \boldsymbol{\tau}') = -2\rho\boldsymbol{\Omega}\wedge\boldsymbol{u}' - \rho\boldsymbol{\Omega}\wedge(\boldsymbol{\Omega}\wedge\boldsymbol{x}') - \rho\dot{\boldsymbol{\Omega}}\wedge\boldsymbol{x}' - \rho\ddot{\boldsymbol{X}} \ , \tag{2.2}$$

and

$$\frac{\partial E}{\partial t} + \mathrm{div}\,\left[(E+p)\boldsymbol{u}' - \boldsymbol{\tau}'\cdot\boldsymbol{u}' + \boldsymbol{q}\right] = 0 \ , \tag{2.3}$$

where, $\boldsymbol{X} = (0, h(t), 0)$ and $\boldsymbol{\Omega} = (0, 0, \Omega^+)$ are the position and angular velocity of the non-inertial frame, respectively, and primed quantities represent variables measured with respect to the moving frame. The four terms appearing in the right hand side of Eq. 2.2 are pseudo forces defined for frames accelerated in commonly occurring ways: the first two, the Coriolis and Centrifugal forces, involve rotation; the third term is called Euler force, which is caused by a variable rate of rotation, and the last force is caused by the rectilinear acceleration of the moving frame. The total energy and the heat flux for a fluid obeying Fourier's law read as

$$E = \frac{p}{\gamma-1} + \frac{1}{2}\rho\left[\boldsymbol{u}'\cdot\boldsymbol{u}' + \left(\dot{\boldsymbol{X}} + \boldsymbol{\Omega}\wedge\boldsymbol{x}'\right)\cdot\left(\dot{\boldsymbol{X}} + \boldsymbol{\Omega}\wedge\boldsymbol{x}'\right)\right]$$

and

$$\boldsymbol{q} = -\frac{\mu}{\mathrm{Re}_a \mathrm{Pr}}\,\mathrm{grad}\,T \ ,$$

respectively. Finally, the viscous stress tensor is given by

$$\boldsymbol{\tau}' = \frac{1}{\mathrm{Re}_a}\left[2\mu\boldsymbol{S}' - \frac{2}{3}\mu\,\mathrm{div}\,\boldsymbol{u}'\,\mathbf{I}\right] \ ,$$

where

$$\boldsymbol{S}' = \frac{1}{2}\left(\operatorname{grad}\boldsymbol{u}' + (\operatorname{grad}\boldsymbol{u}')^{\mathrm{T}}\right)\ ,$$

is the strain rate tensor and $\mathrm{Re}_a = \mathrm{Re}/M_\infty$ is the Reynolds number based on the speed of sound. Assuming the medium to be a calorically perfect gas, the set of equations is closed by the equation of state

$$p = \frac{\gamma - 1}{\gamma}\rho T.$$

For the sake of a clear readability, the previous governing equations were presented in terms of a Cartesian system. In Appendix A, we show the same equations cast in the tensorial form, as they are numerically solved herein. A parallel with the mixed notation usually employed in computational fluid dynamics is also provided.

2.1.2 Spatial Discretization

The numerical scheme which will be employed for the spatial discretization is a sixth-order accurate compact scheme (Nagarajan *et. al*, 2003) implemented on a staggered grid. In a general curvilinear coordinate system, the staggered first derivative, $f^{'}$, of a function f at interior nodes is computed as

$$\alpha f^{'}_{j-1} + f^{'}_{j} + \alpha f^{'}_{j+1} = b\frac{f_{j+3/2} - f_{j-3/2}}{3\Delta x} + a\frac{f_{j+1/2} - f_{j-1/2}}{\Delta x}, \tag{2.4}$$

where $\alpha = 9/62$, $a = 3/8(3-2\alpha)$ and $b = 1/8(-1+22\alpha)$. The use of a staggered variable arrangement requires a mid-point interpolation formula. The implemented sixth-order accurate formula is given by

$$\alpha f^{I}_{j-1} + f^{I}_{j} + \alpha f^{I}_{j+1} = b\frac{f_{j+3/2} - f_{j-3/2}}{2} + a\frac{f_{j+1/2} - f_{j-1/2}}{2}, \tag{2.5}$$

where $\alpha = 3/10$, $a = 1/8(9 + 10\alpha)$ and $b = 1/8(-1 + 6\alpha)$. The boundary and near-boundary nodes require one side derivative and interpolation formulas that can be found in Nagarajan (2004).

Compact finite-difference schemes are non-dissipative and numerical instabilities arising from insufficient grid resolution, mesh non-uniformities, approximate boundary conditions and interpolation at grid interfaces have to be filtered to preserve stability of the numerical schemes. The high wavenumber compact filter presented by Lele (1992) is applied to the computed solution at prescribed time intervals in order to control numerical instabilities. A one parameter family of sixth-order filters is constructed using

$$\alpha\tilde{f}_{j-1} + \tilde{f}_{j} + \alpha\tilde{f}_{j+1} = af_j + b\frac{f_{j+1} + f_{j-1}}{2} + c\frac{f_{j+2} + f_{j-2}}{2} + d\frac{f_{j+3} + f_{j-3}}{2}, \tag{2.6}$$

where $\tilde{f}_j$ is the filtered solution, $a = 1/16(11+10\alpha)$, $b = 1/32(15+34\alpha)$, $c = 1/16(-3+6\alpha)$ and $d = 1/32(1-2\alpha)$. The spectral response of the filter is adjusted by the filter coefficient α that ranges from $-0.5 \leq \alpha \leq 0.5$. Higher values of α provide less dissipation. The boundary nodes use different filtering formulas that can be found in Bhaskaran and Lele (2010).

2.1.3 Time Integration

Far away from the solid boundaries, the governing equations are integrated using an explicit third-order compact storage Runge-Kutta scheme (Wray, 1986). After the spatial discretization, the set of partial differential equations become a set of ordinary differential equations that can be expressed in the form

$$\frac{dQ}{dt} = f(Q, t). \tag{2.7}$$

This set of ordinary differential equations can be integrated from t^n to t^{n+1} using the following third-order Runge-Kutta scheme

$$\begin{aligned} Q^{n+1/3} &= Q^n + \frac{8}{15}\Delta t f(Q^n, t^n) \\ Q^{n+2/3} &= Q^n + \frac{1}{4}\Delta t f(Q^n, t^n) + \frac{5}{12}\Delta t f(Q^{n+1/3}, t^{n+1/3}) \\ Q^{n+1} &= Q^n + \frac{1}{4}\Delta t f(Q^n, t^n) + \frac{3}{4}\Delta t f(Q^{n+2/3}, t^{n+2/3}), \end{aligned}$$

where the intermediate time levels are $t^{n+1/3}$ and $t^{n+2/3}$.

The time integration of the fluid equations is carried out by a fully implicit second-order Beam-Warming scheme (Beam and Warming, 1978) in the near-wall region in order to overcome the time step restriction. The second-order implicit method is given by

$$\frac{3Q^{n+1} - 4Q^n + Q^{n-1}}{2\Delta} = f(Q^{n+1}, t^{n+1}). \tag{2.8}$$

The right hand side is solved through approximate factorization followed by diagonalization of the implicit matrix in the x and z directions. Details about the approximate factorization are presented by Nagarajan (2004).

2.1.4 Boundary Conditions

Sponge layers and characteristic boundary conditions based on Riemann invariants are applied at inflow and outflow boundaries. For a subsonic inflow boundary, four incoming quantities must be specified along with one outgoing quantity computed from the interior domain. In the current study, the entropy, tangential and spanwise velocities and incoming Riemann invariant will be constrained. The outgoing Riemann invariant can then be computed by extrapolation from the interior nodes neighboring the inflow boundary. For a subsonic outflow boundary, one incoming quantity must be specified along with four outgoing quantities computed from the interior domain. Here, the incoming Riemann invariant should be imposed and the entropy, tangential and spanwise velocities and outcoming Riemann invariant can be computed by extrapolation from the interior nodes neighboring the outflow boundary. A damping sponge layer will also be applied along the inflow and outflow boundaries to minimize reflections of disturbances (Nagarajan, 2004; Bhaskaran and Lele, 2010).

Adiabatic, no-slip boundary conditions will be applied at the solid boundaries. The wall density can be obtained by the solution of the continuity equation (Eq. 2.1). The momentum and energy equations are replaced by the constraints on the velocity ($\rho u_i = 0$) and temperature ($\partial T/\partial n = 0$), where the term $\partial(.)/\partial n$ represents a derivative in the wall-normal direction.

2.2 Empitical criteria for dynamic stall onset

2.2.1 Leading edge suction parameter (LESP)

Having an indication of massive dynamic flow separation near the leading edge is of paramount importance for understanding the onset of the dynamic stall. This will allow the construction of dynamic stall models and the definition of control strategies for mitigation of the DSV. In that sense, Ramesh *et. al* (2014) recently proposed a new stall onset criterion based on the idea that an airfoil can support a maximum amount of leading edge suction. By calculating the first term, A_0, of the Fourier series for the distribution of vortex sheet strength along the camber line in thin airfoil theory, they have numerically observed a critical threshold of suction when the leading edge vortex is being formed. When this limit is exceeded, vorticity is released from the leading edge to give rise to the dynamic stall vortex. The term A_0 was referred to as leading edge suction parameter (LESP) and it depends on the airfoil shape and flow Reynolds number, being independent of the airfoil kinematics, except in scenarios where a large trailing edge flow separation is present.

Since most occurrences of dynamic stall exhibit some degree of trailing edge separation and flow reversal, a new quantifiable feature was proposed by Deparday and Mulleners (2019) to predict the dynamic stall vortex inception together with an improved model of the LESP. In their approach, critical values of the chord normal shear layer height and the airfoil circulation were observed to be invariant to motion and, thereby, being better indicators of dynamic stall onset. The LESP model was also modified by the previous authors to account for the evolution of the shear layer during the stall development.

As discussed by Ramesh *et. al* (2014), the LESP parameter A_0 can be used to indicate the onset of the DSV, which occurs when the maximum value of this parameter is achieved. According to Deparday and Mulleners (2019), the LESP can be computed directly from numerical or experimental data as

$$A_0 = \mathrm{sgn}[\cos(\lambda-\alpha)]\sqrt{\frac{2}{\pi}\|\vec{S}_{LE}\||\cos(\lambda-\alpha)|}\ . \tag{2.9}$$

In Eq. 2.9, α is the effective angle of attack and λ is the angle formed between the incoming flow and the leading edge suction vector $\vec{S}_{LE}$. This vector is determined by integrating the pressure signals along the first 10% of the airfoil chord. Hence, $\vec{S}_{LE}$ gives the net force from the surface pressure integration. Here, the sign function is included to yield a continuous result when $\cos(\lambda-\alpha)$ goes from positive to negative and vice-versa. A schematic representation of the terms used to evaluate A_0 according to Deparday and Mulleners (2019) is presented in Fig. 2.1 (a). In this figure, the 10% frontal portion of the airfoil chord is colored in blue and the chord line is shown by a dashed line.

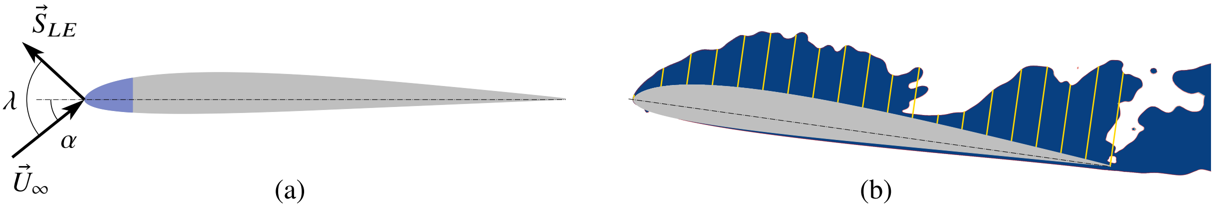

Figure 2.1: Schematic of the relevant parameters used in the calculation of the LESP (a) and entropy measure showing the evaluation of the chord-normal shear layer height (b).

2.2.2 Chord-normal shear layer height

The applicability and reliability of the LESP hinge upon a prior knowledge of the critical thresholds of the leading edge suction as a function of the parameters of the airfoil motion. However, the dependency of this suction on the kinematics and flow compressibility impairs its usage as a universal dynamic stall onset indicator for several realistic flow applications. With the aim of overcoming this limitation, the shear layer height criterion proposed by Deparday and Mulleners (2019) was shown to be a more precise, motion independent, indicator although not easily accessible outside of a laboratory environment.

In this previous reference, the shear layer height was evaluated through an averaged location of clockwise rotating shear layer vortices identified using an Eulerian vortex criterion from the individual snapshots of the velocity field. Here, as we know the values of all conserved variables from the numerical simulation, it is possible to estimate the chord normal shear layer height, Δz, in a simpler manner. We compute contours of an entropy measure and select a small threshold (0.05 in this case) as a limit for the viscous region. A representation of the procedure is shown in Fig. 2.1 (b), where the blue region indicates the portion of the fluid within the limit where entropy values change above the 0.05 threshold. Then, uniformly distributed chord-normal lines are drawn and their distances from the airfoil surface to the entropy contour boundary are measured. These lines are represented in Fig. 2.1 (b) in yellow color and their distances are nondimensionalized by the airfoil chord. Here, 100 lines are used in the analysis, but only a few appear in the figure for better visualization. If a given chord-normal line intersects the limiting entropy level more than once, for instance, in the rightmost yellow line in the figure, a separate distance is computed for each intersection and all such distances are subsequently averaged out to obtain Δz.

2.3 Modal analysis

As experiments and calculations become more advanced, they generate ever-increasing amounts of data. While having a massive amount of data is an advantage, the size of the datasets presents its own challenges. This has led to a growing need for data-driven methods that can take a dataset and meaningfully characterize it with minimal guidance. Several researchers in fluid mechanics have considered modal decomposition as the tool of choice for data-driven analysis (Taira *et. al*, 2017, 2020). Among the different modal decomposition techniques, the proper orthogonal decomposition (POD) is one of the most popular. It was introduced to the fluid dynamics/turbulence community by Lumley (1967) as a mathematical tool to extract coherent structures from turbulent flow fields. Naturally, POD has been widely used in the context of dynamic stall (see Mohan *et. al* (2016); Coleman *et. al* (2019); Lui and Wolf (2019); Mallik and Raveh (2020) to cite a few). The extraction of the POD modes is based on optimizing the mean square of the field variable being examined.

Our hope when performing a modal analysis is that the modes identify features of the data that elucidate the underlying physics. However, there is a foundational theory upon which these decomposition methods can rest. Without sound theory, we may apply or design algorithms that in some cases produce results that we cannot explain or trust. In the case of POD, the data is expected to be a zero-mean second-order stochastic signal. These conditions, though, are hardly satisfied in dynamic stall for the transient nature of the problem. This makes interpreting POD modes from dynamic stall data very difficult. Fortunately, the meaning of the modes depends on the particular type of decomposition used, and there are other options besides POD.

2.3.1 Dynamic mode decomposition (DMD)

Dynamic mode decomposition (DMD) (Schmid, 2010; Tu *et. al*, 2014) is a technique that isolates the most dynamically significant modes containing low-rank flow structures oscillating at a single frequency. The algorithm employed here builds upon the singular value decomposition (SVD) of the snapshot data and computes a finite-dimensional approximation of the infinite dimensional Koopman operator (Tu *et. al*, 2014).

In the algorithm, the dynamical system (which can be nonlinear) is reconstructed as a linear best-fit (least-squares) approximation $\mathbf{X}' \approx \mathbf{AX}$, where matrices $\mathbf{X}$ and $\mathbf{X}' \in \mathbb{C}^{m \times n-1}$ and store the snapshots in columns. Then, the best-fit linear operator $\mathbf{A}$ and its eigendecomposition are evaluated to extract the DMD modes $\mathbf{\Phi}$.

In this section, we provide more details about the DMD algorithm. It proceeds as follows:

1 The snapshots are stored colunmwise in two separate matrices $\mathbf{X}$ and $\mathbf{X}' \in \mathbb{C}^{m \times n-1}$ such that

$$\mathbf{X} = \begin{bmatrix} | & | & & | \\ \mathbf{x}_1 & \mathbf{x}_2 & \dots & \mathbf{x}_{n-1} \\ | & | & & | \end{bmatrix} \quad \text{and} \quad \mathbf{X}' = \begin{bmatrix} | & | & & | \\ \mathbf{x}_2 & \mathbf{x}_3 & \dots & \mathbf{x}_n \\ | & | & & | \end{bmatrix},$$

where $\mathbf{x}_i$, for $i = 1, 2, 3, ..., n$, represent the i-th snapshots. Here, m is the number of grid points and n is the total number of snapshots.

2 The SVD of $\mathbf{X}$ is computed to obtain a low-rank representation of the data as

$$\mathbf{X} \approx \mathbf{U\Sigma V}^*$$

where $\mathbf{U} \in \mathbb{C}^{m \times r}$, $\mathbf{\Sigma} \in \mathbb{C}^{r \times r}$, $\mathbf{V} \in \mathbb{C}^{n \times r}$ and $*$ denotes the conjugate transpose. Here, r is the rank of the reduced SVD approximation to $\mathbf{X}$ and that can be computed using the recent hard-thresholding algorithm of Gavish and Donoho (2014). The matrices $\mathbf{U}$ and $\mathbf{V}$ are named the left singular vectors and right singular vectors of $\mathbf{X}$, respectively, and $\mathbf{\Sigma}$ is a diagonal matrix containing the singular values.

3 The best-fit linear operator $\mathbf{A}$ is computed to map $\mathbf{X}' \approx \mathbf{AX}$ through a pseudo-inverse of the SVD approximation of $\mathbf{X}$:

$$\mathbf{A} = \mathbf{X}'\mathbf{V\Sigma}^{-1}\mathbf{U}^* \ .$$

In practice, however, the operator $\mathbf{A}$ can be prohibitively large for the next step of the algorithm and a matrix similarity $\tilde{\mathbf{A}} = \mathbf{U}^*\mathbf{A}\mathbf{U}$, which defines a low-dimensional approximation of the linear dynamical system $\tilde{\mathbf{x}}_{k+1} = \tilde{\mathbf{A}}\tilde{\mathbf{x}}_k$, is used instead. In this sense, we have

$$\tilde{\mathbf{A}} = \mathbf{U}^*\mathbf{X}'\mathbf{V}\boldsymbol{\Sigma}^{-1} \ .$$

4 The eigendecomposition of $\tilde{\mathbf{A}}$ is computed as

$$\tilde{\mathbf{A}}\mathbf{W} = \mathbf{W}\boldsymbol{\Lambda},$$

where $\mathbf{W}$ is the matrix containing the eigenvectors (stored columnwise) and $\boldsymbol{\Lambda}$ is a diagonal matrix with the corresponding eigenvalues λ_k.

5 The eigendecomposition of the original system is reconstructed using either

$$\boldsymbol{\Phi} = \mathbf{U}\mathbf{W} \quad \text{(Projected)}$$

or

$$\boldsymbol{\Phi} = \mathbf{X}'\mathbf{V}\boldsymbol{\Sigma}^{-1}\mathbf{W} \quad \text{(Exact)}.$$

Each eigenvector ϕ_k of $\boldsymbol{\Phi}$ represents a DMD mode. These two distinct ways to reconstruct the modes occur because Tu *et. al* (2014) showed that the *exact* modes are the actual eigenvectors of matrix $\mathbf{A}$, in contrast to the original definition of Schmid (2010) for the *projected* modes. However, they tend to converge if $\mathbf{X}$ and $\mathbf{X}'$ have the same column spaces.

6 Finally, the initial amplitudes b_k of each mode are found such that the solution is approximated by

$$\mathbf{x}(t) \approx \sum_{k=1}^{r} \phi_k \exp(\omega_k t) b_k = \boldsymbol{\Phi} \exp(\boldsymbol{\Omega} t)\mathbf{b}. \tag{2.10}$$

Here, $\omega_k = \ln(\lambda_k)/\Delta t$ and $\boldsymbol{\Omega}$ is a diagonal matrix whose entries are the ω_k values. There exists different ways to evaluate the initial amplitude. By considering the first snapshot at time $t_1 = 0$, which gives $\mathbf{x}_1 = \boldsymbol{\Phi}\mathbf{b}$, one can evaluate it as

$$\mathbf{b} = \boldsymbol{\Phi}^{\dagger}\mathbf{x}_1,$$

where † stands for the Moore-Penrose pseudo-inverse. Following Tu *et. al* (2014), it is possible to use the principal component (POD) subspace to determine $\mathbf{b}$ through less expensive computations as

$$\mathbf{b} \approx (\mathbf{W}\boldsymbol{\Lambda})^{-1}\alpha_1,$$

where α_1 is obtained from the matrix product $\mathbf{\Sigma V}^*$ associated with the first snapshot, *i.e.*, $\mathbf{x}_1 \approx \mathbf{U\Sigma V}^* = \mathbf{U}\alpha_1$. As proposed by Jovanović *et. al* (2014), another possibility to calculate $\mathbf{b}$ is given by

$$\mathbf{b} = \left[(\mathbf{W}^*\mathbf{W}) \circ \overline{(\mathbf{V}_{and}\mathbf{V}^*_{and})}\right]^{-1} \overline{\mathrm{diag}(\mathbf{V}_{and}\mathbf{V\Sigma}^*\mathbf{W})},$$

where, in this case, $*$ denotes the self-adjoint (Hermitian) operator while the overline is the complex-conjugate. The term $\circ$ represents the elementwise multiplication and $\mathbf{V}_{and}$ is the Vandermonde eigenvalue matrix.

This classical DMD approach has been used for analyzing unsteady flow features in several applications, for example in jets (Semeraro *et. al*, 2012), cavities (Seena and Sung, 2011), wakes (Muld *et. al*, 2012), detonation waves (Massa *et. al*, 2012) and also in dynamic stall (Dunne *et. al*, 2016; Mohan *et. al*, 2016), as mentioned earlier. In this work, we also employ a recent variation of DMD labelled as multi-resolution DMD (mrDMD). The implementation for both algorithms can be found in the PyDMD package (Demo *et. al*, 2018) available at `https://mathlab.github.io/PyDMD/`. It is worth mentioning that the present author is one of the contributors of this project.

2.3.2 Multi-resolution dynamic mode decomposition (mrDMD)

This algorithm variant consists of a recursive computation of DMD to remove low-frequency, or slowly varying, features from the collection of snapshots (Kutz *et. al*, 2016). Its primary advantage stems from its ability to separate long-, medium-, and short-term trends in data. The resulting output, then, provides a means to better analyze transient or intermittent dynamics that the normal DMD fails to capture. Furthermore, the mrDMD is able to handle translational and rotational invariances of low-rank embeddings that are often undermined by other SVD-based methods.

In a wavelet-based manner, the time domain is divided into two segments recursively to create multiple resolution levels until a desired termination. Since only the lowest frequencies are removed from each bin, data can be sub-sampled to increase computational efficiency. Denoting by L, J and m_l the number of decomposition levels, temporal bins per level, and modes extracted at each level l, respectively, the dynamical system is expressed as

$$\mathbf{x}(t) = \sum_{l=1}^{L}\sum_{j=1}^{J}\sum_{k=1}^{m_l} f^{l,j}(t)\phi_k^{(l,j)} \exp(\omega_k^{(l,j)}t)\, b_k^{(l,j)}.$$

In the expansion above, $f^{l,j}(t)$ is an indicator term that acts as a sifting function for each temporal bin and is defined as

$$f^{l,j}(t) = \begin{cases} 1, & t \in [t_j,\, t_{j+1}] \\ 0, & \text{elsewhere} \end{cases}, \quad \text{with } j = 1, 2, \ldots, J \text{ and } J = 2^{(l-1)}.$$

Artificial high-frequency oscillations may be introduced by the hard cutoff of the time series in each sampling bin but they are naturally filtered out by the lowest frequency selection during the recursion. For a detailed description of the mrDMD algorithm the reader is referred to Kutz *et. al* (2016).

2.4 Convolutional neural networks (CNNs)

Part of this study consists of designing a CNN architecture to capture relevant flow structures and establish a mapping relationship between these structures and the aerodynamic coefficients on the airfoil. Both the location and the morphology of the flow structures with respect to the airfoil must be properly inferred by the neural network for an accurate estimation of the aerodynamic loads. For that, we used convolutional neural networks (CNNs) for their success in identifying flow features (see §1.3). It is worth mentioning that this is an ongoing study. Although preliminary, the results presented in this thesis are very promising.

Unlike other supervised machine learning approaches, CNNs are pattern recognition algorithms that discover meaningful features, in essence making a feature vector, and then extract information from these features in order to make inferences. An important milestone in computer vision was the famous LeNet-5 architecture proposed by Lecun *et. al* (1998), which introduced the building blocks used in modern CNNs: the convolutional layers and the pooling layers. The last few layers in the network are composed of fully connected layers that compile the data extracted by previous layers to form the final output.

Convolution is a mathematical operation that slides one function over another and measures the integral of their point-wise multiplication, acting as a weight averaging method. A convolutional layer contains a series of filters known as convolutional kernels, each taking a summation of Hadamard product of a subset of the input pixel values and a corresponding value in the kernel. This kernel, then, strides over the input matrix to scan the entire data/image. The pooling layer, in turn, subsamples the input data in order to reduce the computational load, the memory usage, and the number of parameters. By doing so, it also limits the risk of overfitting and introduces some level of invariance to small translations (Lecun *et. al*, 1998). Dropout is another regularization method usually applied to the fully connected layers to prevent overfitting (Krizhevsky *et. al*, 2012).

2.4.1 Input data

The starting point of the method is the input images of fluid flow fields, such as those from a 2D cross section or spanwise averaged data. Any physical property of interest could be used as input of the network. Here, we trained a CNN that takes u- and v-velocity components as input and another one that uses the pressure coefficient (C_p) field. The reason behind these quantities is because the velocity field can be directly obtained experimentally, through PIV technique, and the pressure is closely related to the airfoil aerodynamic loads. Figure 2.2 shows examples of images used as input to the CNN. These images are not at scale, though. They had to be resized to fit in the present document.

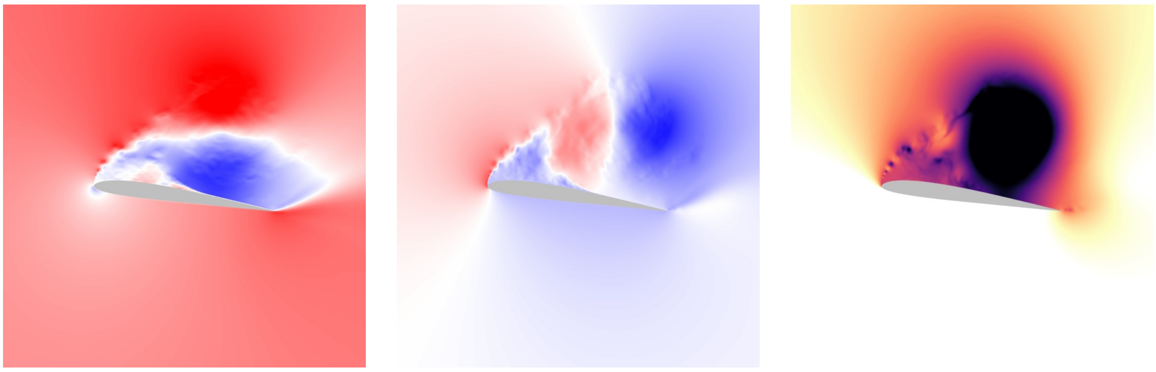
(a) u-velocity (b) v-velocity (c) C_p

Figure 2.2: Examples of images used as input to the CNN.

Our dataset consists of nearly 20,000 RGB images for each physical property and of size 600 × 600 pixels each. These images consider all simulations of dynamic stall cases reported in this manuscript, which include the periodic plunging airfoil and the constant ramp pitching and plunging motions for Mach numbers 0.1 and 0.4. When generating the images, it is important to keep a fixed range for the contour levels of the property of interest. We used the values $[-2, 2]$ for both velocity components and $[-4, 0]$ for C_p. Notice that the velocity components are already non-dimensionalized by the freestream velocity. Finally, this collection of images was shuffled and arbitrarily divided into groups of nearly 16,000, 2,000 and 2,000 images to form the training, validation and test sets respectively.

Data augmentation is used to artificially increase the size of the training set. Realistic variants of each training instance were generated by shifting, rotating, and resizing every picture through preprocessing layers (Shorten and Khoshgoftaar, 2019). The transformations applied to the input images are only geometrical and, therefore, preserve the semantics of the images. Moreover, the DSV and the entire airfoil are fully framed in all generated instances. In our preliminary study, no noise was added to the generated instances. Although PIV images contain a substantial amount of noise (Scharnowski and

Kähler, 2016), we did not apply our model to PIV data just yet. In fact, we are eager to access experimental data to proceed with this study. In this case, we expect that the network will perform better after being trained with noisy data.

2.4.2 Fine tuning

Initially, many attempts were made to build sequential models of convolutional, pooling and fully connected layers capable of predicting the aerodynamic coefficients from flow field images. The number of layers, the size of each layer and the number of filters were varied, generating models containing from nearly 3,000,000 to more than 52,000,000 parameters. These networks were built from scratch with randomly initialized weights and employed L2 regularization and dropout techniques to prevent overfitting. Using the framework of maximum likelihood estimation, the mean-square-error cost function is preferred for regression problems, but here we used the logarithm of the hyperbolic cosine function (logcosh) as it is not strongly affected by occasional wildly incorrect predictions. Different activation functions, such as ReLU and ELU (Clevert *et. al*, 2015), and different optimizers, such as Adam (Kingma and Ba, 2015) and Nadam (Dozat, 2016), were tested. However, despite the many combination of hyperparameters covered, virtually all resulting models were highly biased, meaning that they were too simple to learn the underlying structure of the data. Due to the unsuccessful attempts using these simple sequential models, we took a different turn and used transfer learning.

Transfer learning is a useful approach to speed up training considerably while also requiring significantly less training data to bootstrap computer vision models (Zhuang *et. al*, 2021). It consists of using pre-trained models to leverage features learned on one problem and use them on another problem. Here we used many architectures pre-trained on the ImageNet dataset, which are readily available for Tensorflow Abadi *et. al* (2015) via Keras API (Chollet *et. al*, 2015). That is the tool we employed in this work. Even though pictures related to fluid flow problems are absent from ImageNet, the method used generalize well to our dynamic stall problem. However, as some of these architectures contain many parameters, running them can be expensive, especially when working on CPUs. So we used the strategy described by Chollet (2016a) to train our network in a computationally efficient way for transfer learning. It goes as follows:

1. Instantiate a pre-trained model (in §2.4.3 we show the architectures we used) taking only the convolutional part, up to the fully connected layers.
2. Run this model on the training and validation data only once and record its output. We call this output "bottleneck features" for it is the activation maps immediately before the fully connected layers.

3. Define a fully-connected model to add on top of the convolutional base. But before that, train this small fully-connected model separately, using the bottleneck features as input. This step prevents the large gradient updates triggered by the randomly initialized weights from wrecking the learned weights in the convolutional base. Also, by doing so, the computational efficiency is improved. At this stage, an arbitrary value of 15 epochs is considered for training.
4. Add the previously trained fully-conected layers on top of the convolutional base.
5. Fine-tune the convolutional block with a very slow learning rate to make sure that the magnitude of the updates will not wreck the previously learned features. In this sense, SGD optimizer is preferred.

The pre-trained models assume that the images are pre-processed in a specific way. Hence, the pre-processing step is not only used for data augmentation, but also to properly scale the pixel range or resize the picture to the size expected by the original model. All layers were trained using 300 epochs with an early stopping of 50 epochs based on the mean-square-error metric.

2.4.3 CNN architectures

A few CNN architectures were selected to solve our regression problem. Among them, we have the VGG16 (Simonyan and Zisserman, 2015), the InceptionV3 (Szegedy *et. al*, 2016), the Xception (Chollet, 2016b) and the EfficientNet-B3 (Tan and Le, 2019). The VGG16 is a simple and classical architecture built from the stack of groups of 2 or 3 convolutional layers, each followed by a pooling layer. By using very small filters (3×3), the VGG16 pushes the depth to 16 weight layers totaling approximately 138 million parameters.

The InceptionV3, in turn, uses subnetworks called inception modules, which were initially proposed by Szegedy *et. al* (2015). These modules allow for more computationally efficient and deeper networks through a dimensionality reduction with stacked 1×1 convolutions. In an InceptionV3 model, several techniques for optimizing the network have been put for easier model adaptation. This includes exploring factorized and asymmetric convolutions, and the use of an auxiliary classifier as a regularizer. A high-level diagram of the model is shown in Fig. 2.3 below. It is worth mentioning that only the convolutional blocks were fine-tuned in the present work and the dense layers, and thereby the output, is not identical to the one shown in the figure.

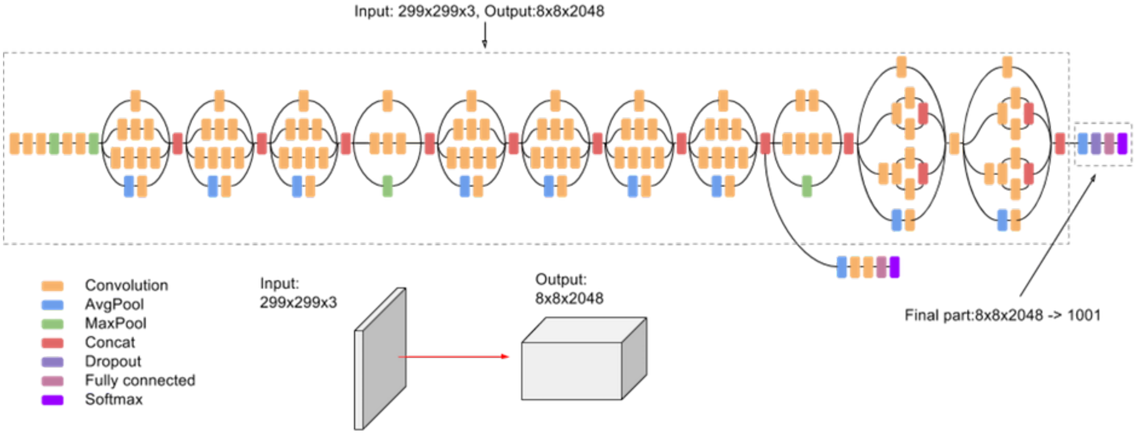

Figure 2.3: Diagram of an InceptionV3 network. The dense layers (denoted as "Final part" in the figure) and the output were modified in the present work. Digital image extracted from Advanced Guide to Inception v3, accessed 12 August 2022 <`https://cloud.google.com/tpu/docs/inception-v3-advanced`>

Another variant of the architecture proposed by Szegedy *et. al* (2015) is the Xception network (Chollet, 2016b). It relies on the concept of depthwise separable convolutions, which splits the channelwise and spatial-wise computations into two steps. The depthwise convolution applies a single convolutional filter per each input channel, while pointwise convolution is used to create a linear combination of the output of the depthwise convolution. Inception module reverses these operations. Compared with conventional convolutions, it is not necessary to perform convolution across all channels, resulting in fewer operations and a lighter model. In addition, the Xception extensively uses residual connections (He *et. al*, 2016) and does not apply non-linearity (ReLU or ELU) after the depthwise operation.

Finally, the family of EfficientNet architectures (Tan and Le, 2019) worked towards balancing network depth, width and resolution to improve performance. Based on the intuition that if the input image is bigger, then the network needs more layers to increase the receptive field and more channels to capture more fine-grained patterns on the bigger image, the authors proposed a new scaling method that uniformly scales all dimensions of depth/width/resolution using a compound coefficient. Here we chose the EfficientNet-B3 variant for its relatively few number of parameters, compared to the aforementioned architectures, and its accuracy.

As mentioned in the previous section, only the convolutional block of these pre-treined models is used in our work. In fact, these networks were trained on classification problems, whereas, here, we are interested in a regression task. Therefore, it is necessary to change the top layers of the network to adjust them to our problem. How this is done will depend on the number of outputs we want the neural network to have. In this sense, two different fully-connected layers were designed to meet two distinct objectives: (1) finding integrated aerodynamic coefficients, such as lift, drag and the quarter-chord pitch moment coefficient; and (2) finding the distribution of pressure coefficient over the airfoil suction side. While in the former we only need 3 outputs (lift, drag and pitch moment), the latter needs to be a large array to store the entire load distribution over the airfoil surface. Here, we used the 337 grid points that compose the airfoil suction side in our numerical simulation. Using grid points is acceptable in our case since all simulations used the same mesh. To keep the data independent of the mesh, one can interpolate the results to specific points on the airfoil surface and then use this data as output to train the network. That said, we have the following fully-connected layers for each case:

1. **Lift, drag and pitch moment:** One dense layer of 256 units that uses the ELU activation function and L2 normalization, followed by a dense layer of 3 units with linear activation.

2. **Pressure coefficient distribution:** Two dense layers of 512 units that use the ELU activation function and L2 normalization, followed by a dense layer of 337 units with linear activation.

2.4.4 Image synthesis

In addition to the regression model to obtain aerodynamic coefficients from images of the flow, we are also interested in expanding the amount of information extracted from experiments. While these two things might be somewhat related, we refer to them separately. This is because we create a model to obtain the coefficients, and another one to extract other information from the flow. Here, for example, this other information consists in images. For this, we need to train a neural network capable of receiving images of the flow as input and generating another image as output.

The motivation for this image-to-image translation stems from the fact that any physical properties can be obtained from a numerical simulation, while the range of information extracted from experiments is very limited or too complex to be acquired. Although the flow field resulting from a numerical simulation can significantly vary from an experimental flow visualization of the same problem, there exists common high-level semantics between them.

Image synthesis with supervised machine learning is the process of artificially generating images that contain some particular desired content, associated with a specific label. The most prominent machine learning model for generating content is known as generative adversarial networks (GANs) (Goodfellow *et. al*, 2014). The GAN is based on game theory, where we have two networks competing with each other to generate the best segmentation. One neural network, called the generator, generates new data instances, while the other, the discriminator, evaluates them for authenticity. But, differently from the aforementioned networks, GANs are fully convolutional networks

(FCN) (Long *et. al*, 2015), which are similar to a common convolution neural network, but the fully connected layers are typically replaced by transposed convolutional layers. These transposed convolution, first introduced by Zeiler *et. al* (2010), allows one to upsample the input feature map to a desired output feature map using some learnable parameters.

Certainly, the nature of having a discriminator model in a GAN provides us with output-target differences on the pixel level, which emerges from a deeper understanding of the images. However, GANs are often difficult to train and tune (Gui *et. al*, 2021), and a simpler approach to synthesize an image is to use the U-net (Ronneberger *et. al*, 2015), a network developed to work with fewer training images and produce accurate biomedical image segmentation. This network resembles an encoder-decoder structure, but with the addition of skip connections that are used to transfer fine-grained information from the low-level layers of the contracting path to the high-level layers of the expanding path. The U-net combines a pixel-wise softmax over the final feature map with the cross entropy loss function. For its simplicity, it is the architecture that we will use in the present work.

In our implementation of the U-net, the images of the velocity components are resized to 256×256 pixels and concatenated channelwise. Hence, we have the following architecture shown in Fig. 2.4:

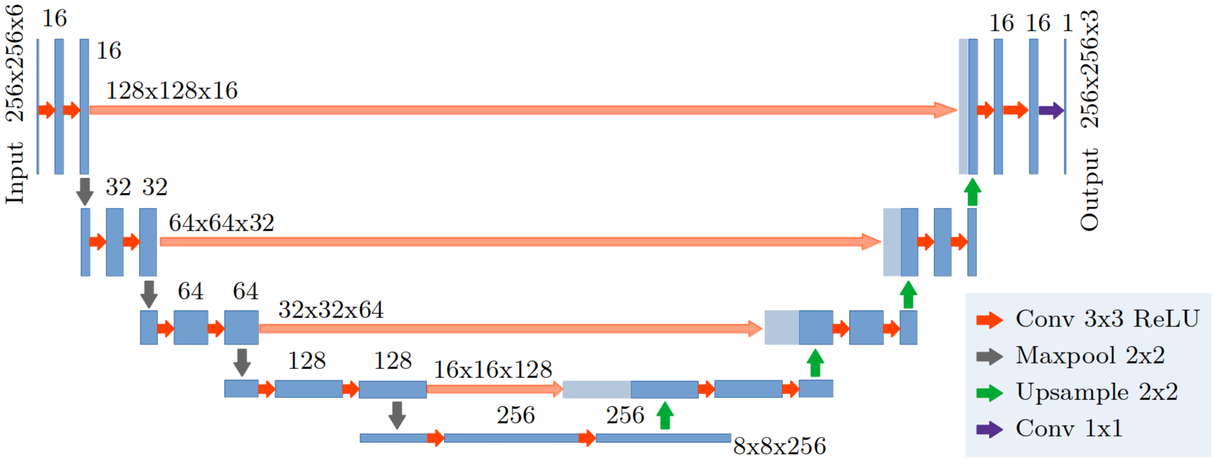

Figure 2.4: U-net architecture.

2.4.5 Domain adaptation

In the present work, we seek to adapt a model trained with annotated C_p field samples from CFD simulations (source), to operate on an experimental (target) distribution, for which no annotations are given. However, the covariance shift that occurs due to different distributions between source and target often causes model performance to deteriorate on target data (Wang and Deng, 2018). To address this issue without any need for training beyond the primary task of our image-to-image translation, we use the unsupervised domain adaptation (UDA) method proposed by Yang and Soatto (2020). Their method minimizes the distributional misalignment across different domains by replacing the low-level frequencies of the target images into the source images using the fast Fourier transform. As a result, the original model trained only on a given source distribution generalizes better across different domains.

3 Dynamic stall onset

Two different freestream Mach numbers are investigated in this work to assess compressibility effects on deep dynamic stall of a periodic plunging airfoil. Simulations are performed for $M_\infty = 0.1$ and 0.4, the former being also studied by Visbal (2011), Mohan *et. al* (2016) and Ramos *et. al* (2019). Mesh refinement and domain extension studies are discussed by the references previously cited and, in the present work, we employ the same grid resolution used by Ramos *et. al* (2019), which has $480 \times 350 \times 96$ (≈ 16 million) points along a $z/c = 0.4$ span. An extensive literature (see Visbal (2011); Visbal and Garmann (2018) and Benton and Visbal (2019b, 2020) for instance) provides compelling evidence that this spanwise extension is sufficient to accurately capture the aerodynamic loadings and the relevant dynamics associated with the dynamic stall onset. The studied configuration comprises an SD7003 airfoil at $\alpha_0 = 8^\circ$ static angle of attack. The airfoil trailing edge is rounded with an arc of radius $r/c = 0.0008$ to facilitate the use of an O-mesh topology and to keep metric terms smooth.

It is worth mentioning that, in this work, we employ the same numerical method and grid used by Ramos *et. al* (2019) for the $M_\infty = 0.1$ flow, whose results compare well with those from Visbal (2011), both in terms of local flow structures and integrated loads. However, in order to validate the results for $M_\infty = 0.4$, a refined grid of size $576 \times 444 \times 120$ (≈ 31 million points) was designed to have 25 to 40% improvement in resolution on the suction side, depending on the direction, after a localized distribution of points. Computations showed an excellent agreement between the two grids and, hence, results will be shown only for the smaller grid.

The airfoil vertical displacement $h(t)$ is specified as a function of nondimensional time t, reduced-frequency k and maximum plunge amplitude h_0 as

$$h(t) = h_0 \sin(2kt). \tag{3.1}$$

Here, the parameters are set as $k = 0.25$ and $h_0 = 0.5$ to reproduce the deep stall flow configuration studied by Visbal (2011) and Ramos *et. al* (2019). Although the numerical formulation uses a non-dimensionalization of flow velocities and time scale by speed of sound, the parameters in Eq. 3.1 are based on the freestream velocity, similar to the previous references. The maximum plunging amplitude is normalized by the chord length and the airfoil undergoes a variation in effective angle of attack in the range of $-6^\circ \leq \alpha_{eff} \leq 22^\circ$.

For the present plunging airfoil at $M_\infty = 0.1$, Ramos *et. al* (2019) show that discarding the first cycle is sufficient to remove transient features from the numerical procedure, which assumes an initial uniform flow in the entire domain. We performed the computation of another cycle for $M_\infty = 0.4$ and observed similar changes in the aerodynamic coefficients compared to those shown by Ramos *et. al* (2019). Hence, results are shown for the second cycle and, although cycle-to-cycle variations indeed occur, we emphasize that the effort here is to focus on the onset of dynamic stall, where one cycle should be sufficient to capture the main trends associated to the formation of the DSV. Phase-averaged results of this case can be found in Visbal (2011) and Ramos *et. al* (2019), and the effects of cycle-to-cycle variations are discussed by the latter authors. It is also important to note that, differently from the previous references, here, we define the reference position for the phase angle $\phi = 0°$ at $h(t) = 0$ and not at the topmost position $h(t) = h_0 = 0.5$. This difference is just a matter of preference. Therefore, at $\phi = 0°$ the airfoil is moving upward with maximum vertical velocity. The airfoil reaches the topmost position at $\phi = 90°$ with zero vertical velocity and, then, starts the descending motion. At $\phi = 180°$ it has the maximum downward velocity and at $\phi = 270°$ it reaches the bottom-most position. Then, it moves upward and repeats the cycle.

3.1 General flow features

Figure 3.1 shows the lift (C_l), drag (C_d) and pitching moment (C_m) coefficients as a function of the effective angle of attack for freestream Mach numbers $M_\infty = 0.1$ and $M_\infty = 0.4$. The dashed blue lines indicate the phase-averaged coefficients obtained by Visbal (2011) after six cycles, for $M_\infty = 0.1$. From this figure, a good agreement is observed between the present results and those from Visbal, despite the differences in the numerical methods, computational grids and phase averaging effects. At this point, it is important to reiterate that our results display the aerodynamic loadings for a single cycle, and that they lie within the cycle-to-cycle variations shown in Visbal's work. The dashed red lines, in turn, stand for the results obtained by 1 cycle of the $M_\infty = 0.4$ flow with the finer grid. Differences observed are due to the sensitivity of the flow to the initial conditions, as it would occur due to cycle-to-cycle variations. The phase angle ϕ is also shown in the plots for particular instants of the motion, and the circle and cross symbols on C_l and C_d plots mark the dynamic stall onset time based on different criteria (further details provided in § 4.6). It is observed that compressibility acts on the sense to attenuate the aerodynamic loads in the hysteresis loop while maintaining their maximum and minimum values, a trend that was also observed by Sangwan *et. al* (2017) for a two-dimensional simulation of a pitching airfoil. Here, we observe that the largest changes in C_l and C_d occur when the effective angle of attack is reduced from $\alpha_{eff} \approx 18°$ to $10°$, which corresponds to the time interval when the airfoil is ceasing its downstroke motion. At $\alpha_{eff} = 8°$, the airfoil is at the bottom-most position for the downstroke.

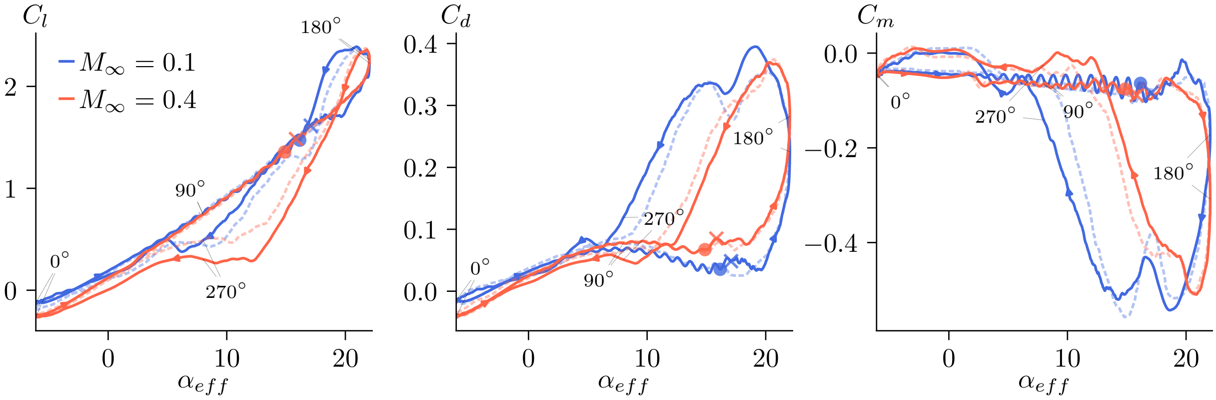

Figure 3.1: Lift, drag and pitching moment coefficients as a function of the effective angle of attack for $M_\infty = 0.1$ and 0.4. Dashed blue lines are phase-averaged results from Visbal (2011) and dashed red lines are results for $M_\infty = 0.4$ with a finer grid. Circle and cross symbols represent onset time based on LESP and Δz criteria, respectively (see § 4.6).

These results, especially the accentuated decay of the coefficients during the post-stall period with the increasing Mach number, can be better understood from Figs. 3.2 and 3.3. The former exhibits the spanwise-averaged pressure coefficient (C_p) contours at different flow instants for the two Mach numbers investigated (first two rows) and its distribution over the airfoil suction side (bottom row). The formation of the DSV is also shown in gray shade using a flow entropy measure defined as $(p/p_0)/(\rho/\rho_0)^\gamma - 1$, where $p_0 = 1/\gamma$ and $\rho_0 = 1$ are reference values for pressure and density, respectively. This entropy measure gives a better visual representation of the separated flow since it indicates the regions where entropy is changing due to viscous effects. The latter figure presents the full history of pressure (C_p) and skin friction (C_f) coefficients along the suction side of the airfoil.

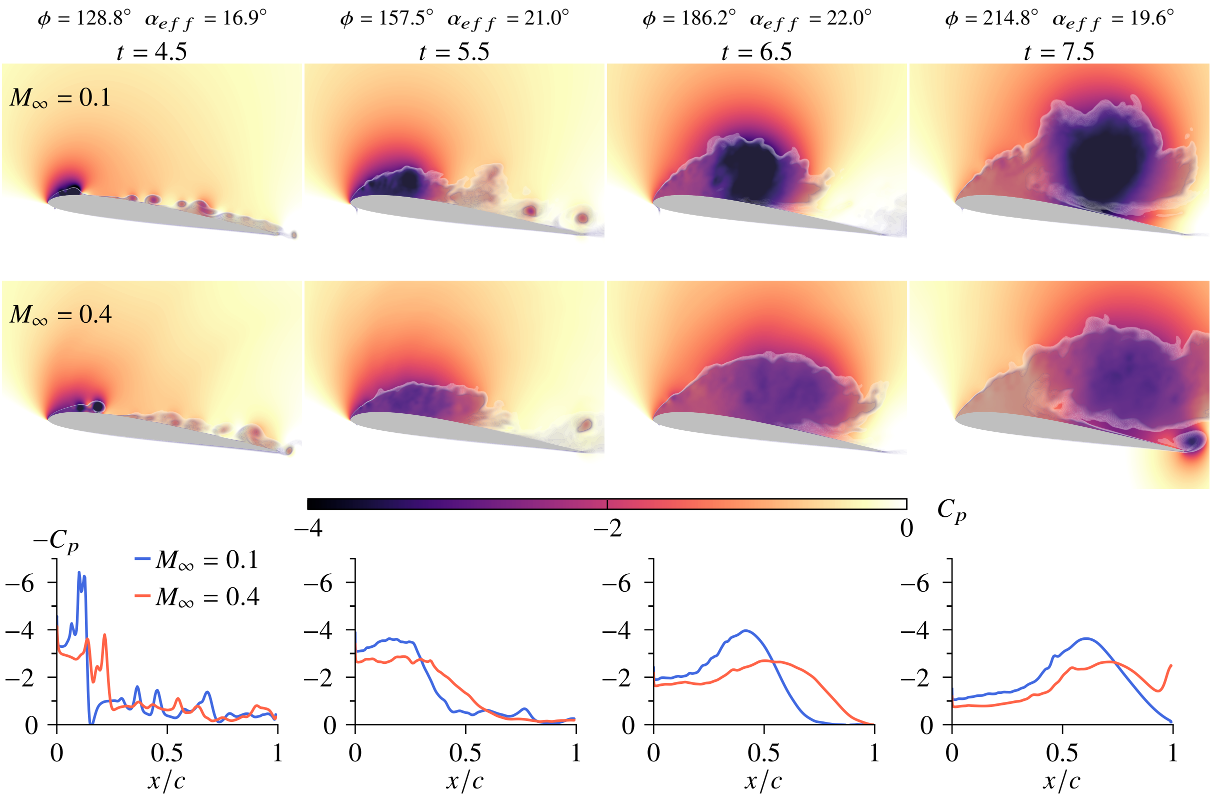

Figure 3.2: Spanwise-averaged pressure coefficients at different flow instants for $M_\infty = 0.1$ (first row) and $M_\infty = 0.4$ (second row), and C_p over the airfoil suction side (third row). The evolution of the DSV can be seen in the supplemental movie at `https://doi.org/10.1017/jfm.2022.165`.

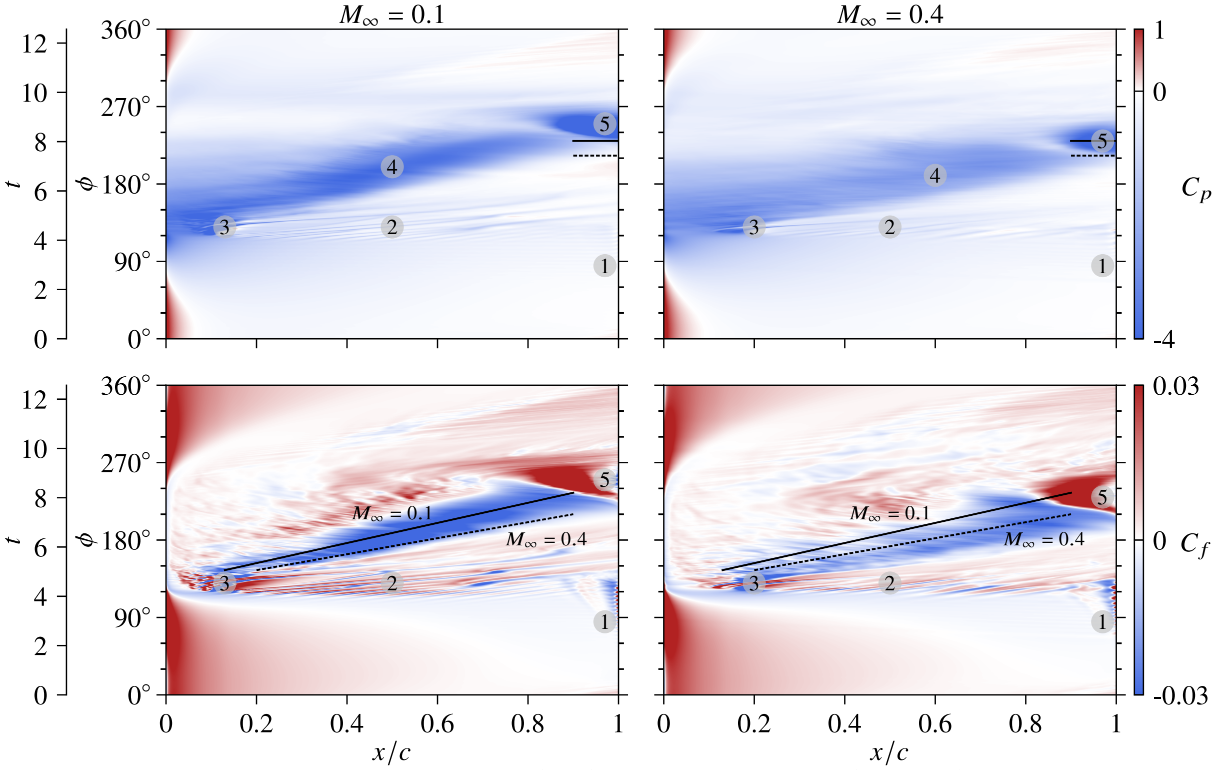

Figure 3.3: Comparison of pressure (top) and skin friction (bottom) coefficients for $M_\infty = 0.1$ (left) and $M_\infty = 0.4$ (right). Auxiliary lines and markers are included to facilitate the comparison between the two flows and to represent specific events as described in the text.

From Fig. 3.2, two immediate observations can be drawn. The first is that the suction peak is reduced near the leading edge for the higher Mach number flow, as demonstrated in the bottom row of the figure for $t = 4.5$. This condition is accompanied by a weaker, more diffuse, pressure core of the DSV. The second concerns the gestation period and residence time for which the DSV remains over the airfoil. A heuristic reasoning to explain the weakening of the DSV strength with compressibility is provided by Chandrasekhara and Carr (1990). They argue that, for higher Mach numbers, the pressure gradient is reduced near the leading edge due to the smaller curvature of the streamlines from the earlier flow separation. At this condition, the net vorticity introduced is lower, which leads to a weaker vortex formation. With respect to the second observation, Fig. 3.2 shows that the DSV residence time is smaller for $M_\infty = 0.4$, and that it is more spread at $t = 6.5$, spanning a larger region over the airfoil suction side. On the other hand, the DSV is relatively concentrated at the mid-chord location for the lower Mach number case. At $t = 7.5$, the DSV is already leaving the airfoil surface for the higher Mach number flow, followed by a trailing edge vortex.

The same conclusions can be drawn from the map of C_p over the airfoil suction side, depicted in the top row of Fig. 3.3. In this x/c - t diagram, the dark blue contours represent the signature of the DSV over the airfoil suction side followed by the formation of the trailing edge vortex. We observe that the C_p contours are lighter for $M_\infty = 0.4$ (see marker #4 in the figures) indicating the presence of a weaker pressure core. Moreover, with closer inspection, it is possible to measure a delay of 17° in the phase angle between the formation of the trailing edge vortex for the two Mach number flows, as indicated by the horizontal black lines on marker #5. The solid and dashed horizontal lines show the initial formation of the trailing edge vortex for the $M_\infty = 0.1$ and 0.4 cases, respectively. While the trailing edge vortex starts to form at $\phi = 213°$ for $M_\infty = 0.4$, its appearance occurs at $\phi = 230°$ for $M_\infty = 0.1$.

The C_f plots in the lower row of Fig. 3.3 present further information about the flow history over the suction side of the airfoil. At about 90° phase angle, an oscillatory pattern appears close to the airfoil trailing edge as shown by marker #1. These oscillations arise due to initial shedding of von Kármán vortices from the airfoil trailing edge, which exhibit a higher frequency at the lower Mach number flow. This vortex shedding can be better visualized in the supplemental movie at `https://doi.org/10.1017/jfm.2022.165`. In the following moments, high-frequency C_f variations can be observed spanning almost the entire chord (denoted by marker #2) in the range $120 < \phi < 130°$ for both flow conditions, but they are more pronounced for the $M_\infty = 0.1$ case. These fluctuations are due to Kelvin-Helmholtz instabilities forming during the downstroke motion. Figure 3.4 shows this primary instability stage of the flow at different instants using entropy contours. As is evident, the instabilities arise initially closer to the trailing edge but rapidly develop along the entire suction side. They appear to form at an earlier time for the lower Mach number and exhibit a more organized and denser behavior where flow structures display a higher wavenumber.

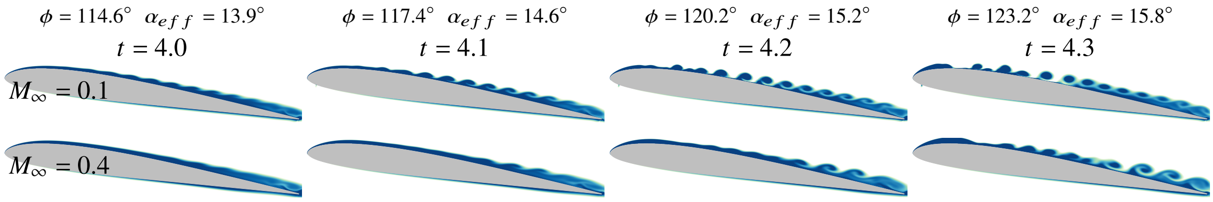

Figure 3.4: Entropy contours showing the development of Kelvin-Helmholtz instabilities (here called the primary instability stage) along the airfoil suction side for $M_\infty = 0.1$ (top) and $M_\infty = 0.4$ (bottom).

For both cases investigated, the formation of the dynamic stall vortex appears just after the Kelvin-Helmholtz instabilities approach the leading edge, at a phase angle $\phi \approx 135°$, shown by marker #3 in Fig. 3.3. In the same figure, the traveling signature of the DSV can be noticed by the negative C_f values shown in blue contours along the airfoil chord for intermediate phase angles ϕ. Auxiliary black lines are included to facilitate the comparison of the mean velocity at which the DSV is being transported for each compressible regime. The lines represent an approximate path of the DSV when moving, considering the center of the blue region. The solid line corresponds to the DSV signature of the $M_\infty = 0.1$ flow while the dashed one refers to the $M_\infty = 0.4$ case. They are repeated in both subplots to facilitate the comparison of their slopes and show that the DSV is being advected faster in the higher Mach number flow. The weaker signature of friction coefficient for $M_\infty = 0.4$ is also noticeable compared to that for $M_\infty = 0.1$.

The skin friction maps in Fig. 3.3 also display the presence of a flow reversal at earlier times that progressively advances over the airfoil suction side from the trailing edge towards the leading edge as ϕ increases. This region appears for $\phi \leq 120$ in light blue contours, below markers #1, #2 and #3. The time (here also visualized as a function of the plunge cycle angle ϕ) in which the flow reversal initiates does not appear to change under the distinct compressible regimes investigated. The main differences in C_f between the two flows start after the beginning of the primary instabilities (marker #2), which are more sparse for the higher Mach number flow. As mentioned before, the transport of the DSV over the suction side is faster for $M_\infty = 0.4$ and its signature is more diffuse. Moreover, the point where the development of the DSV occurs changes from approximately $x/c = 0.1$ for $M_\infty = 0.1$ to $x/c = 0.2$ for $M_\infty = 0.4$ (see different positions of marker #3). This behavior can be better understood through an inspection of the boundary layer forming over the airfoil suction side, which will be discussed in the following section.

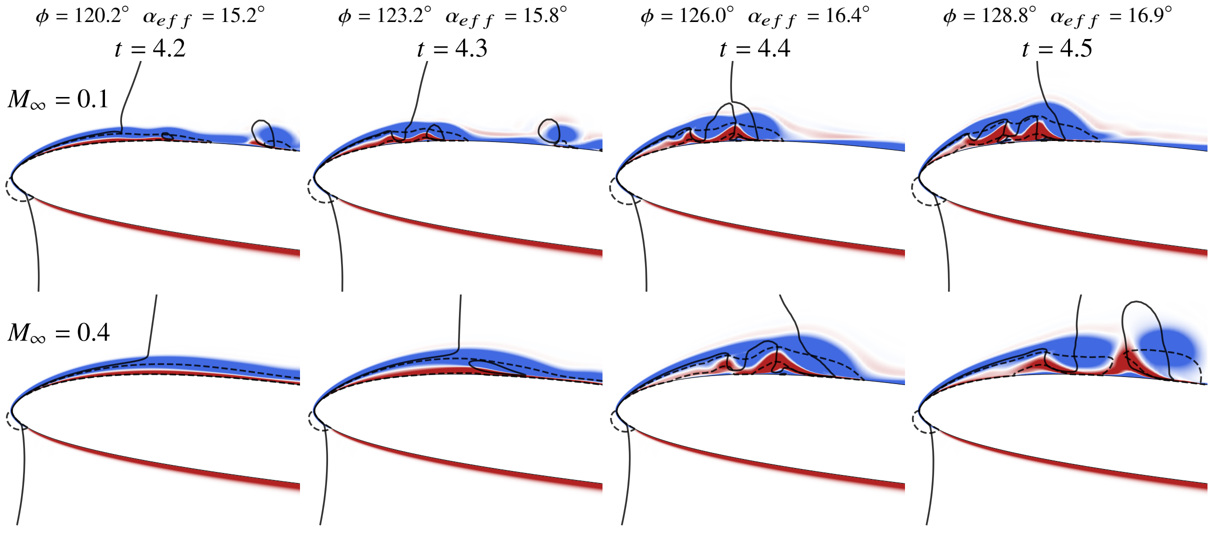

Figure 3.5: Spanwise-averaged z-vorticity field near the leading edge ($x/c \leq 0.25$) revealing the sudden boundary layer separation for $M_\infty = 0.1$ (top) and $M_\infty = 0.4$ (bottom). Dashed and solid lines represent the boundaries for which $u = 0$ and $v = 0$, respectively, indicating flow regions where velocity components change direction.

3.2 Onset of dynamic stall

Figure 3.5 shows the spanwise-averaged z-vorticity contours in a short time window that marks the moment of formation of the DSV. As can be seen from the figure, $\Delta t = 0.3$ based on the freestream velocity, which corresponds to nearly 2.4% of the plunging cycle period. Unlike for steady separation, in dynamic stall the outer flow continues to follow the airfoil contour besides the presence of flow reversal. As a consequence, a local shear layer forms between the displaced leading edge boundary layer and the reversed fluid layer which is, at a later stage, subjected to inflectional instabilities. This leads to the generation and growth of coherent structures that can be visualized in Fig. 3.5. In the figure, auxiliary lines are plotted to indicate regions where u- and v-velocity components change directions, from which we identify the presence of flow reversal and the shear layer over the leading edge.

In previous work by van Dommelen and Shen (1980), it is speculated that the onset of the unsteady separation phenomenon is an inviscid process, independent of the Reynolds number. This characteristic is attributed to the fact that the initial flow reversal near the surface, which is triggered by a strong adverse pressure gradient, is later governed by inertial effects on the zero vorticity line. Along this line, formed as the fluid approaches the separation region, the convective terms dominate over the viscous effects justifying the inviscid assumption. Under the influence of the increasing adverse pressure gradient, the local reversed flow begins to accelerate rapidly upstream near the leading edge region generating an intense shear. Because of the presence of the solid surface, fluid is propelled away from the wall. Meanwhile, the vorticity conservation yields an outward distortion of the zero vorticity line, destabilizing the local vorticity distribution and resulting in the formation of a large vortical structure. The development of this vortex and its induced secondary separation leads to its ejection from the surface.

The process described above is visualized in Fig. 3.6, where the local Mach number is plotted along with the zero-vorticity lines during the dynamic stall onset. In this figure, a straight line measuring $0.06c$ in length is plotted normal to the airfoil surface, from which tangential and normal velocity components are computed to describe the evolution of the local velocity field. The placement of these lines is chosen in order to highlight similar behavior of the velocity field at $t = 4.4$, but since separation occurs at different chord positions depending on the freestream Mach number, they are placed with different distances from the airfoil leading edge for each flow. The values $x/c = 0.11$ and 0.15 are chosen for $M_\infty = 0.1$ and $M_\infty = 0.4$, respectively. We stress that these values are not meant to indicate the precise location of the separation but only to help illustrate the van Dommelen and Shen model. With that clarification, Fig. 3.7 shows the profiles of tangential (u_t) and normal (u_n) velocity components in blue and red colors, respectively. The corresponding vectors are also displayed in the figure. The tail of each vector is placed at the respective normal distance where its velocity components are shown.

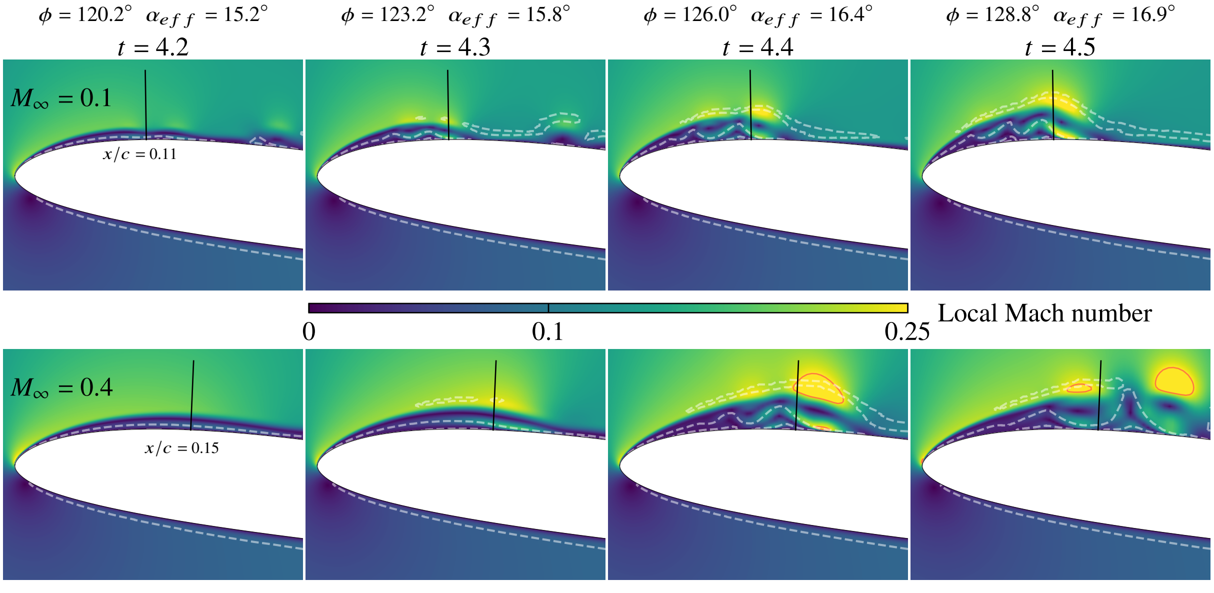

Figure 3.6: Local Mach number contours near the leading edge ($x/c \leq 0.25$) for $M_\infty = 0.1$ (top) and $M_\infty = 0.4$ (bottom). White dashed lines represent the zero-vorticity lines and solid red lines represent regions of sonic flow.

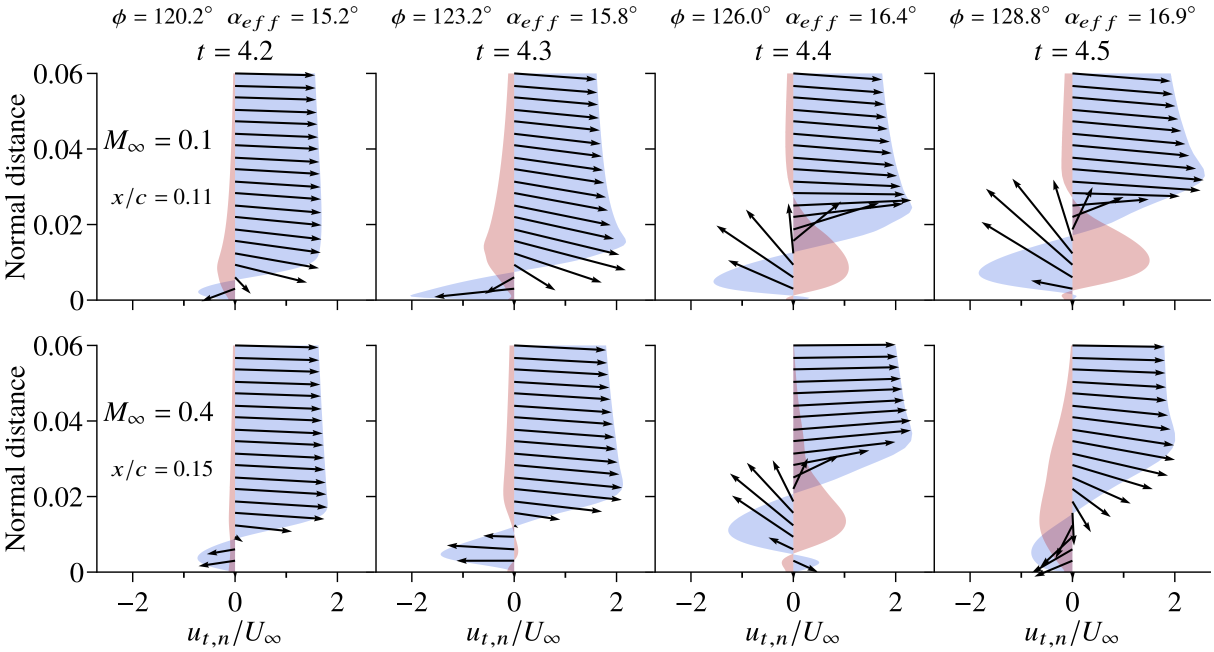

Figure 3.7: Tangential (u_t, blue) and normal (u_n, red) velocity profiles for $M_\infty = 0.1$ (top) and $M_\infty = 0.4$ (bottom).

In Fig. 3.6, the flow continues to accelerate up to a point further downstream of the leading edge where it encounters the reversed flow accelerating along the inner layer in the opposite direction. This acceleration is also evident in the increment of the tangential velocity between the first and second columns in Fig. 3.7. In this region, a mutual interaction is apparent between the outer flow and the flow inside the zero vorticity line to form a low pressure core (not shown). At $M_\infty = 0.4$, the strong acceleration of the reversed flow is sufficient to achieve sonic speeds along the zero vorticity lines (red lines in Fig. 3.6 represent regions of $M = 1$). The flow, however, is decelerated almost isentropically and no shock waves are observed despite the sonic flow regions. The strong shear accompanied by the low pressure on the aft portion of the separation region results in the flow reversal being ejected away from the surface as shown by the velocity vectors in the third and fourth columns of Fig. 3.7. The interaction of the ejected flow with the outer flow creates a vortical structure that intensifies the instabilities in the region. The dynamics observed in Figs. 3.5 and 3.6 appear to agree well with the overall concept of the van Dommelen and Shen model, which provides the description of the flow up to the early stages of separation.

As observed from the previous figures (Figs. 3.5 and 3.6), the onset of the DSV appears further downstream from the leading edge with an increase in Mach number, as was also reported by Chandrasekhara and Carr (1990) and Benton and Visbal (2020) for pitching airfoils. In their work, compressibility caused the leading edge separation to occur at an earlier time and, consequently, at a lower effective angle of attack. Therefore, the separation for higher Mach number flows would experience a less pronounced curvature of the streamlines and a weaker pressure gradient. However, this earlier separation is not observed in our simulations at $\mathrm{Re} = 6 \times 10^4$, suggesting that the pressure gradient reduction may not be a direct consequence of the lower effective angle of attack. It is important to mention that the observations from the previous authors are for higher Reynolds numbers than that considered in the present work.

For the present periodic plunging motion, the leading edge separation seems to be related to the primary instabilities developing at the trailing edge region and, later, spanning the entire airfoil suction side as shown in Fig. 3.4. These instabilities approach the leading edge and interact with the secondary instability presented in Figs. 3.5 and 3.6. Notice that the term *secondary instability* does not refer to the jargon commonly used in classical stability analysis. This term is only used here to differentiate the leading edge instability from the Kelvin-Helmholtz one. Particularly, we notice from Fig. 3.4 that the primary instabilities reach further upstream for the $M_\infty = 0.1$ case. On the other hand, for $M_\infty = 0.4$, a wider favorable pressure gradient region along the leading edge causes the formation of secondary instabilities to be shifted downstream over the airfoil suction side and slightly delayed in time (see first two columns of Fig. 3.5). This is illustrated in Fig. 3.8, which shows the instantaneous covariant derivative of pressure along the airfoil. The variable $\xi = \xi(x, y)$ is the curvilinear coordinate of the O-mesh topology, which goes along the airfoil profile, and $d\xi/|d\xi|$ is introduced to remove the influence of the mesh orientation of the covariant derivative. The basis of the curvilinear system is also normalized to yield a scale in physical units. As discussed in literature (Li *et. al* (2019)), compressibility has a stabilizing effect that delays the laminar to turbulence transition in free shear flows. Here, the mechanism appears to be similar although the plunging motion together with the surface presence lead to a more complex flow.

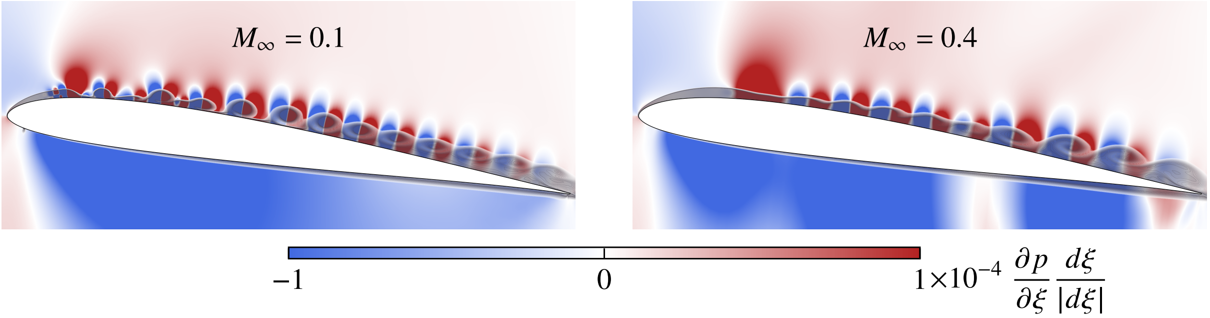

Figure 3.8: Pressure gradient contours (blue and red colors) in the streamwise ξ direction and contours of entropy (transparent shading) for $M_\infty = 0.1$ (left) and $M_\infty = 0.4$ (right) at $t = 4.25$.

Given the importance of the pressure gradient on the dynamic stall onset, we display the pressure gradient history along the ξ direction over the airfoil suction side in Fig. 3.9. The saturation level is kept high to call attention to the features marked in the figure. Von Kármán vortices are shed from the airfoil trailing edge before the primary instability stage. These vortices induce flow fluctuations that are scattered by the trailing edge generating acoustic waves which propagate upstream. These waves are perceived as the white ribbons in marker #3. The traces of the acoustic waves start at $\phi \approx 60°$ and can be observed up to $\phi \approx 120°$. The black arrows are tangent to their traces and it is possible to conclude that, for the $M_\infty = 0.4$ flow, the acoustic waves propagate upstream at a lower speed than for $M_\infty = 0.1$ due to the Doppler effect. Moreover, the larger thicknesses of the ribbons reflect the fact that the frequency at which the acoustic waves are generated is lower for $M_\infty = 0.4$. The arrows also show the path taken by a particular wave that coincides with the inception of the Kelvin-Helmholtz instabilities for each flow (the latter being represented by marker #2). The black circles in both subplots are positioned in the same spatio-temporal coordinates, emphasizing that the mechanism that creates the primary instability originates from the trailing edge at the same time for the two compressible regimes. However, since the upstream propagation speed of the acoustic wave is lower for the higher Mach number, the perturbation takes longer to reach $x/c = 0.65$, where the Kelvin-Helmholtz instability starts. This chord location appears to be the same for both flows and it is represented by the vertical dashed line in each subplot. In the region of marker #2, we observe the Kelvin-Helmholtz instabilities that, analogously to what happens with the acoustic waves, display a lower frequency for $M_\infty = 0.4$.

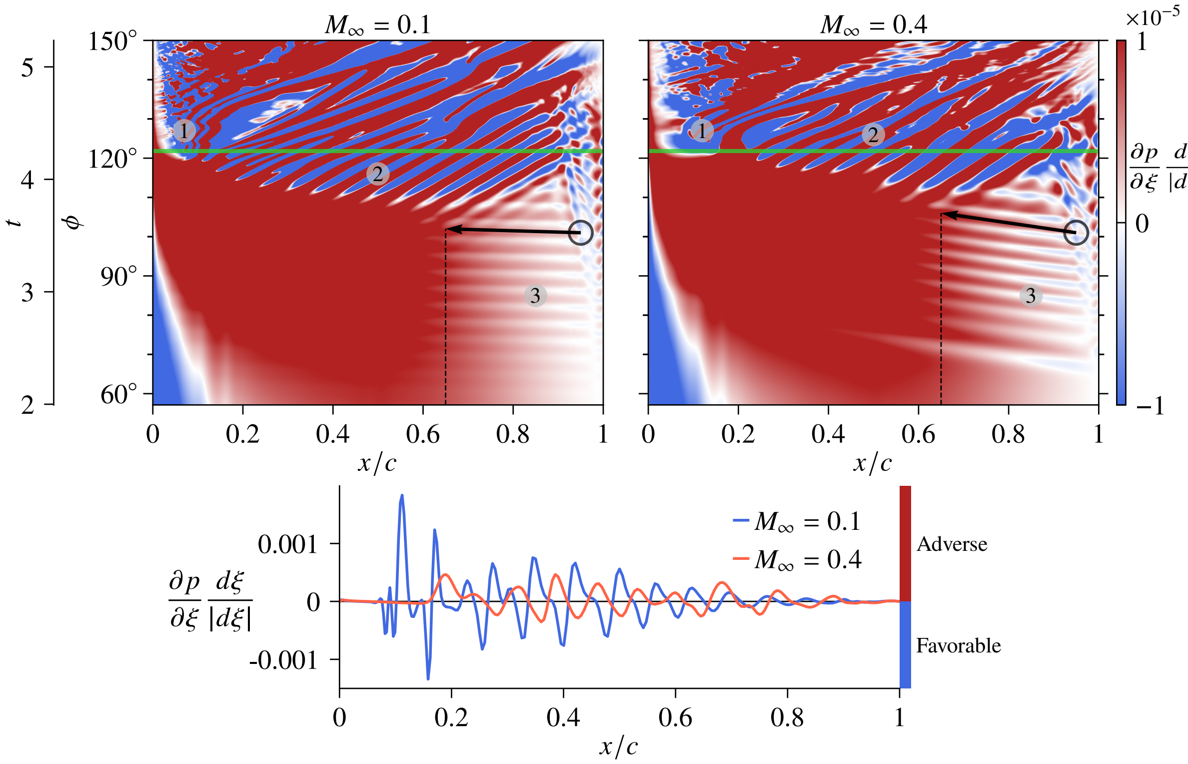

Figure 3.9: History of pressure gradient in ξ direction over the airfoil suction side for $M_\infty = 0.1$ (left) and $M_\infty = 0.4$ (right). The graph below shows the pressure gradients computed along the horizontal green line, which corresponds to $t = 4.25$.

Shih *et. al* (1995) pointed out that, although a flow reversal extends from the trailing edge over the airfoil suction side, there was insufficient time for this flow to reach the leading edge region. Therefore, they postulated that the flow reversal near the leading edge and the eventual initiation of the unsteady separation were essentially local phenomena. The trailing edge, in turn, was considered responsible for influencing the separation indirectly, through the increase of global circulation around the airfoil by shedding counter-rotating vorticity into the wake. In our compressible simulations, the importance of the trailing edge lies in what appears to be the acoustic triggering of Kelvin-Helmholtz instabilities, but it is unclear whether the trailing edge is of secondary importance to the onset of the DSV. The Kelvin-Helmholtz instabilities occur due to shear but our results suggest that the trailing-edge acoustics might act as an initial disturbance that triggers the formation of such instabilities. Moreover, at marker #1 in Fig. 3.9, we see that the onset of the DSV occurs at nearly the same time for the two regimes, as do the acoustic waves that possibly trigger the primary instability. Since these latter propagate at different speeds, this means that the acoustic disturbance does not directly influence the dynamic stall onset. On the other hand, separation only occurs when the primary instability reaches the leading edge region and the trailing edge seems to be important in the generation of this primary instability. Other studies (Benton and Visbal (2020)) have shown that the turbulent separation from the trailing edge can play an important role in the dynamic stall onset depending on the flow configuration. However, such trailing edge separation is not present in our results.

In order to better assess the differences in pressure gradient between the two flows, we plot the values of the ξ pressure gradient component over the horizontal green line displayed in Fig. 3.9, which corresponds to $t = 4.25$. The time instant is the same as that shown in Fig. 3.8, which displayed a wider region of favorable pressure gradient along the leading edge for $M_\infty = 0.4$. This more extensive region of favorable pressure gradient delays the formation of secondary instabilities in the higher Mach number case. From the figure, we can see that the adverse pressure gradient region (positive values) is shifted downstream from the leading edge at higher Mach number. We also notice that the magnitudes of the pressure gradient fluctuations are higher for the $M_\infty = 0.1$ case. In addition, high frequency oscillations and a strong peak appear close to the leading edge for $M_\infty = 0.1$. These are related to the beginning of the destabilization of the local vorticity distribution described by the van Dommelen and Shen model. Finally, this plot provides another interesting observation about the wavelengths of the Kelvin-Helmholtz instabilities: for the higher Mach number case, longer wavelengths are observed near the trailing edge region (say $x/c > 0.6$) while shorter ones can be seen around the mid-chord. For the lower Mach number flow, on the other hand, the wavelengths appear to be more uniform. Since our results are presented in terms of spanwise-averaged quantities, this fact possibly indicates a higher three-dimensionality of the flow structures close to the trailing edge for $M_\infty = 0.4$.

In a recent work from Benton and Visbal (2020), simulations of a static NACA 0012 at 8° of angle of attack and $\mathrm{Re} = 10^6$ showed the presence of a wider spectrum of three-dimensional (oblique) modes in the transition process at the leading edge as compressibility was increased. Based on their observations, we investigate the presence of three-dimensional disturbances in the flow for the current plunging airfoil. Results are shown in Fig 3.10 where iso-surfaces of q-criterion, $Q = 1/2\,(||\Omega||^2 - ||S||^2)$, colored by x-momentum are plotted over the airfoil suction side. The figure is presented for $t = 4.4$, which corresponds to a moment before the ejection of the first leading edge vortex (see third column of Fig. 3.6). Results show that the higher Mach number flow is more three-dimensional along the entire airfoil suction side. Given the quicker breakup of spanwise coherence of Kelvin-Helmholtz instabilities for $M_\infty = 0.4$, it could be that non-normality plays an important role in this case. Even the leading edge vortices related to the secondary instability mechanism display spanwise modes at this higher Mach number. On the other hand, the rolls of the $M_\infty = 0.1$ flow are mostly two-dimensional, except close to the trailing edge where transition sets in.

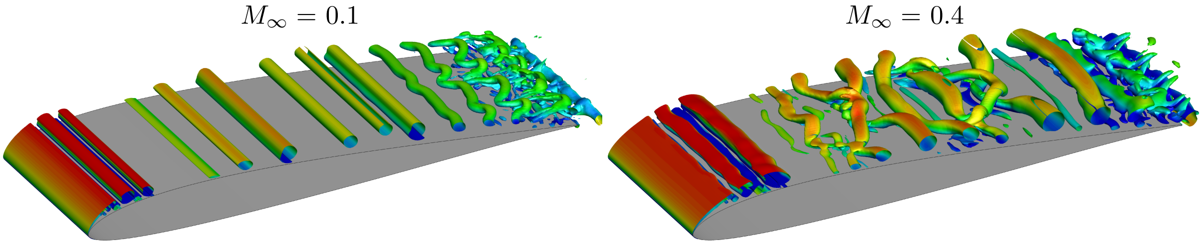

Figure 3.10: Iso-surfaces of q-criterion colored by x-momentum for $M_\infty = 0.1$ (left) and $M_\infty = 0.4$ (right) computed at $t = 4.4$.

Since vorticity is an important quantity in the onset and development of dynamic stall, an analysis of its evolution was also conducted to better understand how its dynamics and related flow structures are affected by compressibility. However, we decided to leave this discussion for the Appendix B in order to convey a clear message to the reader along the main text. The key takeaway from this analysis is that the baroclinic torque present in the vorticity transport equation acts as a stabilizing term as it opposes the dilatation one.

3.3 Analysis of empirical criteria for dynamic stall onset

The temporal evolution of the LESP for the periodic airfoil motion is shown on the left hand side of Fig. 3.11 for the two Mach numbers investigated. Relevant values of the phase angle ϕ are marked in the figure and the green and purple dots are the LESP thresholds, plotted along with their respective coordinates $(t,\, A_0)$. The green dots represent the first local maxima found in A_0 while the purple dots show the global maximum. According to the previous references, the global maximum should indicate the instant of the DSV onset.

However, we find here that the first local maximum provides a better estimate for the onset. Deparday and Mulleners (2019) show that after the onset of the DSV, the LESP is susceptible to fluctuations from the separated flow. Moreover, the secondary instabilities develop downstream 10% of the chord in the present flows. These characteristics could impact on the calculation of the LESP, since they may lead to new maximum values. Hence, the green dots will be used to provide the time instant of dynamic stall onset.

Comparing the blue and red lines from Fig. 3.11, which correspond to the values of A_0 for Mach numbers $M_\infty = 0.1$ and $M_\infty = 0.4$, respectively, we notice that the maximum suction is reduced as compressibility increases. This is a consequence of the weaker low pressure core formed close to the leading edge during the onset of dynamic stall, as shown in Fig. 3.2, and which directly influences the magnitude of the suction vector. Despite this observation, the dynamic stall onset occurs almost at the same time for both Mach numbers.

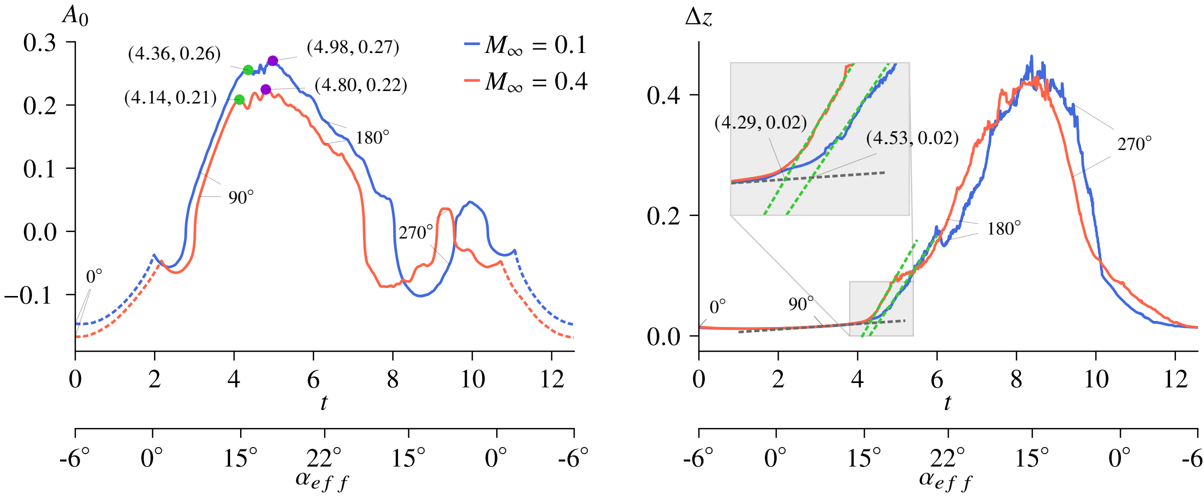

Figure 3.11: LESP and chord normal shear layer height for the airfoil in periodic motion at $M_\infty = 0.1$ and $M_\infty = 0.4$.

The temporal evolution of Δz for the two Mach number flows is shown in the right hand side of Fig. 3.11. From this figure, we see that during the lifetime of the dynamic stall vortex the shear layer height exhibits a high-frequency oscillatory behavior. This is a consequence of locally non-convex topological spaces formed when the flow is highly separated, causing the normal lines to have multiple intersections. This noise, however, does not degrade the capability of the method in finding the critical shear layer height since it is obtained by the intersection of two linear fits. According to Deparday and Mulleners (2019), these fits are comprised of the primary instability stage displayed by the dark gray line in Fig. 3.11, and the vortex formation stage represented by the first slope crossing this line. To draw the linear fits, a time window ranging from $3 \leq t \leq 4$ is used for the dark gray line, while for the vortex formation stage, the windows $4.5 \leq t \leq 6$ and $4.5 \leq t \leq 5$ are used for $M_\infty = 0.1$ and 0.4, respectively. For our simulations, the instant of formation of the DSV is marked by the intersection of the green with the gray dashed lines shown in the right plot of Fig. 3.11.

The threshold value based on the shear layer height of $\Delta z \approx 0.02$ remains the same for both Mach numbers. According to Deparday and Mulleners (2019), this critical value of Δz is invariant with respect to the kinematics. For the present periodical motion, in the absence of shock waves, we find that it is also invariant to the freestream Mach number. Further analysis should be conducted to verify if shock-induced separation would alter this threshold. Figure 3.11 indicates that, at the time instant shown in the abscissa of the first local maximum value of the LESP, a reasonable match is obtained with that computed by the critical shear layer height. However, when the global maximum value of the LESP is used, it indicates a more advanced stage characterized by the roll up of the shear layer into a large scale DSV as the onset point. Despite the small time lapse between results from the two different methods, both answers are reasonable and consistent with the skin friction maps of Fig. 3.3.

At this point, it is important to mention that to the present date there is no consistent definition of "stall onset" in the literature. For example, McCroskey (1981) defines it as the regime where maximum lift is produced. Mulleners and Raffel (2012), on the other hand, consider the point when the DSV detaches from the airfoil surface. Here, we do not infer a precise moment to the stall onset, but instead, consider a range of possible values starting from the time that the secondary instabilities initiate near the leading edge to that when the DSV detaches. Some studies (see Narsipur *et. al* (2020) and Deparday and Mulleners (2019)) reported that the LESP reaches its critical value well after the onset of instabilities near the leading edge. From the perspective of an effective control strategy, it is important to predict the stall onset before the DSV formation (Chandrasekhara, 2007). Overall, our results for LESP and Δz criteria agree reasonably well with the features seen in Figs. 3.5 and 3.6 (where the secondary instabilities are shown), in the sense that the critical values lie inside or close to this time interval. With increasing Mach number, however, both criteria indicate that the onset occurs earlier in time. This is consistent with the observations from Chandrasekhara and Carr (1990), who reported that increasing Mach number makes the DSV to form at a lower effective angle of attack and further downstream the leading edge. However, our simulations may not share this trend depending on how one defines the stall onset. By the inspection of either Fig. 3.5 or 3.6, it is possible to see that the instabilities appear sooner for the Mach 0.1 case, but the detachment of the leading-edge vortex comes after that for Mach 0.4. Hence, it is possible to conclude that both criteria are more closely related to the definition of stall onset as being the time when the DSV detaches from the airfoil surface, what could potentially be detrimental to the effectiveness of dynamic stall control.

3.4 Modal Analysis

Modal decomposition is now performed using the flow snapshots to identify the relevant flow dynamics related to stall onset in terms of low-rank features. As noted earlier, several different types of such decompositions exist, each with its own benefits and shortcomings. Typically, these approaches assemble snapshots in time and extract modes and corresponding eigenvalues, whose interpretation depends on the underlying theory. The benefits of applying modal decomposition in general, and DMD in particular, to examine dynamic stall may be found in Dunne *et. al* (2016); Mohan *et. al* (2016) and Ramos (2019). For DMD, the modes and corresponding eigenvalues obtained in the manner of § 2.3.1 and 2.3.2 represent a decomposition into coherent structures, each associated with a magnitude, growth or decay rate and characterized by a specific frequency.

The transient nature of the current problem, where some phenomena such as stall onset are relatively rapid and dominant in a short time range of the imposed period, motivates the need for special care in the interpretation of the results. Indeed, as shown in this section, application of the original DMD as in the cited references is problematic for the current dataset; this motivates the adoption of the relatively more recent multi-resolution variant (mrDMD), whose properties are more suited to datasets where the condition of a zero-mean second-order stochastic process is not appropriate.

In the standard DMD algorithm, the resulting modes can be ranked by either mode frequency or amplitude. Here, we chose to rank the modes in decreasing order by their amplitudes b_j from Eq. 2.10, with j being the index of the mode. A collection of 1024 snapshots of pressure coefficient is used to build the matrices $\mathbf{X}$ and $\mathbf{X}'$ (details of the algorithm are provided in § 2.3.1) within a time period of π/k, corresponding to a full cycle of the airfoil motion, where $k \triangleq \pi f c/U_\infty = 0.25$ is the reduced-frequency. Analogously to the observation of Dunne *et. al* (2016) and Mohan *et. al* (2016), when ranked by their amplitudes, the first modes exhibit frequencies that may be associated with the harmonics of the imposed motion. Here, we leave the discussion of these harmonics to the §3.4.1 because, despite giving a global perspective about the effects of increasing compressibility on dynamic stall, the harmonics by themselves do not elucidate the underlying physics associated to the dynamic stall onset. To fill this gap, we search for modes which emphasize the contribution to the dynamics near the leading edge.

Some selected modes are presented in Fig. 3.12 together with their respective frequencies. The modes are arranged so that similar events can be compared for the two Mach numbers. Here, we stress that the results obtained from the classical DMD approach provide no guarantee that similar dynamical mechanisms are being compared. Indeed, there is no *a priori* assumption that similar mechanisms should exist at the two

Mach numbers. Thus, by similar events, we mean that the spatial distributions of the modes are comparable. If more than one mode has a similar spatial distribution, we select the one with the closest frequency. Therefore, the rationale behind the selection of the DMD modes is the presence of a spatial distribution that could be associated with the DSV onset. Hence, after obtaining the DMD modes, we selected those whose spatial distribution had a clear relationship with the primary or secondary instability stages. Note that the growth rates of the modes are not presented because they are not representative of a linear stability analysis in this case, and saturation yields eigenvalues close to the unit circle.

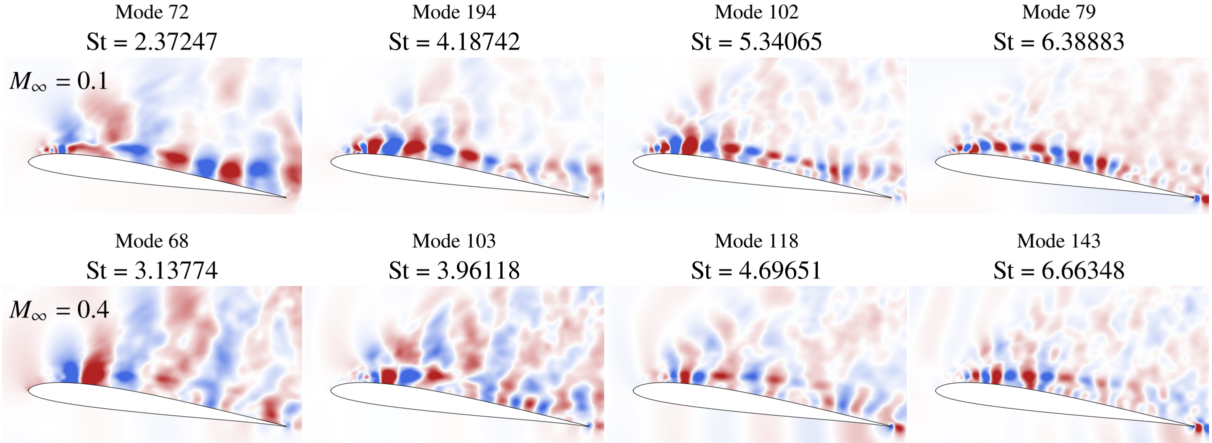

Figure 3.12: DMD modes for $M_\infty = 0.1$ (top) and $M_\infty = 0.4$ (bottom) for the periodic motion.

The standard DMD algorithm essentially combines data from all snapshots; for example, as shown in Fig. 3.12, all modes containing coherent structure information near the leading edge also include the influence of the flow from post-stall stages. Colored regions away from the airfoil surface in all subplots are a remnant indication of the passage of the DSV. They arise from the fact that the extracted modes exist throughout the entire temporal window analyzed, which impairs the capacity of the algorithm to highlight events that may be dominant only in a finite time window of the cycle. The signature of such events is effectively spread out over the cycle and complicates the interpretation of the DMD modes. This issue is also related to the inefficacy of SVD based approaches to extract low-rank dynamics from data with translational and rotational invariance, as discussed in the work from Kutz *et. al* (2016), where the mrDMD algorithm is proposed.

Despite these limitations, some useful observations can still be drawn from these modes. For instance, the intense structures close to the airfoil surface, especially around the leading edge region, are shifted slightly downstream for the $M_\infty = 0.4$ case. The results also suggest that the frequencies of the structures associated with dynamic stall onset between the two Mach number flows are similar and range from St $\sim$ 1 to 40. In Fig. 3.12, only a few modes are shown, so it does not cover all frequencies mentioned in that range. Moreover, these values are not precise as they are derived from a nonlinear collection of snapshots, and only provide a perception of the order of magnitude of the frequencies at play during the dynamic stall onset. The persistence of the flow structures and their corresponding frequencies across the compressible regimes investigated indicate a possible correlation of mode shapes from a parametric modal decomposition perspective, as reported by Coleman *et. al* (2019).

The limitations of the standard DMD are now lifted by applying the mrDMD algorithm proposed by Kutz *et. al* (2016). Using the same procedure as before and the binning technique of § 2.3.2, some of the most interesting modes are presented in Fig. 3.13. In the multi-resolution approach, the modes are no longer ranked by their amplitude so that, instead of showing the index of a given mode, it is more suitable to discuss the resolution level and the bin where it resides. For clarity, the levels and bins are converted into their equivalent time periods Δt and the modes are judiciously organized in the figure so that the same period of time is assimilated between the two different Mach number flows.

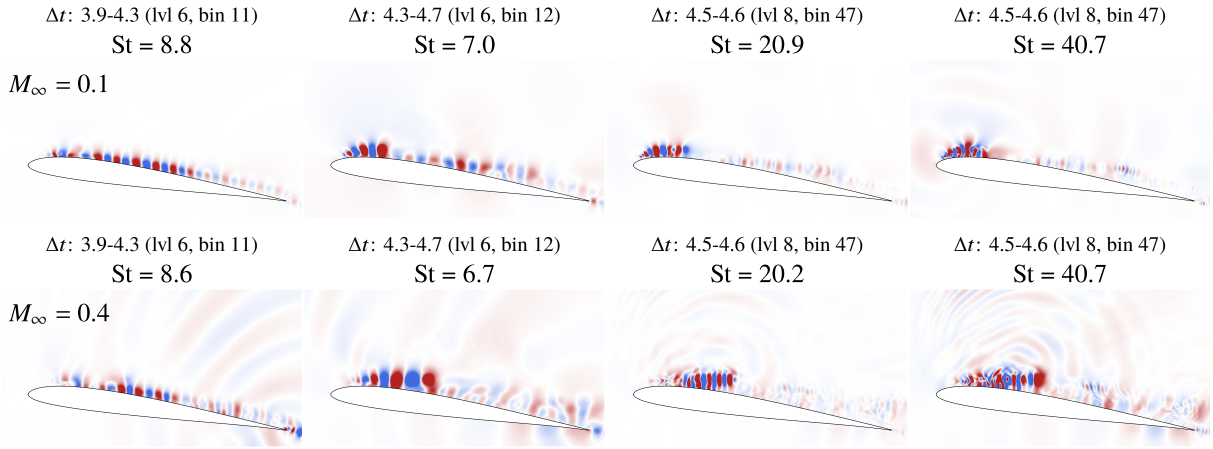

Figure 3.13: DMD modes obtained from the mrDMD algorithm for $M_\infty = 0.1$ (top) and $M_\infty = 0.4$ (bottom) for the periodic motion.

Comparing Figs. 3.12 and 3.13, it is evident that the multi-resolution variant has a better capability to deal with the transient nature of dynamic stall and is able to extract clean and physically interpretable modes. Starting from the leftmost column of Fig. 3.13, we observe the structures that represent the Kelvin-Helmholtz instability formed along the airfoil suction side. Note that the time period encompassed by this mode coincides with the time window when the instability develops, as shown in Fig. 3.4 and also the pressure gradient plot of Fig. 3.9. For the $M_\infty = 0.4$ case, acoustic waves are also seen propagating from the trailing edge due to a scattering mechanism, but these are not visible for the $M_\infty = 0.1$ case since the acoustic waves have a lower amplitude for this flow. The spatial distribution of the modes is also different. While a quasi-continuous train of Kelvin-Helmholtz disturbances appears as a wavepacket at $M_\infty = 0.1$, the structures are more sparsely distributed for $M_\infty = 0.4$, being more concentrated at the mid-chord. This is consistent with the observation of high frequency oscillations in the skin friction and pressure gradient maps of Figs. 3.3 and 3.9, respectively. It is also interesting to note that the frequencies between the two compressible cases are much alike, and this holds for all subplots.

The modes depicted in the subsequent columns are associated with the growth of the shear layer instabilities close to the leading edge and the separation process that leads to the formation of the DSV. In the second column, the modes represent the advection of vortical structures formed in the leading edge shear layer instability, which coalesce afterwards to form the DSV. The frequencies represented in this second column (St ≈ 7) are close to that obtained by Ramos *et. al* (2019) during their attempt to suppress the DSV formation with a zero-net flux actuator. Finally, the last two columns refer to the same time period and mark the separation process described earlier in Figs. 3.5 and 3.6, where nonlinear mechanisms govern the evolution of the flow. As indicated in Fig. 3.13, the frequencies increase substantially at this stage, independently of the Mach number. While the structures observed in the last two columns are more organized and compact for $M_\infty = 0.1$, those appearing in the $M_\infty = 0.4$ flow are composed of a wider range of spatial scales. This observation may reflect the higher three-dimensionality of the $M_\infty = 0.4$ flow, as shown in Fig. 3.10. As discussed before, the structures are also formed downstream for the $M_\infty = 0.4$ case and extend over a larger portion of the airfoil chord. For these DMD modes, one can also see that acoustic waves are generated by the hydrodynamic fluctuations near the leading edge. These waves have higher wavenumbers for the $M_\infty = 0.4$ flow and may contribute to the earlier breakdown into three-dimensional structures.

3.4.1 Harmonics of the periodic motion

In this section, we demonstrate that, when ranked by their amplitudes, the first modes exhibit frequencies that may be associated with the harmonics of the imposed motion. Similar observations were also made by Dunne *et. al* (2016) and Mohan *et. al* (2016). Within a time period of π/k, corresponding to a full cycle of the airfoil motion, where $k \triangleq \pi f c/U_\infty = 0.25$ is the reduced-frequency, we define the Strouhal number based on the nondimensional airfoil chord ($c = 1$) as St $\triangleq fc/U_\infty = k/\pi \approx 0.07958$. This nondimensional frequency of the plunging motion matches that of the dominant (first) dynamic mode, which is plotted in Fig. 3.14 along with the extracted frequencies from DMD. In this figure, the modes corresponding to the harmonics of St $= 0.07958$ are also included for both Mach numbers and the saturation levels are kept the same for all subplots, ranging from -0.004 to 0.004. The DMD is computed here using snapshots of pressure coefficient

Comparing the different Mach number solutions in Fig. 3.14, a striking resemblance of the dominant dynamic mode and its harmonics is noted. This occurs because these

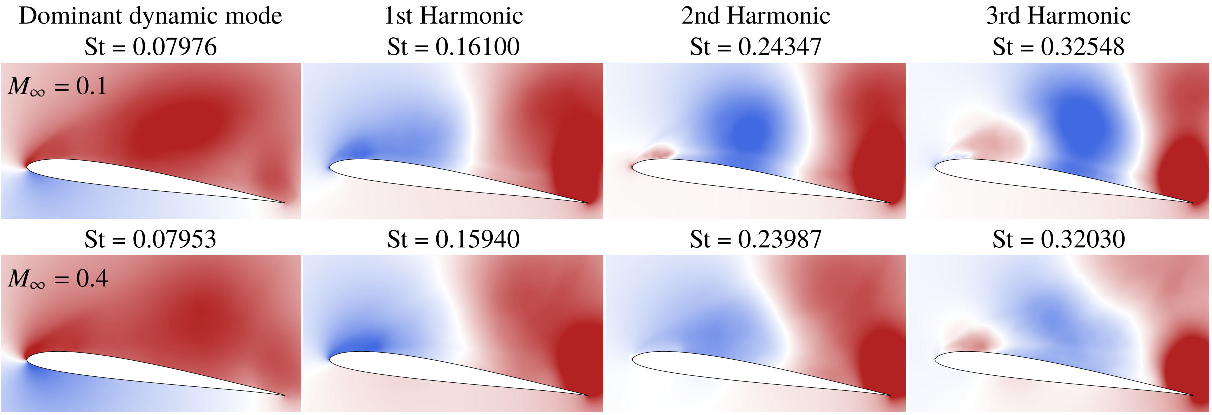

Figure 3.14: DMD dominant mode and sub-harmonics for $M_\infty = 0.1$ (top) and $M_\infty = 0.4$ (bottom) for the periodic motion.

modes are related to the airfoil kinematics, which is the same for both Mach numbers investigated. Nevertheless, some characteristics of the higher Mach number flow are still visible in these modes, such as the weaker DSV strength. For instance, the harmonics of the $M_\infty = 0.4$ flow have a slightly smaller area in blue color, and the levels in these regions are reduced when compared to the $M_\infty = 0.1$ case. Inspection of the 3rd harmonic for both Mach numbers shows a weaker presence of the leading edge red structure for $M_\infty = 0.4$; this indicates that the leading edge dynamics occurs with a different phase compared to that of the $M_\infty = 0.1$ case. Overall, at higher harmonics, the disparities caused by the phase lag between the two flows become more accentuated. The cause of this phase variation is the different gestation period and residency time of the DSV over the airfoil between the two Mach number flows.

4 Pitch-plunge equivalence

In this section, LES results are presented for an SD7003 airfoil under deep dynamic stall for both pitch and plunge ramp motions. All simulations are performed at Reynolds number $\mathrm{Re} = 6 \times 10^4$. It is worth mentioning that, in this work, we employ the same numerical method and grid used by Ramos *et. al* (2019) for a periodically plunging airfoil at $M_\infty = 0.1$, whose results compare well with those from Visbal (2011), both in terms of local flow structures and integrated loads. Here, the airfoil kinematics is changed to investigate the pitch-plunge equivalence problem.

An O-type grid is used in the simulations and contains $480 \times 351 \times 32$ (≈ 16 million) points in the streamwise, wall-normal and spanwise directions, respectively. To check whether this grid is still valid for our cases, a refined grid of size $576 \times 444 \times 120$ (≈ 31 million points) was designed to have 25 to 40% improvement in resolution on the suction side, depending on the direction, after a localized distribution of points. Then, two additional simulations (one for pitch and one for plunge motions) at $\Omega^+ = 0.10$ and $M_\infty = 0.1$ are performed using this refined computational grid. Similar conclusions are obtained between the two grids and, hence, results will be shown only for the smaller one. The discussion about the refined cases are presented in §4.5.

The airfoil span length is set as $s = 0.1c$, where c is the airfoil chord, based on studies reported in the literature (Visbal, 2011; Visbal and Garmann, 2018). These previous investigations show that a relatively small span can properly capture the flow features associated with the onset and evolution of the DSV. An extensive literature (see Visbal (2011); Visbal and Garmann (2018); Benton and Visbal (2019b, 2020) for instance) provides compelling evidence that this spanwise extension is sufficient to accurately capture the aerodynamic loadings and the relevant dynamics associated with the dynamic stall. To certify that the $s/c = 0.1$ span is sufficient to accurately represent the current dynamic stall problems, we performed an additional simulation of a pitching airfoil at $\Omega^+ = 0.10$ and $M_\infty = 0.1$ with $s/c = 0.4$. These results are also shown in §4.5.

4.1 Apparent Camber Effect

As a way of alleviating the lack of a more rigorous treatment on the definition of the equivalence, we use the concept of virtual (apparent) camber. Accordingly, quasi-steady thin-airfoil theory establishes that during pitch-up maneuvers, the apparent camber induced by the variable angle of attack along the chord produces higher C_l and lower C_m. Based on this fact, Visbal and Garmann (2022) could successfully reconcile lift and moment coefficients by subtracting the rotation-induced apparent camber contributions ΔC_l and ΔC_m present in the pitching case. In the present work, this correction is experimented for ramp-type maneuvers. For brevity, we only show the final expressions in what follows and refer the reader to Visbal and Garmann (2022) for a detailed development. According to the previous reference, the ΔC_l and ΔC_m terms are given by:

$$\Delta C_l = -\left(\frac{\mathrm{d}C_l}{\mathrm{d}\alpha_{eff}}\right)_{\text{static}} \left(x_p - \frac{3}{4}\right) \Omega^+ \cos\left(\alpha_{eff}\right) \tag{4.1}$$

and

$$\Delta C_m = -\frac{\pi}{8}\Omega^+ \cos\left(\alpha_{eff}\right) \ , \tag{4.2}$$

where x_p is the pivot location ($x_p = 1/4$ in our simulations). The term $(\mathrm{d}C_l/\mathrm{d}\alpha_{eff})_{\text{static}}$ is the airfoil static lift slope, obtained through line fitting over $10 \leq \alpha_{eff} \leq 17$ in the present simulations. This angle range is chosen due to the quasi-linear behavior of $C_l \times \alpha_{eff}$ observed in the results.

In what follows, we begin our discussion presenting the pitch-plunge equivalence for constant-ramp motion. Two different rates of motion are analyzed in this work, $\Omega^+ = 0.05$ and 0.10. Based on the fact that the literature of pitch-plunge equivalence usually assumes incompressible flows, we set the freestream Mach number as $M_\infty = 0.1$ in a first analysis. This value guarantees that the compressibility effects will be minimum while allowing for feasible computations using the present compressible solver. Then, we assess the effects of compressibility on pitch-plunge equivalence by increasing the freestream Mach number to $M_\infty = 0.4$. Thereby, a series of 8 different simulation setups are investigated in this work.

4.2 Pitch-plunge equivalence for constant-ramp motions

As pitching and plunging motions are fundamentally different, it would be beneficial to establish an equivalent comparison between them to assess their role on dynamic stall. Most studies of pitch-plunge equivalence are available in the literature for periodic motions owing to the already existing large database of periodically pitching foils. However, periodicity introduces complications due to the different initial conditions imposed to the flow from cycle-to-cycle. Fortunately, airfoils in pitching ramp motion, which are commonly used for the study of dynamic stall (Lorber and Carta, 1988; Ol *et. al*, 2010; Yu *et. al*, 2018; Benton and Visbal, 2019b), are known to successfully suppress this difficulty. Motivated by this fact, in this session we define a ramp motion for plunging airfoils that can be directly compared to their pitching counterpart. A similar approach was carried out by Ol *et. al* (2009).

The term *ramp* used throughout the text refers to the fact that the effective angle of attack α_{eff} is continually increasing, for example, as in a pitch-up movement with a fixed angular velocity. In a plunging airfoil, however, the motion requires the descent velocity to continuously increase following a tangent-like curve to match the geometric angle of attack of the pitching maneuver. For that, the descent velocity must be specified as

$$\dot{h}(t) = -\tan(\Omega^{+}t)\left[1 - \exp(-at)\right], \tag{4.3}$$

where Ω^+ is the rate at which the effective angle of attack increases (say $\dot{\alpha}_{eff} = \Omega^+$), and a is a constant used for exponential smoothing set as $a = 9.2$ in the present calculations. The values of Ω^+ analyzed in this work are $\Omega^+ = 0.05$ and 0.10 and the parameters $\dot{h}$, Ω^+ and a are presented here nondimensionalized by the freestream velocity (instead of the speed of sound) to follow other studies available in the literature. The airfoil static angle of attack is kept as $\alpha_0 = 8°$.

Equation 4.3 deserves a special attention and we first neglect the exponential smoothing term to show how Ω^+ and the descent velocity $\dot{h}$ are interrelated. Considering α_0 as the static angle of attack, α_{eff} relates to $\dot{h}$ by the following expression

$$\alpha_{eff} \triangleq \alpha_0 + \arctan\left(-\dot{h}(t)\right) ,$$

which is also equal to $\alpha_{eff} = \alpha_0 + \Omega^+ t$ for a constant ramp motion. This condition implies that $\dot{h}(t) = -\tan(\Omega^+ t)$. Then, we add the exponential term on the descent velocity to smooth out the initial transient of motion and to make it more physically representative, taking us to Eq. 4.3. It is worth mentioning that there exist other ways to construct the angle-of-attack schedule. Eldredge *et. al* (2009), for example, use an alternative definition for the smoothing function. That said, the impact of this term on results will be shown in §4.4, but for what matters, we can say that the results are robust with respect to it.

It is interesting to note that Eq. 4.3 has singularities depending on the value of $\Omega^+ t$. Physically, it means that, at some point, for the effective angle of attack to continue increasing, the velocity would tend to infinity. This condition corresponds to a purely normal relative velocity of incidence and imposes that the simulation time must be bounded to $t < \pi/(2\Omega^+)$. Despite the temporal restriction, the dynamic stall can still be studied using the proposed ramp motion because the formation of the DSV takes place at short times for practical Ω^+ values.

In the pitching ramp motion, the angular rotation rate is prescribed by the following equation

$$\dot{\alpha}_{eff}(t) = \Omega^+[1 - \exp(-at)],$$

which can be directly integrated to give the instantaneous angle of attack,

$$\alpha_{eff}(t) = \alpha_0 + \Omega^+\{t + 1/a\,[\exp(-at) - 1]\}. \tag{4.4}$$

The values of Ω^+ and a in Eq. 4.4 are the same as those employed in the plunging motion of Eq. 4.3 so that the effective angle of attack in both cases increases at the same rate, allowing a direct comparison.

We begin the analysis for the ramp simulations with $\Omega^+ = 0.05$. Results are shown in Figs. 4.1 and 4.2 in terms of the aerodynamic loads and contours of pressure coefficient, respectively. The red dashed lines in Fig. 4.1 indicate the corrected lift and moment coefficients that take into account the rotation-induced apparent camber present in the pitching case (Visbal and Garmann, 2022), as discussed in §4.1. The immediate observation from Fig. 4.1 is the similarity of the pitching and plunging aerodynamic coefficients within the analyzed time window (see solid lines). Both lift and drag continue to increase until reaching $\alpha_{eff} \approx 22.5°$. At this point, a sudden drop occurs, indicating the detachment of the DSV. This drop is more pronounced for the pitch motion (red curve) while the trend is reversed for the moment coefficient. Soon after, a rapid recovery in lift and drag coefficients occurs for both motions. However, the recovery starts at an earlier angle of attack of $\alpha_{eff} \approx 25.0°$ for the plunging case. In this figure, it is possible to notice that the pitch-corrected solution has an even better agreement in terms of C_l and C_m for lower angles of attack, as expected from theory.

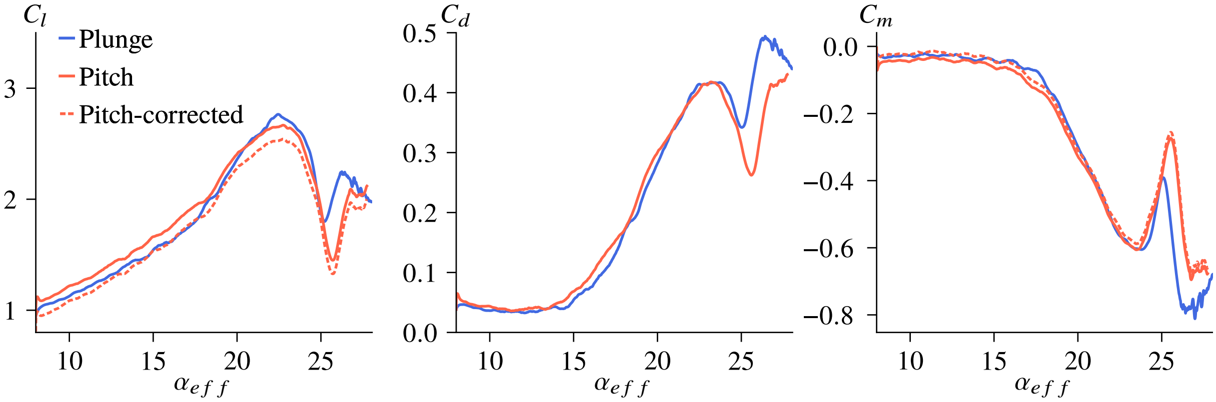

Figure 4.1: Pitch/plunge effects on lift, drag and moment coefficients for $M_\infty = 0.1$ and $\Omega^+ = 0.05$.

Figure 4.2 depicts the flowfields computed for the pitch and plunge cases labeled in Fig. 4.1 at specific effective angles of attack. This figure shows the pressure coefficient (in color) together with plots of an entropy measure (Visbal and Garmann, 2022; Miotto *et. al*, 2022) (in gray scale) defined as $(p/p_0)/(\rho/\rho_0)^\gamma - 1$. The values $p_0 = 1/\gamma$ and $\rho_0 = 1$ are reference values for nondimensional freestream pressure and density, respectively. This entropy measure gives a better visual representation of the separated flow since it indicates the regions where entropy is changing due to viscous effects. This figure provides a qualitative perspective of the flow and allows an interpretation of the evolution

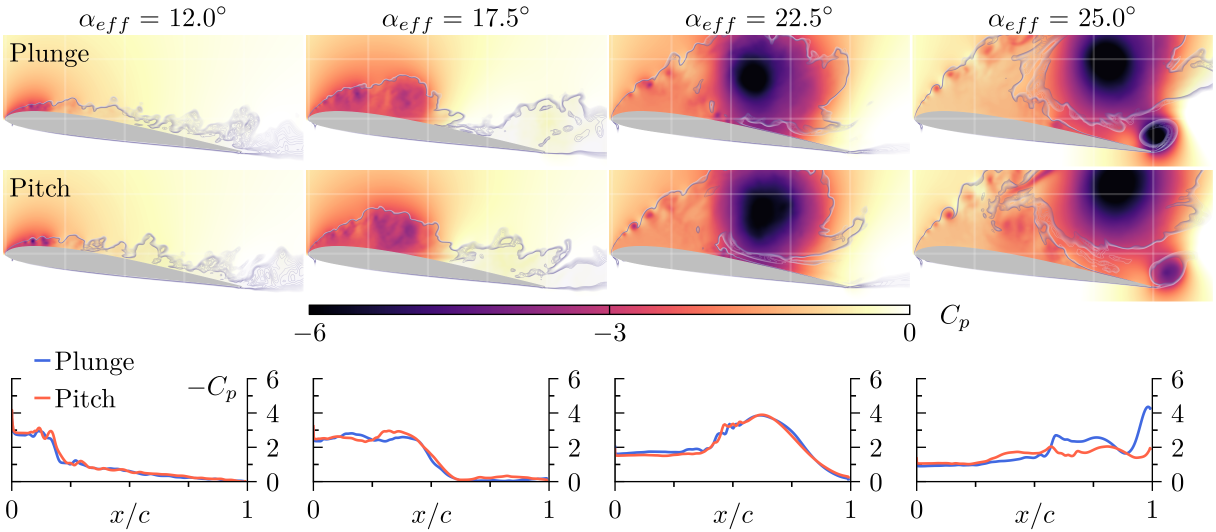

Figure 4.2: Pressure coefficient contours shaded by an entropy measure (superposed in gray scale) and instantaneous C_p distributions on the airfoil suction side at different time instants for $M_\infty = 0.1$ and $\Omega^+ = 0.05$.

of aerodynamic coefficients. While the C_p contours allow for visualization of the pressure variations due to the DSV and TEV, the superposed gray shade of entropy measure shows the flow separation. Faint white lines are plotted in the figures to allow a better comparison of the DSV and TEV positions for the different motions. Movies are submitted as supplemental material to provide a better comparison among all flow configurations studied in the present work. They can be found at `https://drive.google.com/drive/folders/10xs7t7MEJrdjJjD2A31Fu-UPpzCZxzCs?usp=sharing`. In one of the movies, results are compared based on the simulation time, while in the other, the effective angle of attack variation is kept the same. The cases discussed in Figs. 4.1 and 4.2 are referred to in the leftmost two columns of the top row in the movies.

Figure 4.2 also presents the C_p distributions along the airfoil suction side for the same effective angles of attack. As can be observed from these plots, the pressure distributions have excellent agreement for pitch and plunge, except when the TEV dynamics plays a major role. This can be seen in the rightmost plot for $\alpha_{eff} = 25.0°$ where, for the plunging motion, the TEV has a more pronounced suction peak at the trailing edge. For both cases, the TEVs form and move upstream along the airfoil suction side (we refer to the supplemental movie for a complete visualization of this effect) leading to the recovery in lift coefficient and the drag increase shown in Fig. 4.1. However, the stronger TEV (higher suction) from the plunging case leads to larger C_l and C_d values. Moreover, since the TEV advances upstream earlier for the plunging case, the lift recovery also occurs for lower effective angles of attack.

Results for $\Omega^+ = 0.10$ are shown in Figs. 4.3 and 4.4 (see also the rightmost two columns of the top row in the movies), where the aerodynamic coefficients are much alike up to $\alpha_{eff} \approx 25.0°$. Beyond this angle of attack, up to $\alpha_{eff} \approx 30.0°$, the lift coefficients continue to increase due to the transport of the DSV along the airfoil suction side. This shift of the maximum lift and drag to higher incidence angles with increasing rate is expected from the literature (Eldredge *et. al*, 2009; Granlund *et. al*, 2013). However, there is a notable difference between the coefficients for pitch and plunge ranging from 25.0° to 35.0°, which we will comment on shortly. The TEV, in turn, forms at $\alpha_{eff} \approx 35.0°$ as can be seen in the third column of Fig. 4.4, and at higher angles of attack, the trailing-edge dynamics becomes relevant. For this case, the TEV is still the main cause of the equivalence breakdown and we can use an analogous discussion as that presented for $\Omega^+ = 0.05$ to explain the loss of equivalence between pitch and plunge. As such, although including the correction for the pitch apparent-camber effect improves the agreement of lift and pitch moment coefficients for the rates $\Omega^+ = 0.05$ and $\Omega^+ = 0.10$, it is not sufficient to accommodate the dissimilar dynamics that occur after the TEV is formed. This means that while the LEV formation and its subsequent evolution is driven by the rate of change of the effective angle of attack, the entire dynamic stall phenomenon cannot be described in a purely geometric sense. This fact conflates with the conclusions from Ol *et. al* (2008) and McGowan *et. al* (2008) who questioned the validity of the definition of the effective angle of attack used to construct the airfoil motions after noticing a mismatch of the wake patterns.

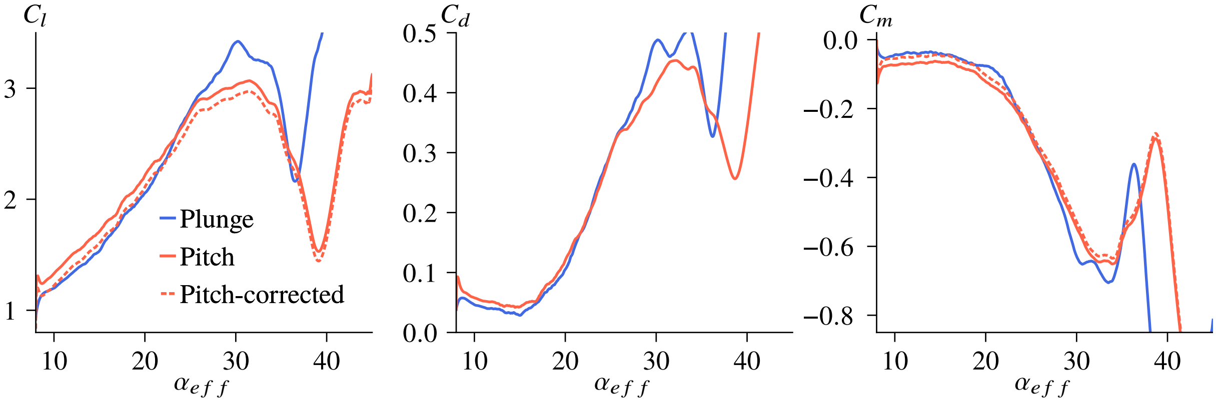

Figure 4.3: Pitch/plunge effects on lift, drag and moment coefficients for $M_\infty = 0.1$ and $\Omega^+ = 0.10$.

In Fig. 4.3, a difference is observed in the maximum values of C_l between pitch and plunge, specifically from $\alpha_{eff} = 25.0°$ to $35.0°$. The second column of Fig. 4.4 shows that, at $\alpha_{eff} = 30.0°$, the DSV is at the airfoil semi-chord and no significant pressure forces are observed at the trailing edge. Despite the similarities between the two flows, the instantaneous pressure distributions along the airfoil suction side show that the plunging case has a slightly stronger suction along the entire chord, which causes the discrepancy in maximum lift. The differences in the aerodynamic loads could be then justified by either a possible higher sensitivity of the airfoil response with respect to the higher rate Ω^+, or one could attribute this to the distinct inertial reaction during the beginning of the motion.

As shown in §4.4, we observed a noticeable sensitivity of the flow to smoothing at high

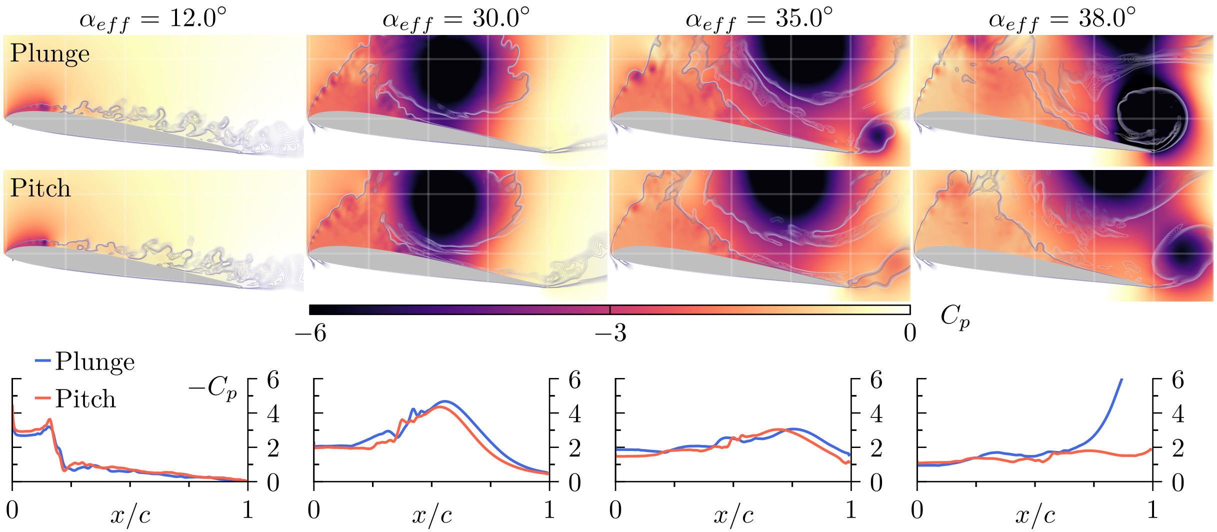

Figure 4.4: Pressure coefficient contours shaded by an entropy measure (superposed in gray scale) and instantaneous C_p distributions on the airfoil suction side at different time instants for $M_\infty = 0.1$ and $\Omega^+ = 0.10$.

incidence angles, contradicting some earlier observations from Gendrich *et. al* (1995). These authors concluded that the non-circulatory contributions should only influence the flow during the acceleration period and a relatively short time afterwards. On the other hand, Granlund *et. al* (2013) showed a noticeable sensitivity due to smoothing transients at higher angles of incidence and Mancini *et. al* (2015), in turn, demonstrate that higher acceleration of a surging airfoil impacts the force history for long convective times after its cessation, mostly due to the circulatory effect. An inspection of the C_p fields shows that, despite the nearly identical flow topologies between pitch and plunge, the locations of the low pressure cores of the LEVs are not precisely the same with time advancement, which should cause the bound circulation to vary between the two motions. A small shift in the LEV trajectory was also reported by Lee *et. al* (2022) and Mancini *et. al* (2015). However, the latter authors primarily attribute the variations of the airfoil response to a stronger LEV formed on fast airfoils. As the observations suggest, it is possible that the discrepancies in the aerodynamic loads between pitch and plunge from $\alpha_{eff} = 25.0°$ to 35.0° are linked to their initial accelerations.

To strengthen our observations about the equivalence, we draw maps of skin friction coefficient C_f over the airfoil suction side as a function of the effective angle of attack for both pitching and plunging motions in Fig. 4.5. These maps allow the visualization of the DSV and TEV traces along the airfoil chord. In this figure, the rows indicate a fixed rate Ω^+ while the type of motion is ordered columnwise. Additional axes carrying time labels are included to allow a better comparison between the different rates of motion Ω^+ and to identify the instants of the DSV onset. Note that since we double Ω^+, the time to reach the same effective angle of attack is expected to be halved. By comparing the columns, *i.e.* the types of motion, one can immediately observe the remarkable similarities between pitch and plunge prior to the formation of the TEV, represented by the red contours observed near the upper right corners in all figures. For $\Omega^+ = 0.10$ (bottom row), the earlier formation of the TEV for the plunge motion is evident.

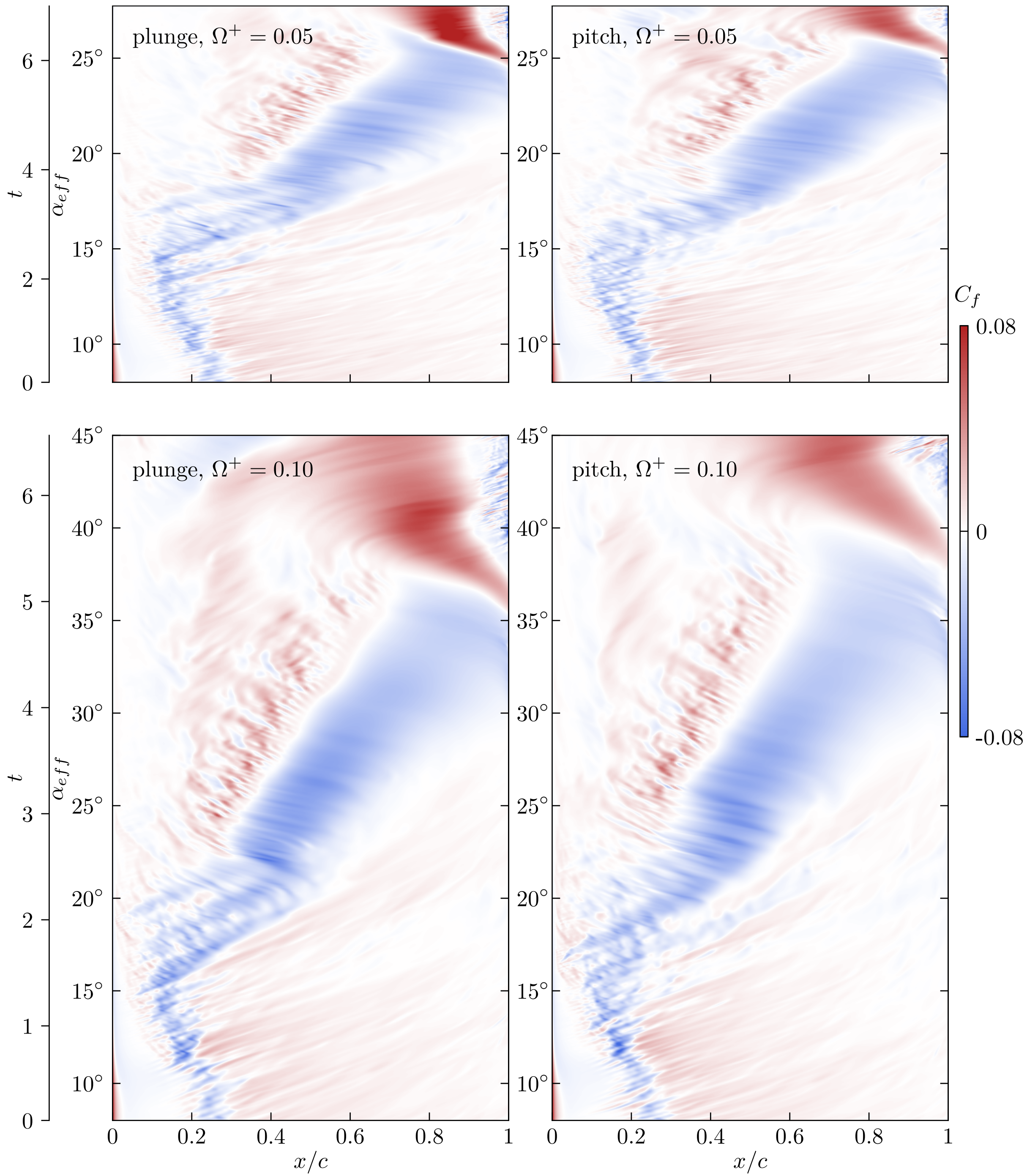

Figure 4.5: Comparison of skin friction coefficients of plunging (left) and pitching (right) ramp motions for $M_\infty = 0.1$, with $\Omega^+ = 0.05$ (top) and $\Omega^+ = 0.10$ (bottom).

From the maps of skin friction coefficient in Fig. 4.5, we observe the presence of a separation bubble from the moment when the airfoil starts the ramp motion (static angle of incidence at $\alpha_0 = 8°$). The bubbles start at $x/c \approx 0.25$ and move towards the leading edge with the increasing angle of attack until $x/c \approx 0.15$ and $\alpha_{eff} \approx 15°$. Then, they burst giving rise to the development of the LEV. Both the separation bubble and the signature of the DSV can be seen from the blue color contours in the skin friction coefficient distributions. The importance of a laminar separation bubble (LSB) on the dynamic stall onset has only recently become possible to evaluate. This difficulty comes from the small spatio-temporal scales associated with the LSB and from the high sensitivity of the bursting phenomenon to the state of the boundary-layer. In recent studies, Benton and Visbal (2018a,b) observed through the use of wall-resolved LES that the bubble bursting results in the formation of a small LEV that rolls up the separated flow to develop the DSV. In their work, the bubble bursting involved flow separation at the trailing edge that reaches the LSB near the leading edge to trigger the bursting. They attributed the variability in the location and timing of the DSV to the delay between the LSB formation and its interaction with the upstream propagation of the turbulent separation. In our simulations, such turbulent separation does not exist and the bubble bursting occurs due to a local process. The absence of the separated flow can be justified by the different airfoil configuration, Reynolds number and static angle of attack adopted in this study. Nonetheless, it is important to mention that this is not the first time that bubble bursting is described in terms of a local process (*i.e.*, without the turbulent separation). We will return to that discussion later in this chapter.

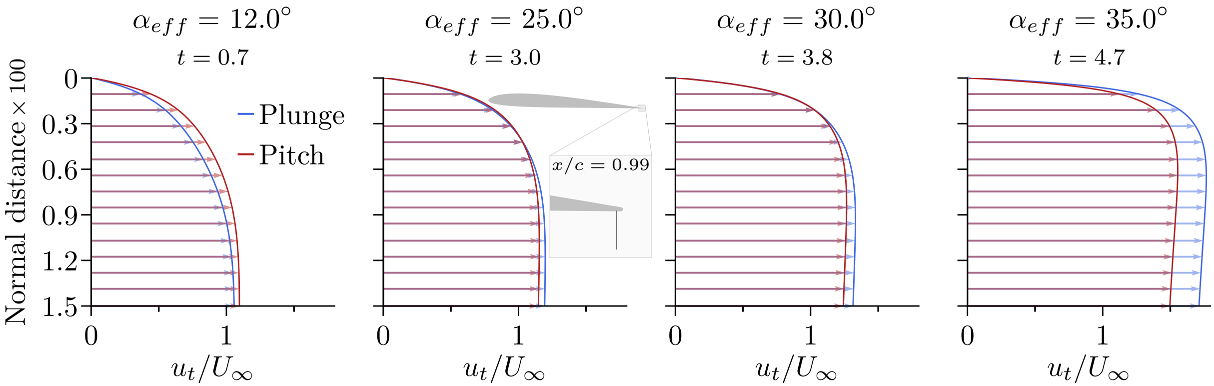

Figure 4.6: Tangencial velocity profiles measured at $x/c = 0.99$ on the airfoil pressure side for $M_\infty = 0.1$ and $\Omega^+ = 0.10$.

In summary, we show that the pitch-plunge equivalence holds for the cases of constant-ramp motion investigated until the formation of the TEV, at high effective incidence angles. A recent model from Xia and Mohseni (2017) establishes that the rate of circulation being shed from the trailing edge is impacted by the tangential velocities arriving on both sides of the trailing edge. In Fig. 4.6, we show an evolution of the tangential velocity profiles u_t near the trailing edge (at the 0.99 chord station on the pressure side) for pitch and plunge. The airfoil is also represented in this figure along with the line on which the velocity profiles are measured. This line is $0.0015c$ high. Note that the y-axis of the plots (wall-normal distance) is inverted to better match the line from which the data was extracted. Results show that the velocities are different before the formation of the TEV. The only case in which the TEV is already formed is that for the plunging case at $\alpha_{eff} = 35.0°$ in the last column. Therefore, the differences in TEVs between pitch and plunge could be associated to the different velocity profiles. In addition, the viscous extension of potential-flow unsteady aerodynamics from Taha and Rezaei (2019, 2022) also cast light on the probable reasons for the equivalence breakdown. Accordingly, their study demonstrate that the viscous contribution induces a significant phase shift in Theodorsen's lift response at high frequencies. In our case, this could be translated to a lag in the TEV formation between pitch and plunge due to different viscous responses. However, we emphasize that the trailing-edge systems of the present cases are also influenced by the LEVs and, therefore, should not be treated in isolation.

4.3 Earlier equivalence breakdown due to compressibility

In the previous section, we showed how the pitch-plunge equivalence holds for constant-ramp motions of the cases investigated. The aerodynamic coefficients and flow topologies are very similar between pitching and plunging motion, and noticeable differences would only occur at high loading conditions, especially when the TEV starts to form. In this section, we investigate the robustness of the pitch-plunge equivalence to compressibility variations. Even at the low/moderate Reynolds number considered in this work, compressibility effects should not be overlooked. For instance, many small wind turbines have high tip-speed ratios and some micro-air vehicles operate at high speeds, and this gives rise to situations where compressibility may influence performance. To this end, we consider a freestream Mach number $M_\infty = 0.4$ and replicate the same airfoil kinematics from before. This value is chosen to avoid the presence of shock waves since they would alter the underlying onset mechanisms.

Following the previous analyses, the aerodynamic coefficients for the pitch and plunge cases are presented followed by the contours of pressure coefficient and entropy measure. Results of simulations for $M_\infty = 0.4$ and $\Omega^+ = 0.05$ are presented in Figs. 4.7 and 4.8 (see also the first two columns of the bottom row in the movies). We also plot the aerodynamic coefficients for $M_\infty = 0.1$ in Fig. 4.7 and the C_p distributions over the airfoil suction side in Fig. 4.8 to establish a better comparison between the two compressible regimes. In both figures, results for $M_\infty = 0.1$ are shown by semi-transparent dashed lines. As the correction for apparent camber in pitching airfoils does not depend on any flow parameter, but only on the airfoil kinematics, this analysis has been omitted from the following results. With this, we draw the reader's attention only to the effects of compressibility. In this case, the pitch-plunge equivalence holds up to $\alpha_{eff} \approx 17°$, beyond which the curves vary drastically between pitch and plunge. When compared to the $M_\infty = 0.1$ cases, it corresponds to a drop of 5° of effective angle of attack over which the equivalence remains valid. From the figure, one can also see that the lift coefficients display a similar behavior for both $M_\infty = 0.1$ and 0.4 up to $\alpha_{eff} \approx 17°$. However, the higher compressibility results in an increased drag and magnitude of pitching moment coefficients that starts from the beginning of the motion.

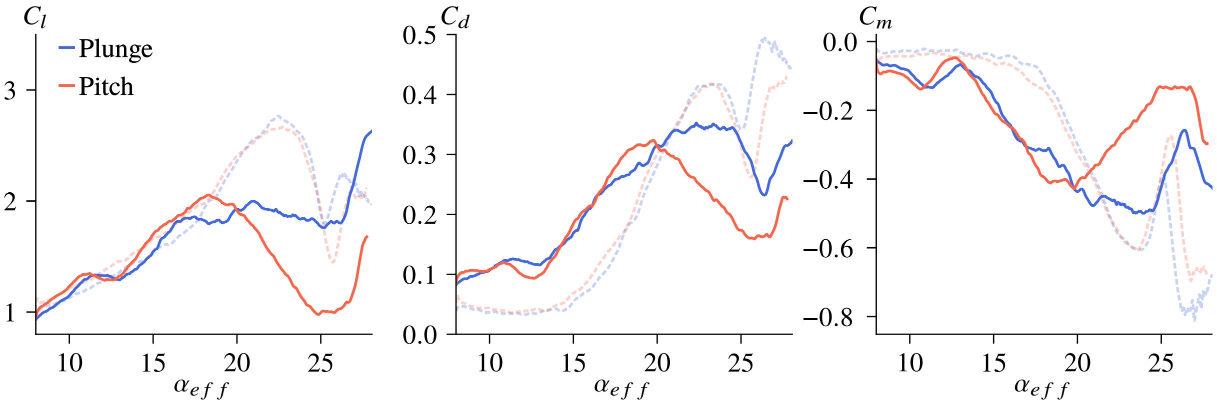

Figure 4.7: Pitch/plunge effects on lift, drag and moment coefficients for $M_\infty = 0.4$ and $\Omega^+ = 0.05$ (solid lines). Results for $M_\infty = 0.1$ are replicated by the dashed semi-transparent lines.

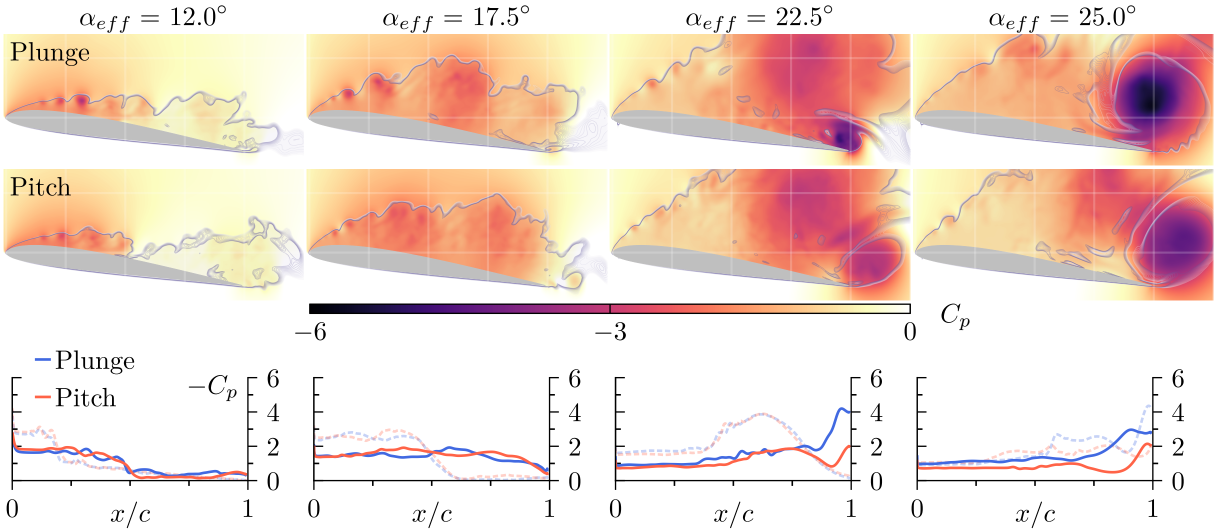

Figure 4.8: Pressure coefficient contours shaded by an entropy measure (superposed in gray scale) and instantaneous C_p distributions on the airfoil suction side at different time instants for $M_\infty = 0.4$ and $\Omega^+ = 0.05$.

In summary, the higher compressibility results in a scenario in which an overall increase of drag occurs. This contradicts the main trends observed by Miotto *et. al* (2022) for an SD7003 airfoil under periodic motion. In this previous reference, an increase in Mach number resulted in an improved aerodynamic performance in terms of drag. To address this antagonistic effect of compressibility, we compare the first two columns from Figs. 4.2 and 4.8. From these figures, we notice that the increase of drag forces occurs due to the higher separation and the more evenly distributed pressure forces over the airfoil chord at $M_\infty = 0.4$. In the second column of Fig. 4.2, we see the development of the LEV for the $M_\infty = 0.1$ cases. However, this more coherent flow structure seems to be absent in the $M_\infty = 0.4$ flows as depicted in Fig. 4.8. As a matter of fact, the large separation of the flow hinders the coalescence of the smaller vortical structures making the cohesive dynamic stall vortex to manifest posteriorly, as observed in the third column of the same figure.

From Fig. 4.8, it is possible to see that the DSV is more diffuse and weaker for the $M_\infty = 0.4$ flows. This is also manifested in the the plots of C_p distribution, from which it is easier to compare the two compressible regimes. The arrival of the DSV at the trailing edge region is sufficient to drastically change the aerodynamic loads between pitching and plunging. The disparate evolution of each type of motion is not an exclusive consequence of the pressure core itself, but of how it interacts with the trailing edge. For example, at $\alpha_{eff} = 22.5°$, a strong TEV forms over the airfoil in the plunging motion for $M_\infty = 0.4$. This vortex is weaker and positioned further downstream for the pitching case. In the last column of the figure, at $\alpha_{eff} = 25.0°$, we confirm that the TEV continues to grow further downstream of the airfoil for the pitching case compared to the plunging one. A similar trend, but less pronounced, is observed for the $M_\infty = 0.1$ cases as the large low pressure core of the DSV approaches the trailing edge. The reason for the earlier differences seen in the aerodynamic coefficients computed for plunge and pitch at $M_\infty = 0.4$ relates to this fact. By comparing Figs. 4.2 and 4.8, specially the third column, we also observe the smaller residency time of the DSV at $M_\infty = 0.4$, which is a phenomenon well established in the literature (Chandrasekhara and Carr, 1990; Corke and Thomas, 2015).

Results for $\Omega^+ = 0.10$ and $M_\infty = 0.4$ are shown in Figs. 4.9 and 4.10 (see also the rightmost two columns of the bottom row in the movies). For $M_\infty = 0.1$, we have seen that the aerodynamic coefficients and the flow topologies are much alike within the time period investigated, despite the gap in both C_l and C_d between the plunge and pitch solutions between $\alpha_{eff} = 25°$ and $35°$ (these results are replicated in Fig. 4.9 by the dashed semi-transparent lines). The lift for $M_\infty = 0.1$ also exhibited a small shift between pitch and plunge until reaching $\alpha_{eff} = 25°$. Similarly to the lower Mach case, one can see a shift between the red and blue curves of Fig. 4.9 along the interval from $8.0° < \alpha_{eff} < 17.0°$ in the lift coefficient, beyond which the lift curves show an almost perfect agreement. This shift, however, still persists in both drag and moment coefficients until $\alpha_{eff} \approx 30.0°$. From this point forward, the curves follow completely different trends.

Such different behavior, both in the sense of compressiblity effects and pitch-plunge equivalence, is better understood through the inspection of Fig. 4.10, from where we observe significant flow variations between the pitching and plunging motions. At $\alpha_{eff} = 12°$, the larger flow separation is responsible for the increased drag when compared to the results for $M_\infty = 0.1$ (see Fig. 4.4 for comparison). In the second column of Fig. 4.10, a strong low-pressure core can be identified in the pitching motion, but it appears more diffuse and slightly displaced downstream for the plunging case. This fact, however, does not seem to affect the equivalence observed for the lift coefficients. The equivalence breakdown only occurs at $\alpha_{eff} \approx 30.0°$ due to the formation of the TEV. From the third

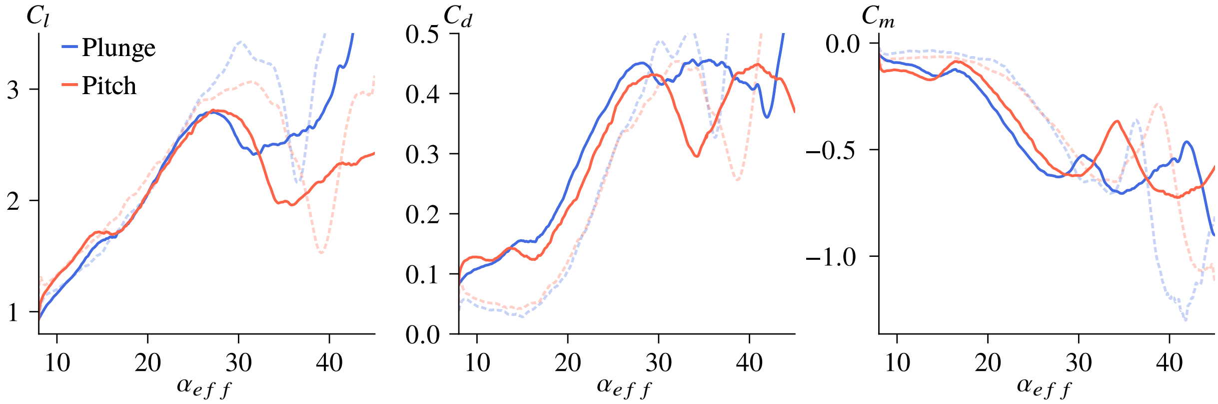

Figure 4.9: Pitch/plunge effects on lift, drag and moment coefficients for $M_\infty = 0.4$ and $\Omega^+ = 0.10$ (solid lines). Results for $M_\infty = 0.1$ are replicated by the dashed semi-transparent lines.

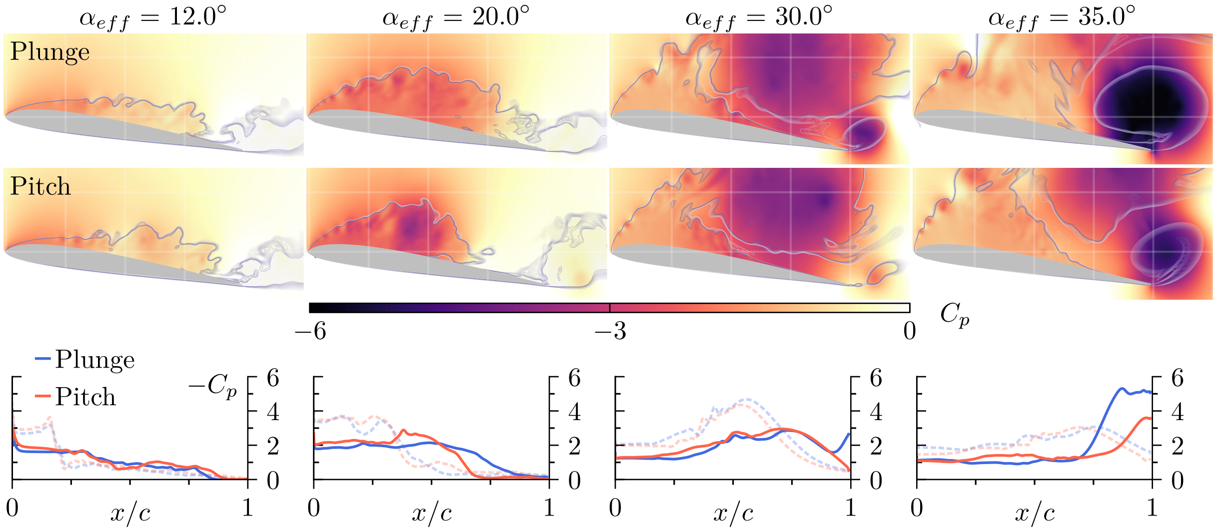

Figure 4.10: Pressure coefficient contours shaded by an entropy measure (superposed in gray scale) and instantaneous C_p distributions on the airfoil suction side at different time instants for $M_\infty = 0.4$ and $\Omega^+ = 0.10$.

column of Fig. 4.10, it is possible to see the earlier evolution of the TEV for the plunging motion in comparison with that for the pitching case. Finally, the noticeable increase in lift and drag coefficients revealed in Fig. 4.9 for $\alpha_{eff} > 38.0°$ occurs due to the inception of a second DSV, which is accompanied by a significant pressure drop on the entire airfoil suction side for the plunging motion. This phenomenon can be seen in the supplemental movie.

Similarly to what is done for the $M_\infty = 0.1$ cases, we plot maps of skin friction coefficient over the airfoil suction side in Fig. 4.11 for the $M_\infty = 0.4$ flows. In contrast to the $M_\infty = 0.1$ cases, the presence of the separation bubble is almost entirely masked from these maps for $M_\infty = 0.4$ as there is no concentrated zone of separation. Figure 4.12 shows the instantaneous entropy measure contours for $\alpha_{eff} = 8.0°$, immediately before the airfoil motion. In the bottom row, the same figure presents the spanwise and time-averaged entropy contours with the streamlines to better visualize the recirculation zones for the two compressible initial flow conditions. From these plots, it becomes evident that the recirculation region in the $M_\infty = 0.4$ flow is more pronounced, extending further downstream that for $M_\infty = 0.1$. For the higher Mach number flows, a very elongated recirculation region settles down until half-chord at the static angle of attack and, then, it breaks and propagates when the airfoil initiates the ramp motion. This can be seen in Fig. 4.11 by the light blue traces appearing for $8.0° < \alpha_{eff} < 12.0°$, for $\Omega^+ = 0.05$, and $8.0° < \alpha_{eff} < 15.0°$, for $\Omega^+ = 0.10$, along $0.5 < x/c < 1$. Figures 4.7 and 4.9 show that this process is characterized by the ejection of a primary separated flow structure from the mid-chord during the early stages of the airfoil motion.

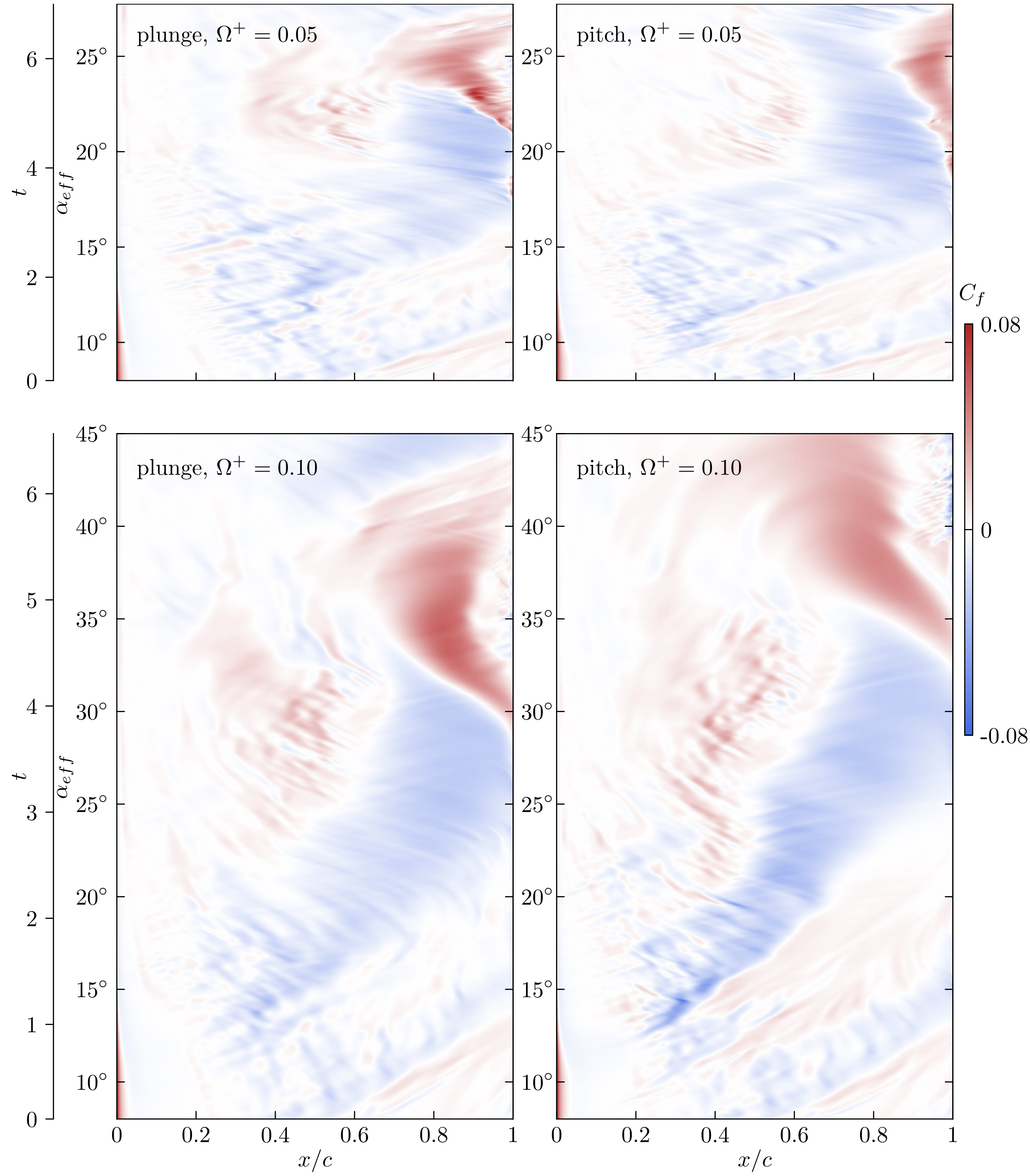

Figure 4.11: Comparison of skin friction coefficients of pitching and plunging ramp motions for $M_\infty = 0.4$, with $\Omega^+ = 0.05$ (top) and $\Omega^+ = 0.10$ (bottom).

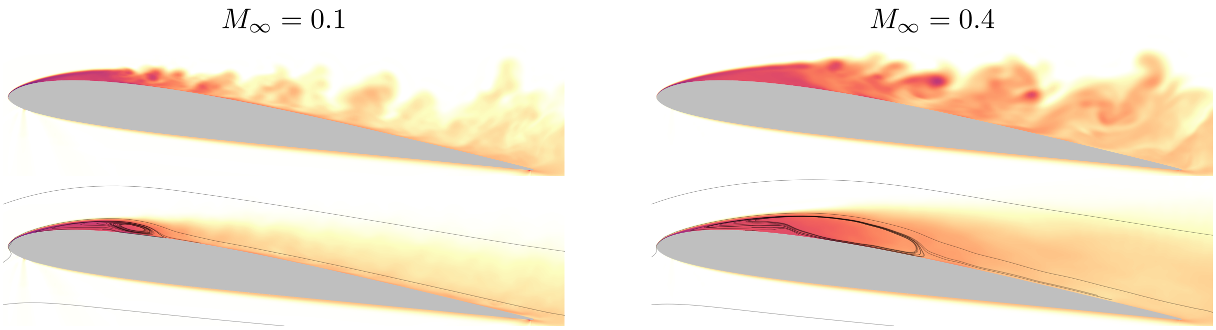

Figure 4.12: Top row: Instantaneous entropy contours immediately before the airfoil motion ($\alpha_{eff} = 8°$) for $M_\infty = 0.1$ (left) and $M_\infty = 0.4$ (right). Bottom row: Spanwise- and time-averaged result with streamlines revealing the presence of a separation bubble.

The different features observed for the two Mach number flows suggest the existence of a strong connection between compressibility and the characteristics of the separation bubble. Indeed, a recent work from Benton and Visbal (2020) shows that with an increasing Mach number the bubble burst started to occur at earlier angles of attack, and independently from the turbulent separation that moves upstream from the trailing edge (this feature is not present in our simulations). It was hypothesized that the shift from a trailing edge to leading edge stall process is due to the reduced entrainment of high-momentum fluid from the inviscid region into the separation bubble, which causes it to be larger and, thereby, more susceptible to bursting under an adverse pressure gradient. In our results, however, the separation process, even at $M_\infty = 0.1$, is already described as of leading edge type due to the absence of a turbulent separation from the trailing edge to trigger the bubble burst. Therefore, based on this hypothesis, by increasing the compressibility, we are bringing the separation bubble into a more vulnerable state, which explains the topological characteristics of the flow for the $M_\infty = 0.4$ cases.

Figure 4.11 also shows that, after the airfoil starts to move and the primary flow structure is ejected from the mid-chord, the flow develops to form the DSV, which is characterized by the darker blue contours in the figure. The precise timing for the onset of the DSV is hard to obtain from only a visual inspection of the skin friction maps, specially for $\Omega^+ = 0.05$. This is because the C_f patterns for $M_\infty = 0.4$ are more diffuse, which indicates that the DSV is weaker and more evenly distributed over the airfoil. At this higher Mach number, larger discrepancies appear in the skin friction maps between these two types of motion. For instance, one can see that the DSV is more diffuse and slightly shifted downstream for the plunging motion at $\Omega^+ = 0.10$ (notice the wider blue region in the bottom left subplot in Fig. 4.11 in comparison to that from the right hand side). This is also confirmed by Fig. 4.10 (in the second column), where the low-pressure core for the pitching motion appears to be more concentrated. Furthermore, large differences can be found regarding the TEV. For $\Omega^+ = 0.05$, the red region above $\alpha_{eff} = 20.0°$ exhibits a significant entrainment upstream of the trailing edge for the plunging motion, which results in clipping the blue trace marking the signature of DSV between $0.6 < x/c < 0.8$

at $\alpha_{eff} \approx 24.0°$. The same does not occur for the pitching airfoil, where we observe that the blue region extends throughout the entire time period analyzed. According to Fig. 4.8 (last column), these differences are a consequence of the interaction between the DSV and TEV that makes the former to be ejected away for the plunging airfoil. Finally, for $\Omega^+ = 0.10$ (bottom row of Fig. 4.11), the TEV is formed earlier during the plunge motion and the evolution of the skin friction for $\alpha_{eff} > 35.0°$ is significantly different between the two types of motion. One should notice, for example, the presence of a negative C_f region for the plunging airfoil at $\alpha_{eff} > 40°$. This is due to the formation of a second LEV which does not appear for the pitching case. This LEV is responsible for the drastic increase of lift and drag coefficients reported in Fig. 4.9 for the plunge motion.

4.4 Smoothing function term

As discussed in the beginning of Chapter 4.2, the exponential terms appearing in Eqs. 4.3 and 4.4 are used to smooth out the initial transient. Therefore, it is important to ascertain the sensitivity of the solutions to the smoothing function used to enforce a physical (finite) airfoil acceleration. The reason for that is because the exponential term acts on the descent velocity for the plunging cases and $\dot{\alpha}_{eff} \propto \arctan(-\dot{h}(t))$, while in Eq. 4.4, it acts directly on the pitch rate with $\dot{\alpha}_{eff} \propto \Omega^+$. As a consequence, there is a time lag in the effective angle of attack between the pitch and plunge motions when the exponential smoothing term is present, which could lead to slightly different flow dynamics and impair the comparison between them. Such time lag is observed in Fig. 4.13 that describes the effective angle of attack as a function of time for the two types of motion, with and without the smoothing term. The red line in this figure represents the function $\alpha_{eff} = \alpha_0 + \Omega^+ t$, which is followed by both pitching and plunging motions when the exponential term is not accounted for. As one can see, the plunging motion has a steeper acceleration at the early stages of the airfoil descent, forcing the angle of attack to quickly converge to the red line. On the other hand, the pitching motion has a delay to reach a nominal angle of attack, what creates a time lag with respect to plunging. As the rate Ω^+ increases, this lag becomes more evident even though it is less than 1°.

In order to investigate the impact of the added smoothing term in Eqs. 4.3 and 4.4, we compare simulations with and without it by means of the aerodynamic coefficients. Results are shown in Figs. 4.14 and 4.15 for the plunging and pitching cases, respectively. For the pitching case, a discontinuity appears in the aerodynamic loads in the early stage of motion when the smoothing term is not present, but the same does not happen for the plunging simulations. In both figures, we notice a more prominent disagreement occurring between the solid and dashed lines during high angles of attack, either when the DSV detaches or the trailing-edge vortex starts to form. The deviation of the solid

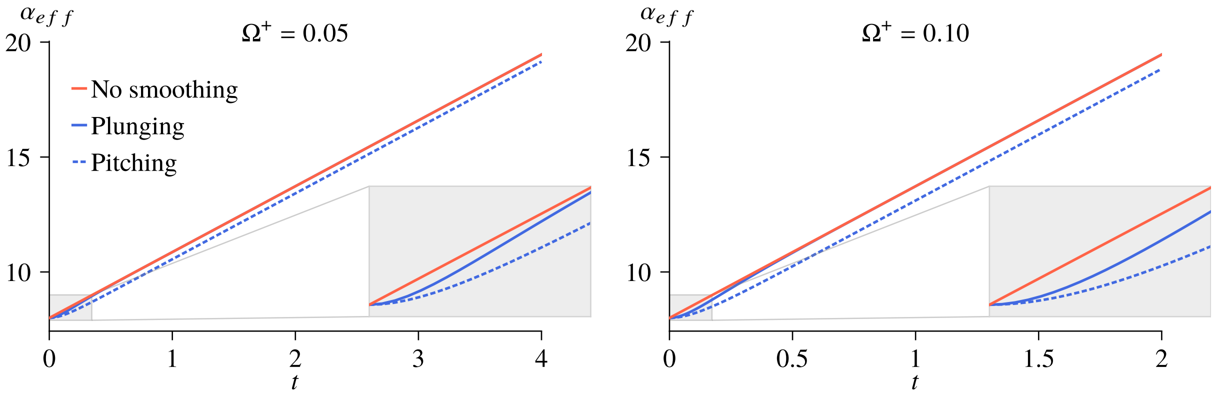

Figure 4.13: Effect of the exponential smoothing function on the effective angle of attack for $\Omega^+ = 0.05$ (left) and 0.10 (right).

and dashed lines is even more pronounced in the plunging case at $M_\infty = 0.4$ (red lines), which may be related to the steeper rate $\dot{\alpha}_{eff}$ during the earlier stages of the airfoil descent, as shown in Fig. 4.13. These results demonstrate the existence of a robust region of pitch-plunge equivalence at low angles of attack. However, at high incidence angles, the trailing-edge vortex dynamics causes the airfoil response to differ even when the same motion is being considered due to the high sensitivity to the initial conditions. This poses a challenge to the development of models for pitch-plunge equivalence at high incidence angles. Anyway, the time delay introduced by the smoothing term does not drastically affect the flow response up to the trailing-edge vortex formation, making it possible to draw a fair comparison between the two types of motion.

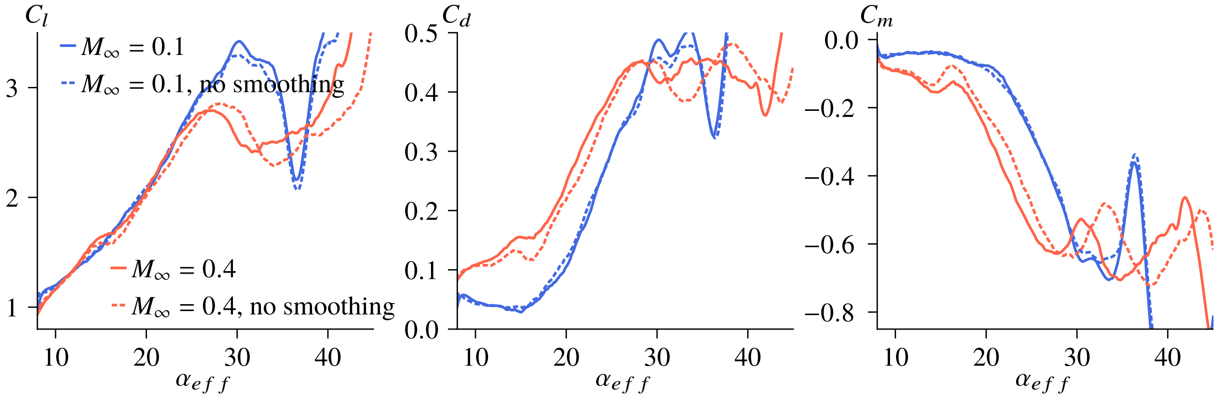

Figure 4.14: Effect of the exponential smoothing function on lift, drag and moment coefficients for $M_\infty = 0.1$ with $\Omega^+ = 0.10$ (plunging ramp motion).

4.5 Grid refinement

As mentioned in the beginning of Chapter 4, the grid used in this work was based on previous studies reported in the literature and followed the best practices with regard to grid resolution (Visbal, 2011; Ramos *et. al*, 2019) and spanwise extension (Visbal, 2011; Visbal and Garmann, 2018; Benton and Visbal, 2019b, 2020). However, to strengthen our

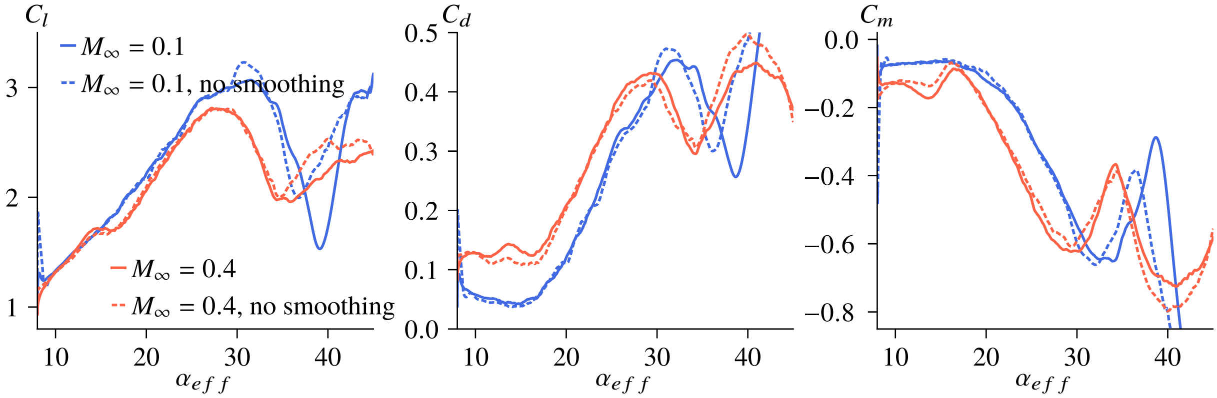

Figure 4.15: Effect of the exponential smoothing function on lift, drag and moment coefficients for $M_\infty = 0.1$ with $\Omega^+ = 0.10$ (pitching ramp motion).

conclusions, we designed a refined mesh with 25 to 40% improvement in resolution on the suction side, depending on the direction (streamwise, wall-normal or spanwise).

In this section, we compare results for pitching and plunging motions considering $\Omega^+ = 0.10$ and $M_\infty = 0.1$ for two different grid resolutions. The first grid is the one used to obtain the results displayed in the manuscript. It has 480 × 351 × 32 points and will be labeled as “grid 1”. The finer grid, in turn, contains 576 × 444 × 120 points, and will be labeled as “grid 2”. Moreover, to certify that the $s/c = 0.1$ span length was indeed sufficient to accurately represent the current dynamic stall problems, we performed an additional simulation with $s/c = 0.4$ for the pitching airfoil considering “grid 1”, but with 128 points along the span to keep the spanwise resolution the same.

Figure 4.16 displays the results in terms of the aerodynamic coefficients for all grids tested. In blue color we have the plunging motion and both red and wine colors represent the airfoils undergoing pitching. The solid lines are the same results reported previously in the manuscript, i.e., it uses “grid 1” and $s/c = 0.1$, except for the solid wine color, which considers $s/c = 0.4$. The dashed lines represent the results for “grid 2” and $s/c = 0.1$. As it can be seen from the figure, the matching between solid and dashed lines is excellent up to nearly $\alpha_{eff} = 25°$, which coincides with the instant when pitch and plunge deviate from one another for this particular rate Ω^+. Results of both motions follow similar trends for the grid resolutions and spanwise extensions investigated. Major differences appear in the pitching case, which show a drops in Cl and Cd, and a peak in Cm, slight shifted in phase, at $\alpha_{eff} = 36°$. This effect, however, is mostly related to small differences in the initial state of the flow from one grid to the other. In the previous section we observe that even with the same grid, a small difference in the initial conditions significantly influences the behavior of the pitching motion at high α_{eff} (see blue lines in Fig. 4.15).

The local flow structures are compared in terms of pressure coefficient and entropy measure for selected time instants in Figs. 4.17 and 4.18. For the plunging motion (Fig. 4.17), the evolution of the DSV is very similar between the two grids. The pitching motion (Fig. 4.18), on the other hand, exhibits more pronounced variations in the location of the DSV for angles beyond $\alpha_{eff} \approx 25°$, which justifies the behavior observed in the

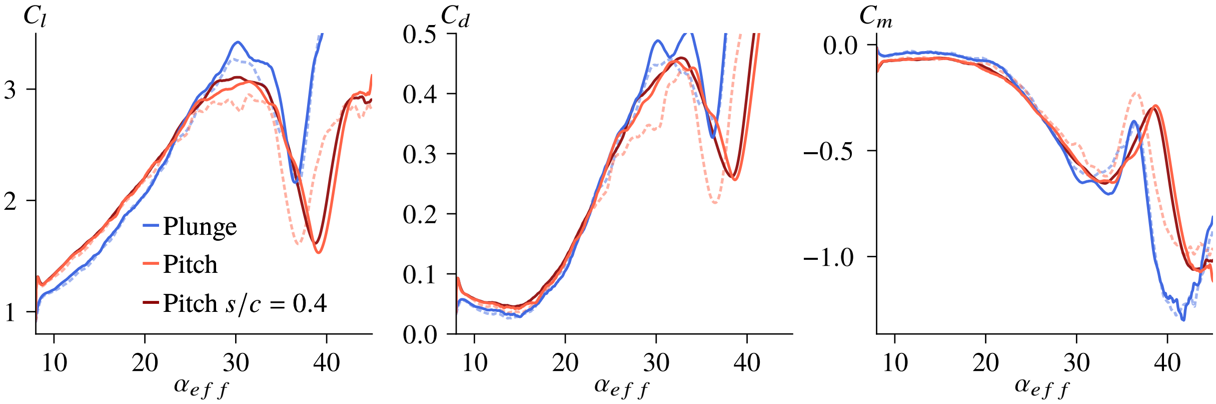

Figure 4.16: Influence of grid resolution and spanwise extension on lift, drag and moment coefficients for pitch and plunge ($M_\infty = 0.1$ and $\Omega^+ = 0.10$).

aerodynamic loads. In summary, this grid refinement study shows that “grid 1” provides sufficient accuracy for the pitch-plunge equivalence analysis considering the present flow parameters. Moreover, it also shows that a span of $s/c = 0.1$ suffices to properly represent the DSV onset and evolution.

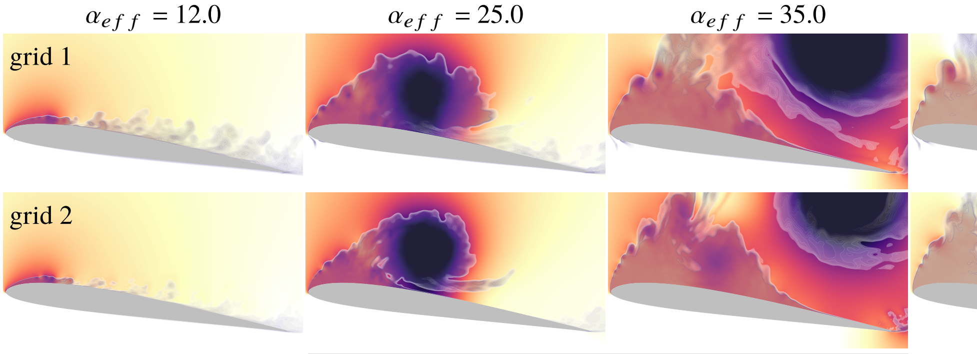

Figure 4.17: Pressure coefficient and entropy measure for a plunging airfoil at $M_\infty = 0.1$ and $\Omega^+ = 0.10$, comparing the two grid resolutions.

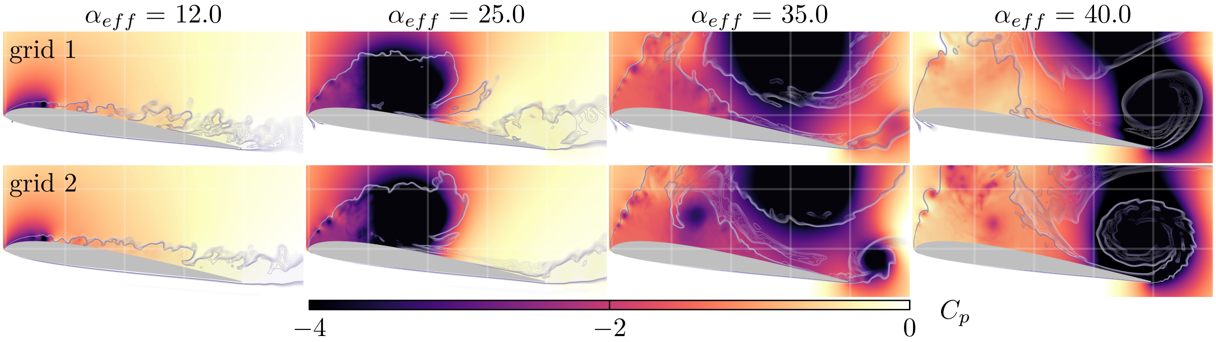

Figure 4.18: Pressure coefficient and entropy measure for a pitching airfoil at $M_\infty = 0.1$ and $\Omega^+ = 0.10$, comparing the two grid resolutions.

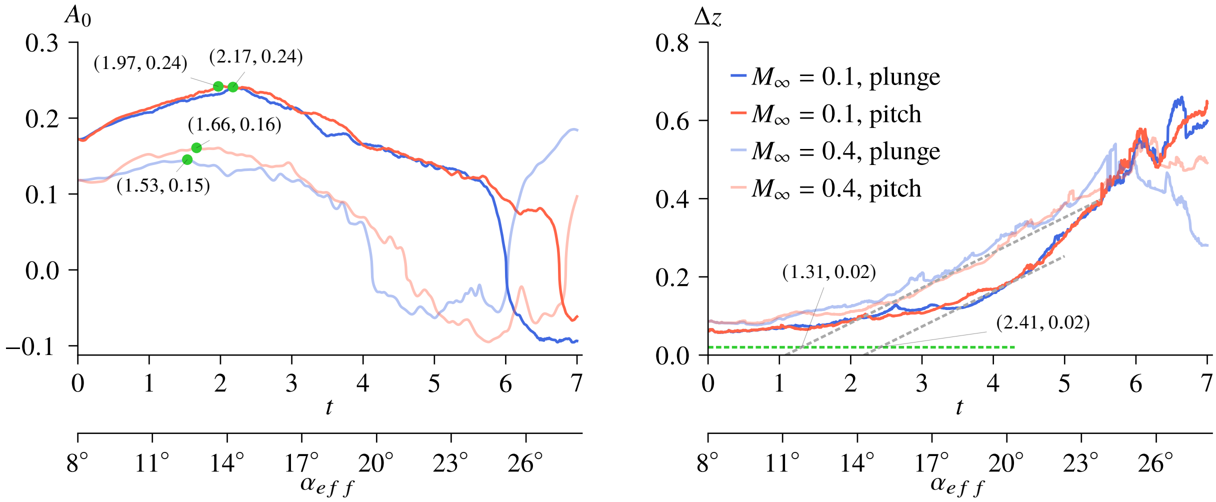

Figure 4.19: LESP (left) and shear layer height (right) for $M_\infty = 0.1$ and $M_\infty = 0.4$ for the ramp motion with $\Omega^+ = 0.05$.

4.6 Analysis of empirical criteria for dynamic stall onset

In the present section, we evaluate the leading edge suction parameter and shear layer height for the airfoils undergoing ramp motion. Results are shown in Figs. 4.19 and 4.20 for $\Omega^+ = 0.05$ and 0.10, respectively. One can observe that A_0 is drastically affected by compressibility, with lower LESP values obtained as the freestream Mach number increases. It is interesting to note that variations in the critical value of A_0 due to compressibility are much more pronounced than due to changes in the airfoil motion. For instance, pitching and plunging configurations have similar critical A_0 values for a fixed M_∞, with the largest difference observed for $M_\infty = 0.4$ and $\Omega^+ = 0.10$. The influence of the rate Ω^+, in turn, can be seen through the comparison of Figs. 4.19 and 4.20 for a fixed Mach number and type of motion. It is worth mentioning that, in the analysis of Figs. 4.19 and 4.20, we are only focusing in the states prior to the moment when the dynamic stall vortex is formed, i.e., before the maximum value of A_0.

At this point, we can infer that the critical LESP increases with the rate of motion. This trend was reported by Deparday and Mulleners (2019) for an airfoil under periodic motion, but nothing was said about the compressibility effects on the LESP. Here, we investigate how different compressible regimes alter the prediction capabilities of the LESP model. At a first glance, it may seem that the increment of the critical LESP is caused by a higher local Mach number near the leading edge with increasing rate Ω^+. This statement sounds reasonable as a higher suction could be associated to a higher local Mach number. However, our results show that the role of compressibility is the opposite: increasing the freestream Mach number reduces the values of A_0. The explanation for this contradictory behavior can be taken from the flow topology shown in Figs. 4.2, 4.8,

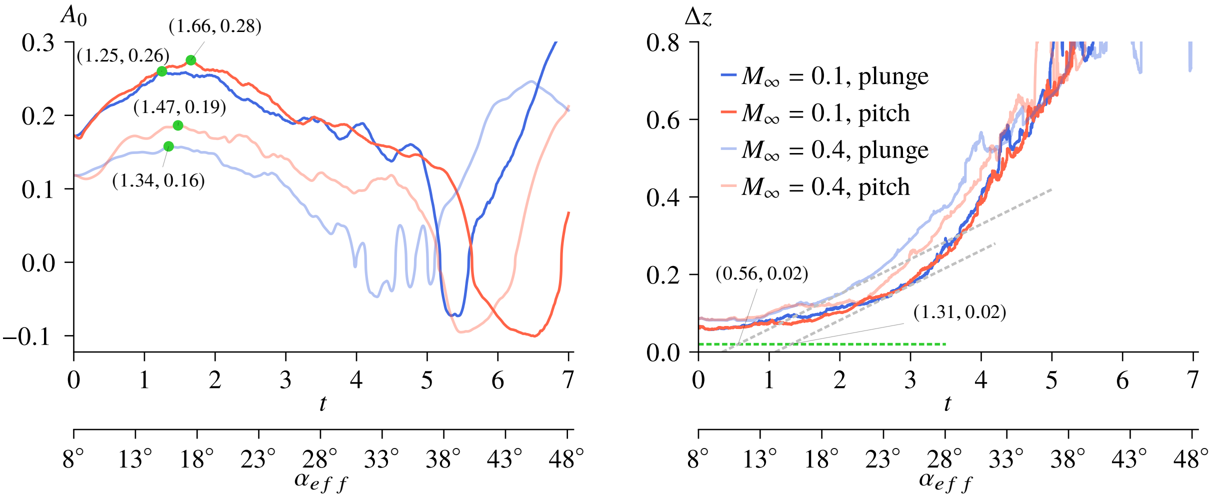

Figure 4.20: LESP (left) and shear layer height (right) for $M_\infty = 0.1$ and $M_\infty = 0.4$ for the ramp motion with $\Omega^+ = 0.10$.

4.4 and 4.10, which presents all the setup variations employed in our simulations. If we consider the $\alpha_{eff} = 17.5$ column for a given type of motion just for illustrating purposes, we observe that as one increases the rate Ω^+ for a fixed Mach number, the pressure in the leading edge region is reduced and, consequently, the magnitude of the suction vector becomes larger. For a fixed rate, on the other hand, the increasing Mach number causes the low pressure core to be more diffuse and weaker, what translates to a smaller leading edge suction. Another conclusion drawn from Figs. 4.19 and 4.20 is that the onset of the DSV occurs at lower effective angles of attack for lower values of Ω^+.

The temporal evolution of the shear layer height for the ramp simulations is shown in the right hand side of Figs. 4.19 and 4.20. Miotto *et. al* (2022) computed the critical Δz for an airfoil undergoing a periodic plunging motion. This parameter was obtained by the intersection of linear fits between a primary instability stage and the vortex formation stage. In the periodic motion, the primary instability stage is defined by the appearance of Kelvin-Helmholtz structures that move upstream near the airfoil surface and trigger the onset of the DSV. For the ramp simulations, however, the critical value could not be measured directly from the ramp data due to the nonexistence of a well defined stage of primary instabilities. Furthermore, in the ramp motion, the shear layer height keeps increasing constantly, what makes it hard to specify a proper fitting line. Besides that, the threshold of $\Delta z = 0.02$ obtained in the periodic airfoil simulations has already been exceeded even before the airfoil started to move. This value is represented in Figs. 4.19 and 4.20 by the horizontal dashed green line. The many different attempts made to find the critical parameter based only on the data from the ramp motion resulted in a wrong prediction of the dynamic stall onset, in the sense that it did not match the time in the skin friction maps (Figs. 4.5 and 4.11) in which one could consider as a potential point where the dynamic stall vortex initiates.

Based on the assumption that there exists a minimum threshold for the nondimensional growth rate of Δz for the shear layer to roll up into a primary dynamic stall vortex, we are able to determine the moment when the onset of dynamic stall takes place using only the information of the shear layer height. For that, we collect the growth rate of Δz during the vortex formation stage and its critical value from the previous study of an airfoil in periodic motion (Miotto *et. al*, 2022) and apply it to the ramp cases. This assumption holds for our simulations but its robustness to other airfoil kinematics and flow conditions needs further investigation. For instance, we cannot infer how different reduced frequencies of the periodic motion would affect the growth rate of the chord-normal shear layer height during the vortex formation stage.

From the results of the periodic motion, we observed that the growth rate of Δz ranged from $\partial \Delta z / \partial t = 0.09$ to 0.11, depending on the time interval used in the least square fit. Hence, using the value 0.10 as the minimum threshold, we draw a line $\Delta z = 0.10\ t + B$, where B is to be determined through visual inspection in such a manner that this line touches the curve for Δz from the right. This means that we are finding the region beyond which the roll up of the free shear layer is capable of forming a large and self-sustained dynamic stall vortex. These lines are dashed and represented in gray color in Figs. 4.19 and 4.20. After projecting it towards the threshold chord normal distance, 0.02, represented by the green dashed line, we obtain the location of the dynamic stall onset. This procedure seems to be suitable for cases of ramp motions, where usually a large separation is already present.

When the rate is $\Omega^+ = 0.05$ and the Mach number is fixed at a given value, not only the maximum A_0 seems to be almost invariant to whether the airfoil is performing a plunging or a pitching motion, but also the time when the onset of dynamic stall occurs is very alike. This is verified by the abscissa of the coordinates of the green dots in Fig. 4.19. However, the onset times from the critical Δz obtained with our approach do not match those from A_0. For $M_\infty = 0.1$, the onset of the DSV based on A_0 is around $t \approx 2$, while it is shifted to $t = 2.41$ when using the Δz criterion. The opposite occurs for $M_\infty = 0.4$, in which it goes from $t \approx 1.60$ for A_0, to $t = 1.31$ for Δz. Although these differences in the abscissas may lead to questioning of the methods, their values are reasonably accurate. From the skin friction maps (see the first row of Figs. 4.5 and 4.11), one can verify that the abscissa values of the green dots and that of the dashed line crossings in Fig. 4.19 meet a plausible region where the dynamic stall is initiating.

Similar conclusions can be drawn from the simulations at $\Omega^+ = 0.10$ (see Fig. 4.20) except that, in this case, the abscissa of the intersection for the $M_\infty = 0.1$ simulations in the Δz plot lies in between the time span observed by the green dots in the A_0 plot. This fact supports the validity of the critical Δz value and, by consequence, the assumption that exists a minimum threshold for the growth rate of the shear layer to develop a dynamic stall vortex. Moreover, a distinct temporal evolution of Δz is noticed between pitching and plunging motions for $M_\infty = 0.4$, with a gap being formed between the red and blue transparent lines in Fig. 4.20. This makes the pitching motion to have the same onset indication of the $M_\infty = 0.1$ flow, *i.e.* $t = 1.31$, while the onset occurs at earlier times for the plunging airfoil. Such distinct evolution of the shear layer height between the two types of motion is somewhat expected, since the evaluation of Δz considers the entire suction side of the airfoil, thereby, taking into account the flow topology that results from each motion kinematics.

Once again, the skin friction maps of the simulations at $\Omega^+ = 0.10$ can be used to confirm the validity of the time indicated by the critical values in both A_0 and Δz criteria. Particularly, we would like to bring the attention to the plunging airfoil at $M_\infty = 0.4$ since this simulation exhibited a considerable deviation from its pitching counterpart in terms of the evolution of the shear layer height. This case is represented by the transparent blue line in Fig. 4.20 and by the bottom left map in Fig. 4.11. According to the LESP threshold, the dynamic stall onset of this case occurs at $t = 1.34$, which corresponds to nearly $\alpha_{eff} = 15°$. At this angle, represented in the C_f map of Fig. 4.11 by the second y-axis tick from bottom to top, an intense negative skin friction appears around $x/c = 0.4$ indicating that the dynamic stall vortex is already formed. The Δz criterion, on the other hand, says that the onset takes place at $t = 0.56$, or at nearly $\alpha_{eff} = 11°$. This angle is just above the first tick that marks $\alpha_{eff} = 10°$ in the skin friction map and coincides with the region around $x/c = 0.3$ from which the dynamic stall vortex seems to be originated. Hence, the onset moment indication from Δz appears to be more precise in this situation.

4.7 Flow modal decomposition

Recently, Miotto *et. al* (2022) showed that despite the DMD algorithm being able to obtain the dynamic modes that correspond to the harmonics of an airfoil under periodic motion, it fails to extract the modes associated to the onset of the dynamic stall vortex. As a consequence, the standard DMD algorithm does not improve our understanding of the underlying physics that governs the stall onset. The reason for the limiting capability to extract physically meaningful modal features is that the DMD considers the modes to exist throughout the entire temporal window analyzed. In the ramp motion, this problem becomes even more evident as the airfoil kinematics and, consequently, the flow dynamics, are transient in nature and there is no motion periodicity implied. Moreover, depending on the time period considered in the construction of the linear operator, different results can be obtained since the dynamics are constantly changing over time.

To illustrate how the algorithm performs in the ramp simulations, a few dynamic modes of a plunging airfoil at $M_\infty = 0.1$ and $\Omega^+ = 0.05$ are shown in Fig. 4.21. The pressure coefficient is used to build the snapshot matrix and we consider 1400 snapshots from $0 \leq t < 7$. From this figure, it is clear that the modes carry information from

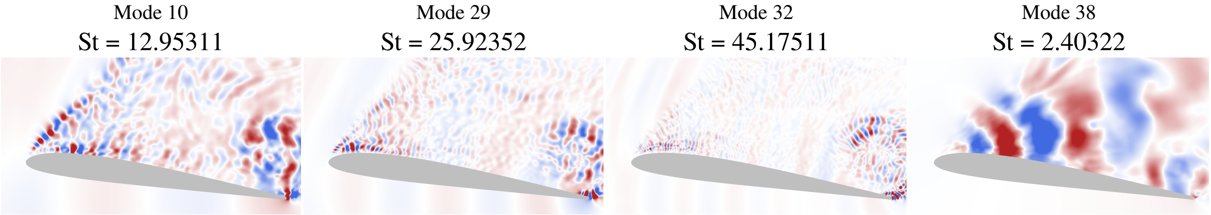

Figure 4.21: DMD modes for plunging ramp motion at $M_\infty = 0.1$ and $\Omega^+ = 0.05$.

post-stall stages with dynamical structures indicating the presence of the trailing edge vortex, besides the onset and transport of the dynamic stall vortex. It is worth mentioning that almost all DMD modes have similar behavior. The presence of this large number of similar modes is not only attributed to the transient nature of the problem, but also to the inability of SVD-based approaches to handle data with embedded rotations, translations, and scaling (Mendible *et. al*, 2020), which results in several spurious modes.

Since the mrDMD approach is able to handle symmetries and translations (Kutz *et. al*, 2016), we apply it in the ramp simulations seeking to extract low rank embeddings of the data from which one can infer a possible physical interpretation. Results are shown in Figs. 4.22 and 4.23 for $\Omega^+ = 0.05$ and $\Omega^+ = 0.10$, respectively. In both figures, we selected and displayed the modes in such a way that similar structures belonging to a certain resolution level and bin could be compared among the different types of motion for a fixed rate Ω^+ and Mach number. Again, by similar structure, we mean that their frequency and spatial distribution are alike. Moreover, in this procedure, we focus on selecting modes that could be related to the dynamic stall onset. Hence, the bin of a given resolution level is chosen to comprehend the inception period of the leading edge vortex.

Differently from what is observed in the periodic motion (Miotto *et. al*, 2022), the timing of the dynamic stall onset for ramp cases could not be determined precisely and seemed to be highly sensitive to the airfoil kinematics and freestream Mach number. We observed that the onset moment indicated by the critical A_0 and Δz values did not match, but they lie within an interval where the dynamic stall inception possibly occurs, confirmed by the skin friction maps. As a consequence, the columns of Figs. 4.22 and 4.23 do not necessarily compare the dynamic modes within the same time period. If we had kept the bin number always fixed, there would be no guarantee that the mode is indeed related to the stall onset for all situations present in that column. Thus, for each column, we fixed a resolution level and selected the modes with similar frequency and spatial distribution, but the bin location varies according to the Mach number in order to force the time window of the bin, Δt, to be contained inside $[\min(t_{A_0},\ t_{\Delta z}),\ \max(t_{A_0},\ t_{\Delta z})]$, where t_{A_0} and $t_{\Delta z}$ are the abscissa of the critical A_0 and Δz, respectively.

For the lower rate $\Omega^+ = 0.05$ shown in Fig. 4.22, the modes of the pitching and plunging motions are remarkably similar when the Mach number is fixed. The lower frequencies (St $\approx$ 10) shown in the first column of this figure appear to have little

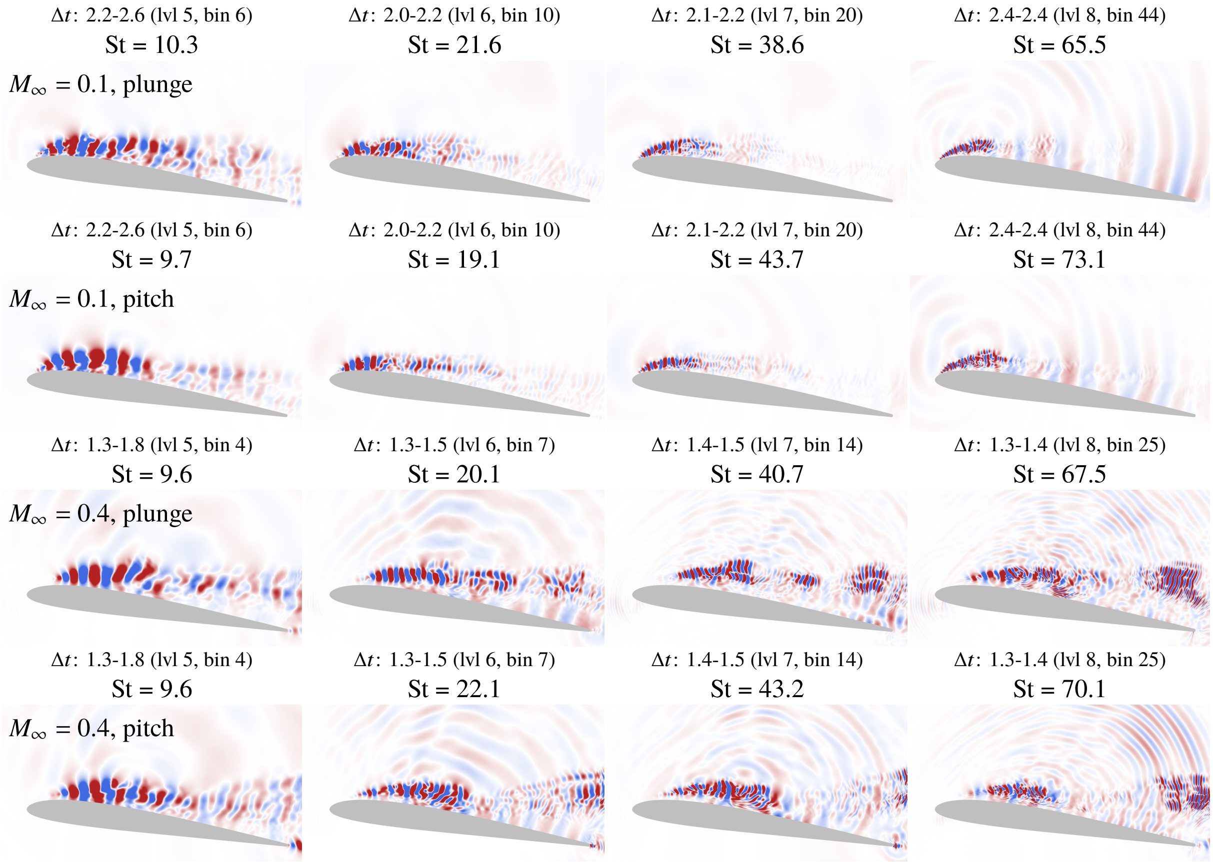

Figure 4.22: Multi-resolution DMD modes for $M_\infty = 0.1$ and $M_\infty = 0.4$ at $\Omega^+ = 0.05$.

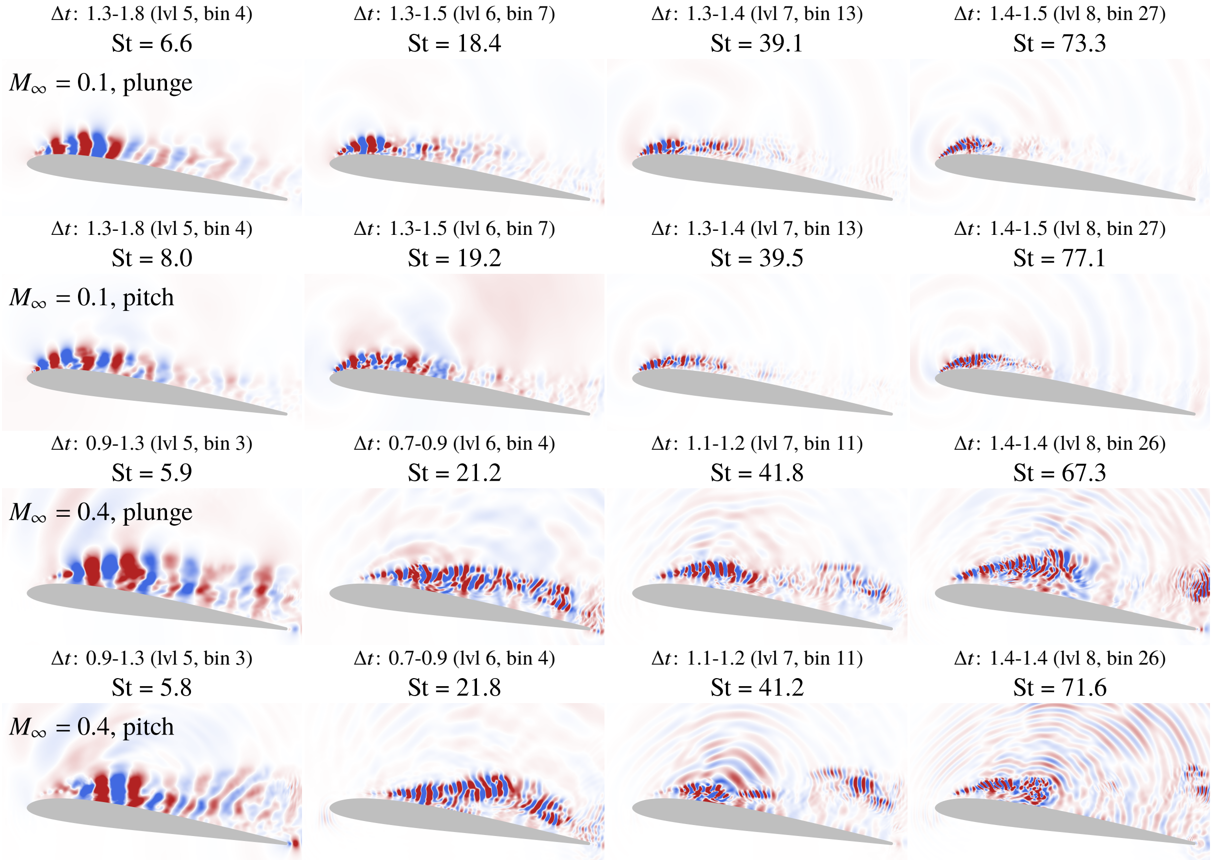

Figure 4.23: Multi-resolution DMD modes for $M_\infty = 0.1$ and $M_\infty = 0.4$ at $\Omega^+ = 0.10$.

dependency on compressibility, except for the fact that the spatial extension of the mode is slightly shifted downstream with increasing Mach number. However, at moderate and high frequencies (St $\gtrapprox 20$), the spatial distributions of the modes change considerably with compressibility. While the dynamic modes for $M_\infty = 0.1$ are more concentrated near the leading edge region, they become spread over the entire airfoil suction side for $M_\infty = 0.4$. This observation is related to the larger separation regions present in the higher Mach number flows for lower angles of attack.

It was discussed earlier that compressibility reduces the entrainment of high-momentum fluid from the inviscid region into the separation bubble. As result, the bubble becomes taller and more susceptible to burst under a weaker adverse pressure gradient. This translates into the formation of a larger recirculation zone shown by the streamlines in Fig. 4.12. The susceptibility of the bubble to burst, in turn, causes a coherent structure to detach from the mid-chord region when the airfoil starts to move when $M_\infty = 0.4$. This structure can be observed by the field of entropy measure above the trailing edge region in Fig. 4.2 (see the two bottom rows and two first columns), and also by the skin friction map in Figs. 4.5 and 4.11. In the mrDMD modes, this is expressed by the pattern appearing just above the trailing edge for the plunging and pitching flows at $M_\infty = 0.4$. Notice that the time window of the bin, Δt, coincides with the time when this primary separation from the mid-chord occurs.

Finally, Fig. 4.23 shows the selected mrDMD modes for $\Omega^+ = 0.10$. At this rate, even the low frequency modes change considerably for the different Mach numbers as shown in the first column. At $M_\infty = 0.1$, the flow event is concentrated closer to the leading edge region in comparison to the $M_\infty = 0.4$ case. The spatial distributions of the modes also become more disparate when one switches the type of motion between pitching and plunging. This opposes to the almost indistinct spatial distribution observed in the $\Omega^+ = 0.05$ cases in Fig. 4.22. In addition, these differences become more accentuated as the Mach number increases, what is somewhat expected given the drastic topological changes in the flows as previously observed. It is interesting to note, however, that the frequencies are similar, independent of the rate, type of motion, and Mach number.

5 Convolutional neural networks applied to dynamic stall

In this chapter, we present the results obtained with our CNN models. Despite being preliminary, these results are very promising and have been continuously improved by the author. Here, they will be presented in 3 different sessions. The first (§5.1) refers to regression models built to predict one or more scalar quantities, in this case, the aerodynamic coefficients. Two models were built, one for predicting lift, drag and quarter-chord pitch moment, and another for the distribution of C_p along the airfoil suction side. The convolutional layers process the pressure information by extracting features, which are gathered by the fully connected layers to obtain the aerodynamic coefficients. Hence, the difference between these two models resides only in the fully-connected layers, as discussed in §2.4.3. Although we tested several different neural networks, only the results for InceptionV3 will be shown here since this network had the lowest mean squared error among the networks tested. The second session (§5.2), in turn, presents the results of image-to-image translation using the U-net architecture. Given the u- and v-velocity inputs, the model is able to predict the pressure coefficient field with excellent accuracy. Finally, the last session (§5.3) discusses some possibilities where the concepts proposed here can be applied.

5.1 Prediction of aerodynamic coefficients

To speed up the training process and yield more accurate results, we used an InceptionV3 network pre-trained on ImageNet dataset. This model takes 299×299 RGB images of pressure coefficient field and estimates lift, drag and quarter-chord pitch moment coefficient. In Table 5.1, we present which simulations were used to train the neural network. Essentially, all pitching and plunging cases presented earlier in this thesis were included in the training set. After shuffling the collection of images, this dataset was devided into nearly 16,000 images for training, 2,000 images for validation and another 2,000 images for test.

After training, we achieved a loss of 2.2693×10^{-4} with mean square error of 3.5242×10^{-4} and a validation loss of 2.5085×10^{-4} with mean square error of 3.8655×10^{-4} at the 126th epoch. An early stopping with patience of 50 epochs was set to prevent unnecessary computation, which means that the neural network trained for 176 epochs. Results for the aerodynamic coefficients for 100 random images of the test set are compared against their true values in Fig. 5.1. In this figure, we observe that all 100 randomly

Reynolds	Motion	Mach	Rate / Reduced frequency
60,000	Plunge periodic	0.1	0.25
60,000	Plunge periodic	0.4	0.25
60,000	Plunge ramp	0.1	0.05
60,000	Plunge ramp	0.1	0.10
60,000	Plunge ramp	0.4	0.05
60,000	Plunge ramp	0.4	0.10
60,000	Pitch ramp	0.1	0.05
60,000	Pitch ramp	0.1	0.10
60,000	Pitch ramp	0.4	0.05
60,000	Pitch ramp	0.4	0.10

Table 5.1: Simulations used to train the neural network.

selected images predicted the airfoil response with a great accuracy.

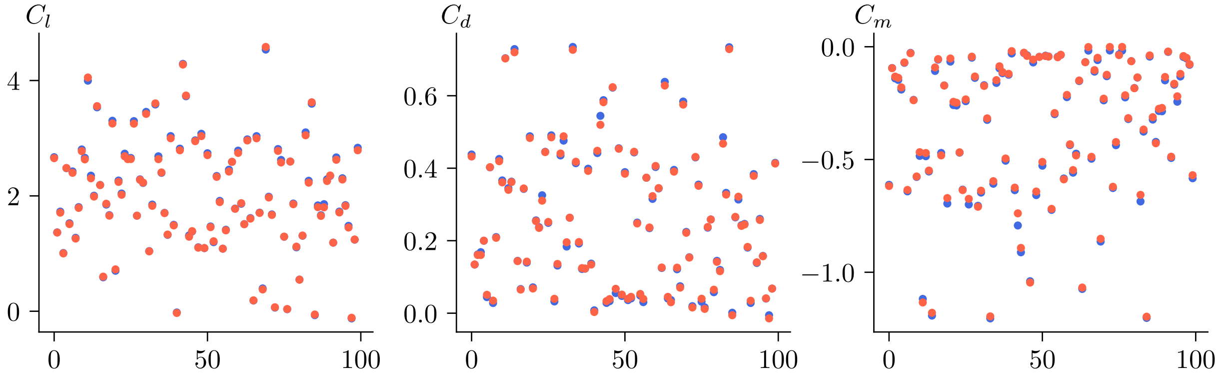

Figure 5.1: Comparison between true (red) and predicted (blue) lift, drag and quarter-chord pitch moment coefficients for 100 examples of the test set.

The previous result shows that the CNN is capable of processing the pressure information by extracting relevant features from the input image. This information was then translated into surface-integrated measurements, such as lift, drag and quarter-chord pitch moment coefficients. However, these responses come with easy in an experimental procedure. A more interesting result is the pressure distribution over the airfoil surface, as this type of measurement requires the installation of several probes, which can be structurally prohibitive or even very expensive. To this end, it is necessary to change the fully-connected layers of our CNN. The model mentioned above outputs 3 values in the last fully-connected layer, being one for each aerodynamic coefficient. Now, we want the outputs to represent the probe values over the airfoil surface. The modifications we made to the fully connected-layers was described in §2.4.3, to which the reader is referred for more details. To train this new model, it is possible to reuse the convolutional layers of our previously trained model and fine tune it. But here, we went with the convolutional block pretrained on the ImageNet dataset since this training only took about 9.5 hours in a NVIDIA Tesla A100.

In Fig. 5.2, we show the result for the C_p distribution over the airfoil suction side for some selected snapshots, which are reproduced in the right hand side of the figure.

These images belong to the test set, so they were never seen by the network. From the graphs, we observed a great agreement between the actual distribution of C_p and that predicted by the network. Some high-frequency fluctuations appear to be filtered out by the network, possibly due to the limited resolution of the input image. But, the significance of these results is much more optimistic: they tell us that if we can operate this model on experimental images, the pressure sensors could be replaced by a CNN-based model. This would have a huge impact on experimental campaigns. Before that, however, there are many issues that need to be addressed. For example, how does the model generalize to other flow or motion parameters? Can another fluid flow property be used as an input, such as velocity, which can be obtained directly from PIV?

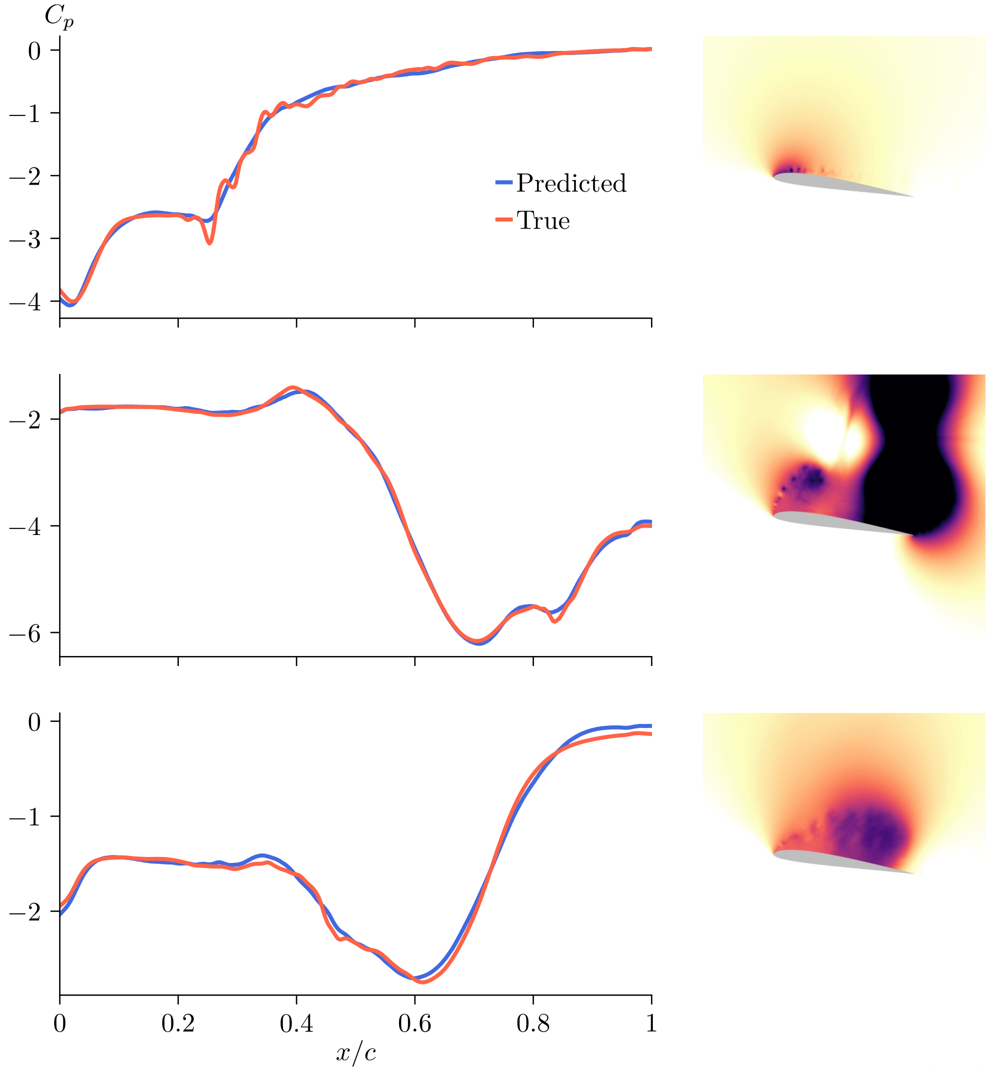

Figure 5.2: Pressure coefficient distribution over the airfoil suction side (left) and corresponding snapshot of pressure coefficient field (right). Top: plunge constant ramp with $\Omega^+ = 0.05$ and $M_\infty = 0.1$. Middle: plunge constant ramp with $\Omega^+ = 0.1$ and $M_\infty = 0.1$. Bottom: plunge periodic with $k = 0.25$ and $M_\infty = 0.4$.

As this is a work in progress, we do not yet have all the answers to these questions. But efforts have already been made in this direction. We start by investigating the model's ability to predict the airfoil response in a flow with an intermediate Mach number. For this, we run an LES of a periodically plunging airfoil at freestream Mach number of $M_\infty = 0.2$. Other parameters such as Reynolds number, reduced frequency, etc. were kept the same. Despite never seen an image of dynamic stall problem for $M_\infty = 0.2$, the network successfully predicted the airfoil response, as shown in Fig. 5.3. Remember that the model was trained with pictures of $M_\infty = 0.1$ and $M_\infty = 0.4$ flows. Thus, we verify that the model is able to interpolate between different compressible regimes. Here, we consider the network with 3 outputs (C_l, C_d and C_m), but similar conclusions are also drawn for the network that predicts the C_p distribution.

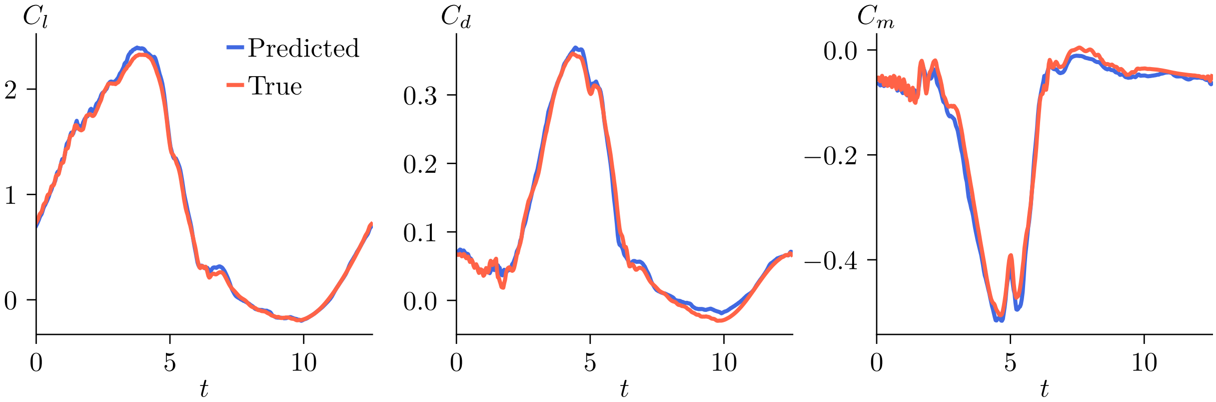

Figure 5.3: Lift, drag and quarter-chord pitch moment coefficient estimation for an airfoil at Mach number 0.2, never seen by the model.

We still need to verify that the model is able to extrapolate between flow parameters. This is probably a more delicate question, because depending on how far this extrapolation goes, the fluid behavior can be very different from what the network was trained on. For example, if we significantly increase the Mach number, the mechanism of dynamic stall formation will involve shock waves, which have never been seen by the neural network. We do not expect the model to be able to correctly interpret scenes with semantics very different from those on which it was trained.

To illustrate this, let us use the data we already have at hand. We have plunge simulations in periodic and ramp motion. In Fig. 5.4 we show how a CNN that was trained only in cases of ramp motion operates on images referring to periodic motion. In this figure, the blue lines were obtained by the CNN and the red ones indicate the correct results. The solid lines stand for images of $M_\infty = 0.1$ and the dashed lines for $M_\infty = 0.4$. The results show that the neural network prediction (blue lines) collapses at moments when the flow is reattached. This is because the model was trained on images in which the flow always had some degree of separation. Thus, the network could not predict that the airfoil would experience negative lift and also thrust, as in the red lines.

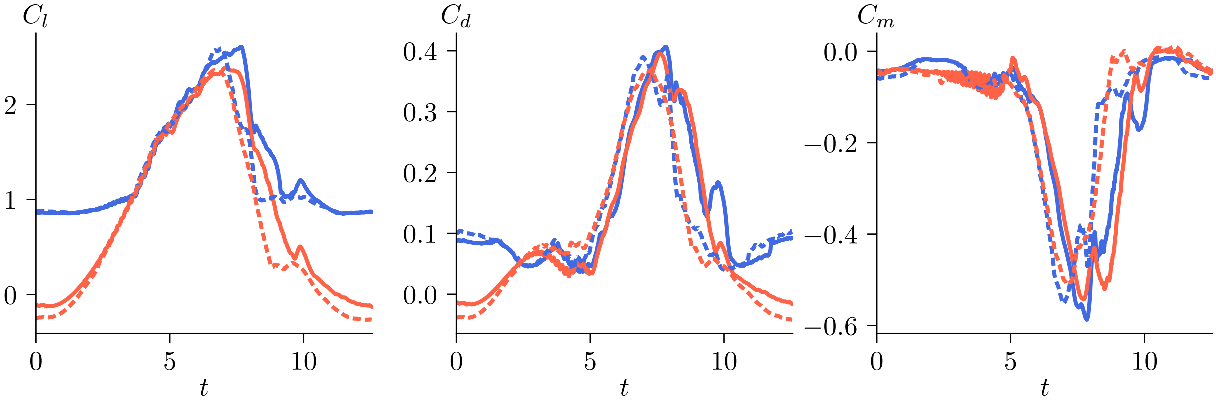

Figure 5.4: Results from a CNN trained on constant ramp-only data (blue) operating on cases of periodic plunging motion (red). Solid lines refer to $M_\infty = 0.1$ cases and dashed ones to $M_\infty = 0.4$.

We also tried the opposite situation: we trained our model on only periodic plunging airfoil data and operated on images of airfoils in constant ramp motion. The results are shown in Figs. 5.5 and 5.6, the first referring to a case of pitch in constant ramp motion with $\Omega^+ = 0.05$, and the second, with $\Omega^+ = 0.10$ rate. Again, solid lines indicate results for $M_\infty = 0.1$ and dotted lines for $M_\infty = 0.4$. In this scenario, the model has a better performance, especially for the lowest rate (Fig. 5.5). However, we still notice some discrepancies between the red and blue lines. For instance, the model under predicted the lift coefficient for $M_\infty = 0.1$ (solid lines) between $t = 4$ and $t = 6$ and it did not increase again after $t = 6$ as happens in the red line. This indicates that the dynamics in the trailing edge region is not being interpreted correctly by the model. However, it is worth mentioning that the network was trained with only 2 simulations of the periodic motion and also that, in this type of maneuver, the trailing edge vortex behaves very differently from the cases of ramp motion.

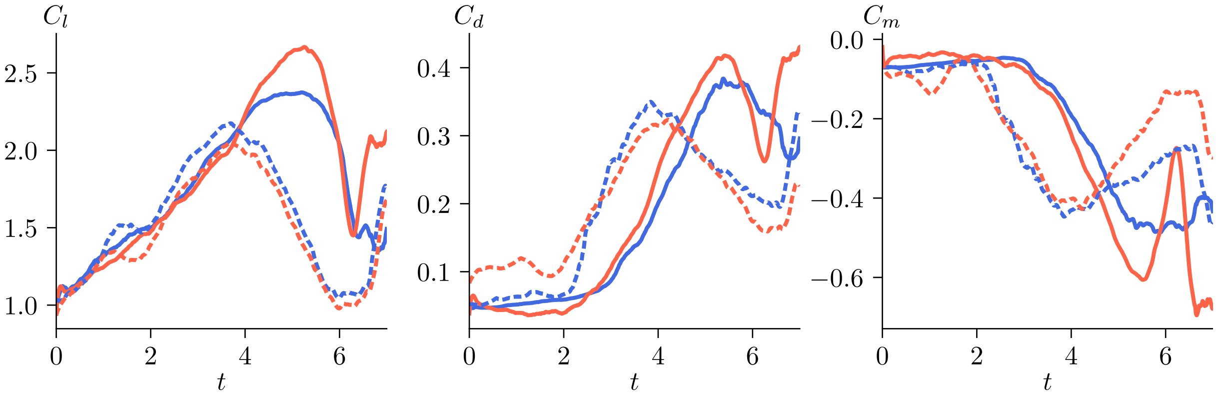

Figure 5.5: Results from a CNN trained on periodic plunging data (blue) operating on a constant ramp pitching airfoil at $\Omega^+ = 0.05$. Solid lines refer to the $M_\infty = 0.1$ flow and dashed ones to $M_\infty = 0.4$.

In essence, the network saw the DSV pass over the airfoil only twice and still was able to get most of the coefficients right for the case of $\Omega^+ = 0.05$. So, it can be said that the pitching-up airfoil at $\Omega^+ = 0.05$ and the periodic plunging airfoil share similar semantics.

But increasing the pitch-up rate Ω^+ affects the perception of these semantics, which can be verified by the more prominent mismatch between the red and blue lines in Fig. 5.6. By comparing Figs. 4.2 and 4.4, we observe that the position of the DSV with respect to the airfoil is a source of variability. Since this variability is not represented in the training set, as it contains only two simulations in which the DSVs follow similar trajectories, the model fails to generalize.

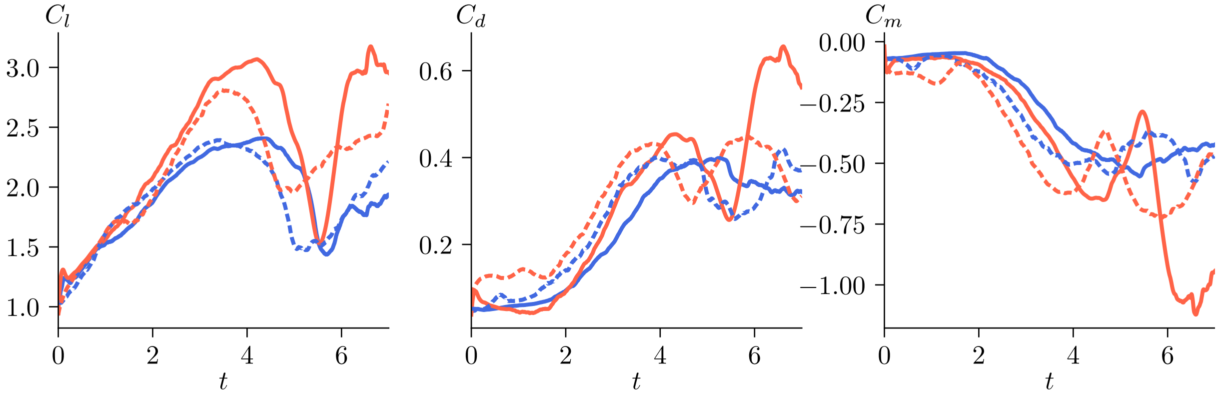

Figure 5.6: Results from a CNN trained on periodic plunging data (blue) operating on a constant ramp pitching airfoil at $\Omega^+ = 0.10$. Solid lines refer to the $M_\infty = 0.1$ flow and dashed ones to $M_\infty = 0.4$.

In summary, nuisance variability affecting the image domain will impair the generalization ability of the model. This means that any sources of variability must be included to force the model to learn it away. Fortunately, though, in fluid mechanics most of the nuisance variability is already known and can be dealt with at the outset. For example, we know that the position of DSV with respect to the airfoil is an important parameter to be learned. So, the annotations of DSV appearing in different positions must be included in our training if we want the model to generalize well. This goes in the same direction with regard to building models for extrapolation. If perceptually significant changes appear between this extrapolated condition and the annotated samples on which the network was trained, the model will likely fail.

The final question that we addressed in this thesis is that of using another fluid flow property as input of the CNN. For being directly obtained from a PIV technique, the velocity field is a good candidate for input. So, we build a model that takes images of u- and v-velocity components, concatenated channelwise, and predicts the aerodynamic coefficients. We are using the same InceptionV3 architecture from before (pretrained on ImageNet dataset) with 3 outputs in the fully-connected layers. The only difference is that it receives 2 input images at the same time. The results are shown in Fig. 5.7, obtained after training for 131 epochs, which corresponds to a loss of 0.0114 with mean square error of 0.0225 and a validation loss of 0.0043 with mean square error of 0.0077. The graphics displayed in this figure refer to the pitching-up airfoil with $\Omega^+ = 0.05$ in a $M_\infty = 0.1$ flow and they contain data from train, validation and test sets.

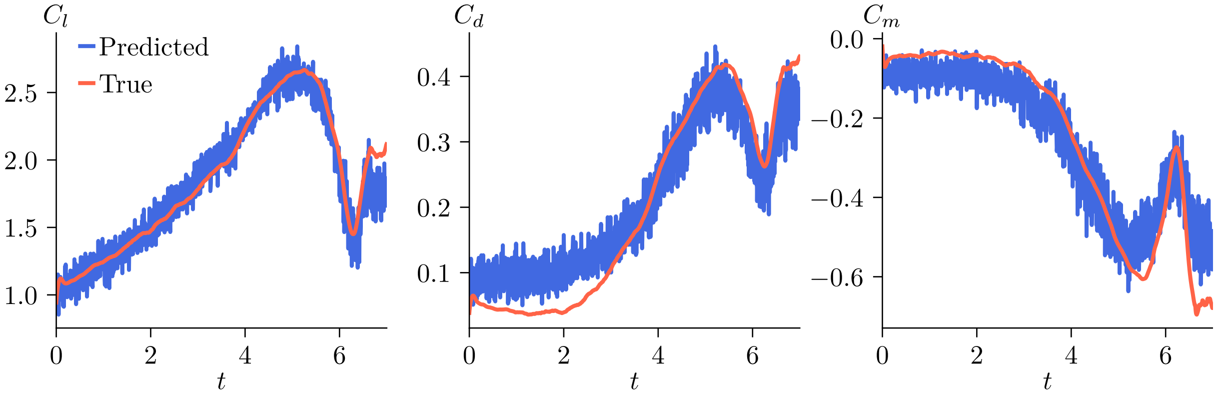

Figure 5.7: Lift, drag and quarter-chord pitch moment coefficient estimation using the velocity components as inputs.

From Fig. 5.7, we observe that the predicted coefficients oscillate around their annotated values. This could be due to a high-bias model or an irreducible error in the velocity data itself. By irreducible data error, we are not saying that the velocity field is wrong, but rather that this image is inherently too noisy for the task. To verify if the underfitting occurs due to high bias, we would need to use more complex networks. So far, to generate these results that consider velocity components as input, we only used the InceptionV3 network. So, we do not rule out the possibility that the result will be better with other architectures. However, for what matters, the pressure coefficient field is preferable to velocity when it comes to building our regression model. In principle, this makes sense, since pressure is directly related to forces (and consequently to aerodynamic coefficients).

5.2 Prediction of the pressure coefficient field

As we saw in the previous section, pressure coefficient is preferable to velocity when it comes to building our regression model. But the role that pressure plays in fluid flow analysis goes beyond simply obtaining aerodynamic loadings. In this session we will show how neural networks can be used to extract the pressure field from the fluid flow velocities. For now, all data used here come from numerical simulations. In fact, the neural network is trained only with data from numerical simulations. But soon, we seek to apply this model in experimental images to open new avenues in fluid flow analysis.

We draw on image-to-image translation and domain adaptation to amplify the scope of information extracted in experimental fluid mechanics. We uniquely treat the image semantic segmentation as an image-to-image translation task that infers semantic labels of structures from the input images in a supervised way. Particularly, given the source domain of numerically simulated images of the velocity field, we train a U-net (Ronneberger *et. al*, 2015) to generate synthetic pressure coefficient fields. Then, global photometric statistics of experimental images are manipulated using the Fourier Domain

Adaptation method proposed by Yang and Soatto (2020) to improve the alignment of the low-level statistics between the source and target distributions. This is especially important since the networks do not transfer well across different low-level statistics (Achille *et. al*, 2019).

In this thesis, only the results for the model operating in the source domain will be presented. The application of the domain adaptation technique is still an ongoing work since we currently lack experimental images of dynamic stall. Here, the U-net was trained for 58 epochs yielding a loss of 1.0293×10^{-4} with mean squared error of 2.0634×10^{-4} and a validation loss of 2.8063×10^{-4} with mean squared error of 5.6276×10^{-4}. The same dataset from the regression model was used to train the U-net. However, the u- and v-velocity components concatenated chanelwise were used as input instead of the C_p field. This last flow quantity is now the output of the supervised setting.

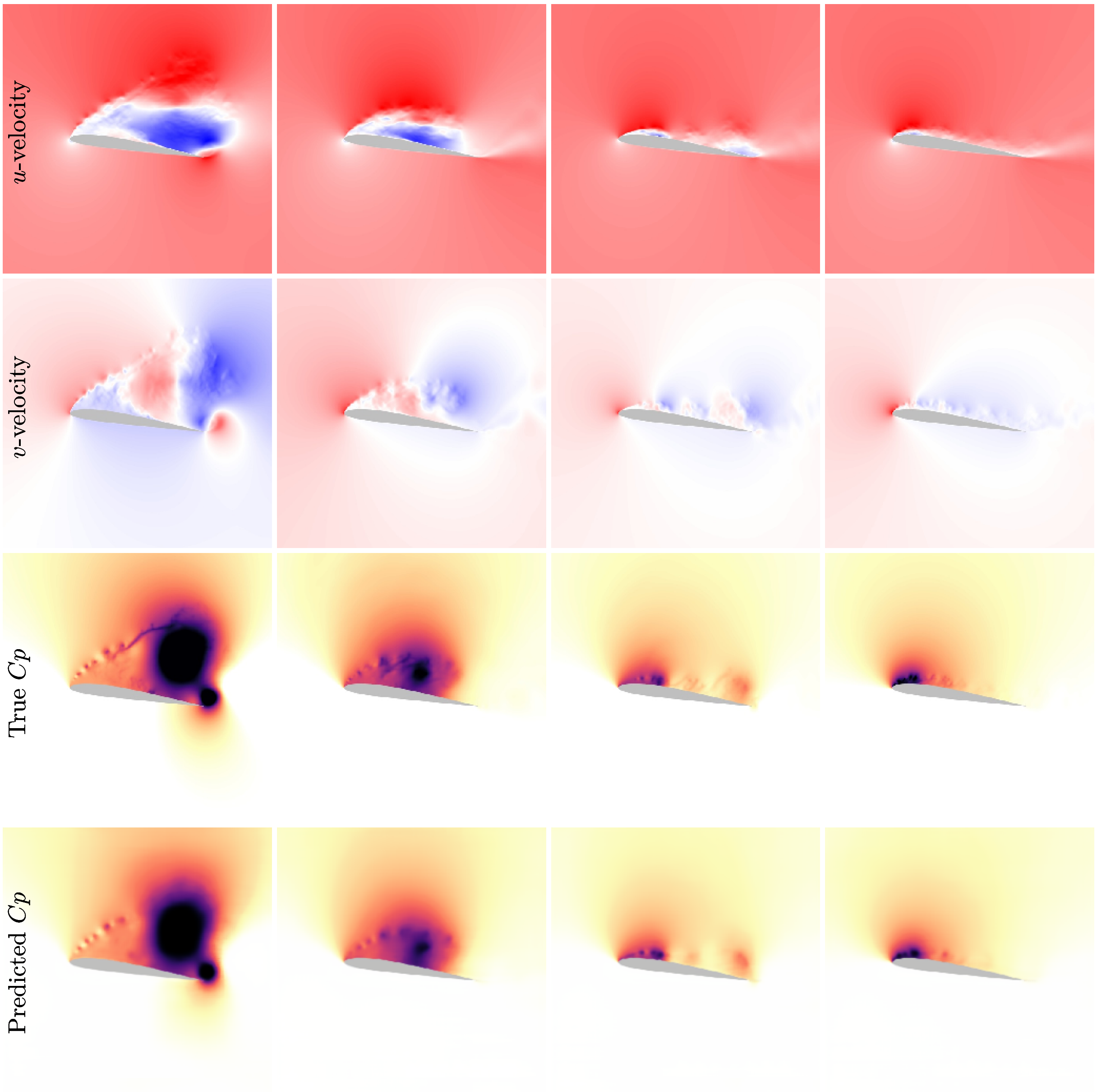

Figure 5.8: Input velocities and the comparison between true and predicted C_p fields.

Figure 5.8 shows the input velocities, the actual pressure coefficient fields and those predicted by the network. These results are displayed columnwise, each column corresponding to a snapshot randomly selected from our test set. An excellent agreement is observed between the true and predicted fields. This demonstrates that a simple encoder-decoder architecture can correctly map the input attribute values to the corresponding synthetic image. However, some fine details are missing out from the predictions. For instance, the tail-like structure appearing on top of the DSV in the first column is absent from the synthetic image. In the future, we plan tweaking the hyperparameters of the U-net and also using GAN architectures to improve these results. Moreover, we still need to evaluate how the synthetic C_p images perform as input of the regression models built previously. We hope that translating the velocity field into C_p at the outset can improve the loading estimation.

5.3 Other applications

In a previous section we showed how a U-net architecture, typically used for semantic segmentation tasks, can be used to translate across different flow properties. In our example, we mapped the velocity field to pressure given the importance it plays in fluid mechanics. However, the computation of other flow properties entails no overhead. We could have used density, temperature, vorticity, or any other property in place of pressure. The proposed framework is still a proof of concept, but the results are very promising and represents a first step towards our goal of amplifying the information content of experimental data.

In Appendix D, we demonstrate the usage of our method on barchan dunes. The U-net architecture is trained on images obtained from numerical simulations of fluid-particle interactions to establish the mapping relation between the dune morphology and the underlying particle forces at the grain scale. Since we already have access to experimental images of this problem[1], we will apply the domain adaptation technique on barchan dunes. This allows the acquisition of force measurements from experimental images, which would be impossible otherwise. As a result, we believe that this study can provide valuable insights to the the way sediment transport is modelled and to the grain scale dynamics.

---

[1] The numerical and experimental data of the barchan dunes are courtesy of Carlos Azael Alvarez Zambrano and Erick de Moraes Franklin.

6 Conclusions and Future Work

The present thesis has tree main contributions to the state-of-the-art of dynamic stall:

- Characterization of both the onset of dynamic stall and the overall flow physics during stall development;
- Better comprehension of the equivalence between pitch and plunge motions; and
- Development of surrogate models to analyze dynamic stall problems.

Each of these contributions is explained in detail below.

6.1 Dynamic stall onset on periodically plunging airfoils

Large eddy simulations are performed to investigate the onset and evolution of dynamic stall for an SD7003 airfoil undergoing a periodic plunging motion. Simulations are performed for freestream Mach numbers $M_\infty = 0.1$ and 0.4 for a fixed chord-based Reynolds number $\mathrm{Re} = 6 \times 10^4$ to examine phenomenological variations due to compressibility effects. Similar to previous observations reported for pitching airfoils, it is found that both the residence time and strength of the dynamic stall vortex (DSV) decrease for the higher Mach number flow. Hence, higher compressibility leads to lift and drag reductions caused by the weakened DSV, which occurs when the airfoil is ceasing its downstroke motion. For the rest of the periodic motion, the aerodynamic coefficients display similar features at both Mach numbers.

For the present configurations, the onset of dynamic stall is marked by two major flow features: a train of Kelvin-Helmholtz instabilities, referred here as primary instability stage, and a secondary instability stage due to the breakdown of vortical structures along a shear layer formed at the leading edge. With respect to the primary stage, acoustic waves are scattered from the trailing edge due to vortex shedding apparently triggering the formation of Kelvin-Helmholtz instabilities. This mechanism appears to be invariant to the freestream Mach number although it is observed that higher compressibility induces the flow to become more susceptible to three-dimensional spanwise disturbances.

With respect to the secondary stage of instabilities, the mechanisms of flow separation observed in the present plunging airfoil display broad agreement with the van Dommelen and Shen model for pitching airfoils. In this case, complex dynamics are observed along a shear layer formed at the leading edge. The evolution of this shear layer causes the flow to eject vortical structures outward from the surface. The flow dynamics are similar for both Mach numbers analyzed despite the different positions where they occur near the leading edge. These spatial variations are directly affected by the pressure gradient distributions over the leading edge. For $M_\infty = 0.1$, the pressure gradient becomes adverse sooner than for $M_\infty = 0.4$, and the pressure gradient fluctuations are stronger causing the shear layer to destabilize further upstream. We observe that the onset of dynamic stall is related to the interaction of both primary and secondary instabilities that occur near the leading edge.

In order to better characterize the stall onset, two empirical indicators are investigated: the leading edge suction parameter (LESP) and the critical chord-normal shear layer height, Δz. The influence of compressibility on these stall indicators is also assessed. It is observed that the maximum suction supported by the leading edge is reduced as compressibility increases, revealing that the LESP is not only a function of the parameters of the airfoil motion but also of the freestream Mach number. The Δz criterion, on the other hand, appears to be almost invariant to the freestream Mach number. We also find that, although both criteria fit the observable moment when the DSV forms, they tend to characterize the stall onset based on the point when the DSV detaches from the airfoil surface and not when the secondary instabilities set in. From the perspective of dynamic stall control, this fact reveals the need to create more conservative criteria to predict stall. This is necessary since flow actuation should be applied prior to the formation of the DSV.

A decomposition of the pressure coefficient field into dynamic modes is also performed to extract the low-rank spatial features from the datasets and their associated frequencies. The detailed description of the boundary layer state with the modal support can help the exploration of suitable actuation parameters for flow control. The standard DMD algorithm is able to identify the modes associated with the periodic motion and its harmonics, however, it fails to isolate the unsteady flow features that take place during the onset of dynamic stall. This limitation arises from the fact that the extracted modes exist throughout the entire temporal window analyzed. The multi-resolution variant of the algorithm (mrDMD), on the other hand, successfully extracts clean and physically interpretable modes for all cases investigated herein.

Although the spatial distribution of the modes related to the dynamic stall onset may vary with compressibility, their frequency content are much alike.The mrDMD captures the wavepacket structure of the Kelvin-Helmholtz instability and the modes associated to the separation process that lead to the formation of the leading edge vortex. The effects of increasing compressibility are also manifested in these modes. For instance, the sparser distribution of Kelvin-Helmholz instabilities, the larger size of the secondary separation of the shear layer and the displacement of the critical region further downstream of the leading edge which occurs when the Mach number increases are all represented therein.

6.2 Pitch-plunge equivalence

Large eddy simulations are performed to investigate the pitch-plunge equivalence for an SD7003 airfoil undergoing constant ramp motions. For that, the ramp motion of the plunging airfoils is set to match the geometric angle of incidence of equivalent pitch-up airfoils with fixed angular velocity. Two different rates of motion at which the effective angle of attack increases are employed and the freestream Mach number is varied in such a way that one can see how each parameter (type and rate of motion, and freestream Mach number) influences the equivalence. To be pragmatic, all simulations have the same initial state for a given freestream Mach number. This study represents an important step to discern how pitch and plunge motions behave when exposed to different compressible scenarios.

Results show that the pitch-plunge equivalence holds until the formation of the TEV for all rates of motion and Mach numbers analyzed. In this sense, the way the TEV interacts with the DSV differs between pitch and plunge, causing the aerodynamic coefficients to mismatch. After subtracting the rotation-induced apparent camber contributions present in the pitching case, we reconciled lift and moment coefficients for most of the time. However, this correction is not sufficient to extend the equivalence beyond the point when the TEV system begins. The birth and development of the DSV, in turn, is remarkably similar for the two types of motion, especially for low Mach numbers. This implies that the LEV formation and its subsequent evolution is strongly driven by the rate of change of the effective angle of attack.

Considerable topological changes occur in the flow fields when compressibility is varied, even before the airfoil initiates its motion. At the static angle of attack, the higher Mach number flow depicts a longer separation region formed further downstream the leading edge compared to that observed for the lower Mach number case. During the airfoil motion, the higher compressibility results in an overall increase of drag due to the more evenly distributed pressure forces over the airfoil chord. In addition, the residence time and strength of the DSV decrease with an increasing Mach number, the former being responsible for the earlier breakdown of pitch-plunge equivalence since the TEV begins to form at lower incidence angles.

Increasing compressibility also makes the peculiarities of each class of motion more pronounced. This is especially due to the primary separation arriving at the trailing edge region and the smaller residency time of the DSV. At the higher rate of motion, the DSV of the pitching airfoil evolves into a more concentrated structure. On the other hand, the incipient DSV is more diffuse for the plunging motion. These topological differences, however, do not compromise the pitch-plunge equivalence for lower angles of incidence, but reinforce the need for a more rigorous definition of the effective angle of attack that takes into account the trailing-edge dynamics and compressibility effects.

6.3 Applications of machine learning

Based on the pressure coefficient from the unsteady flowfield, a pre-trained InceptionV3 network rendered the backbone of a neural network model that links the existing flow structures to the aerodynamic coefficients. The CNN correctly inferred the attributes present in the flow image even in a compressibility regime for which no annotations were given. As a result, an excellent agreement between predicted and ground truth values was obtained. This fact demonstrates that CNN-based models can be used to interpolate between flow parameters. Now, more studies need to be conducted to determine the ability of the neural network to extrapolate the source domain. In this sense, we provide evidence that not including sources of variability in the training set can lead to a significant deterioration of the model's performance. By training our model on different types of simulation parameters, we demonstrate that the position of the DSV with respect to the airfoil as well as the trailing edge vortex are sources of variability that must be learned for the model to generalize well.

Our goal is to bridge the gap between numerical simulations and experiments. In this sense, the adoption of PIV techniques by fluid dynamicists forms a compelling argument for using velocities as input to our model instead of the C_p field. The results, however, show worse predictive accuracy for translating between velocity field and airfoil loadings. In principle, the direct relationship between pressure and force seems to support the claim that velocity data introduce irreducible errors. However, it is necessary to run more complex neural networks to be able to prove this.

The question of using velocities as input to the model is also addressed in tasks other than regression. Here, we use the velocities to synthesize the corresponding pressure coefficient field through an image-to-image translation. The results show that a simple U-net architecture can infer the semantic labels of structures present in the input velocity images. In fact, the proposed framework can be used to extract any physical quantity of interest and is not limited to estimates of C_p. Most of the fine-grained details in the scene was captured by the network, but we believe there is room for improvements in this regard. Finally, we intend to combine the aforementioned models with an unsupervised domain adaptation method to extract relevant information from experimental visualizations.

6.4 Future work

As we showed in this thesis, the transient nature of dynamic stall makes it difficult to extract physically meaningful structures from the application of standard DMD. In fact, the same holds if one analyzes probe signals of a dynamic stall problem using a Fourier scope. Fourier spectral analysis is a well-established method for examining the global energy-frequency distributions of linear, time-invariant systems. However, its resulting spectrum may be misleading if the process is not linear or if the data is non-periodic or non-stationary. The Hilbert-Huang transform (HHT) makes use of the *empirical mode decomposition* (EMD) to decompose the data into a finite and often small number of complete and nearly orthogonal basis functions, called *intrinsic mode functions* (IMFs); and of the Hilbert spectral analysis on these IMFs to obtain the energy-frequency-time distribution, designated as the Hilbert spectrum, from which the time localities of the events are preserved. In a future work, we are interested in applying the EMD and some of its variants to study the acoustics of dynamic stall and also to extract suitable actuation parameters for flow control. In this sense, we have seen that the frequency and spatial information provided by mrDMD offer a range of possibilities to explore various control actuations. We are now looking to gather the information obtained by these different techniques and use it to design actuators to suppress DSV formation or alleviate its impact on aerodynamic fluctuations.

Because the mrDMD was able to provide physically meaningful structures with spatial support and their frequency content, this technique can be used to explore the different trailing-edge systems between pitch and plunge motions. This research may provide directions for better comprehension of the causes of the equivalence breakdown. In this same line, we also seek to explore some other equivalence criteria that are based on recently-developed theories of unsteady aerodynamics.

Finally, we are currently working on accessing experimental data of dynamic stall to test our CNN-based method. As mentioned in §5.3 and in Appendix D, we are already working on the problem of barchan dunes. This study will continue and we believe that positive results will come from it. In addition, the robustness of the method to interpolate and extrapolate the source domain will be investigated considering a broader range of the parameter space. This includes Reynolds numbers and airfoil kinematic parameters (amplitude, rate, reduced frequency). Overall, if our optimistic observation comes to pass, it is possible that sensors will be replaced by neural network-based data. For instance, using our proposed framework, the velocities from PIV images could be first mapped to C_p field, which in turn will be used as input to a regression model that determines the wall forces.

6.4.1 Extending beyond the scope of this work

So far, we have listed some immediate possibilities for future work, given the new contribution to the state-of-the-art brought by this thesis. Despite the importance of providing a direct continuation of the present work, the dynamic stall problem is not limited to the scopes discussed here. Thus, in this session, we leave other possibilities for future work that extend beyond what we studied, but which are still relevant to the research topic.

Because vertical axis wind turbines (VAWT) operate at lower speeds, lower height, and have a different visual signature, they have greater potential to be deployed in urban settings than conventional wind turbines. The benefits also extend to environmental and health issues. Several studies link the noise generated by wind turbines to annoyance and sleep disorders (Karanikas *et. al*, 2021; Monazzam *et. al*, 2019; Botelho *et. al*, 2017), as well as impacts on birds and wildlife (DREWITT and LANGSTON, 2006; Shaffer and Buhl, 2016; Dai *et. al*, 2015; Chowdhury *et. al*, 2022). In this sense, the lower sound emission of VAWTs (Chowdhury *et. al*, 2022) brings another competitive advantage in the search for sustainable solutions in power generation. However, the emergence of VAWT as a renewable energy source has been hampered by their low efficiency and structural reliability, which are related to the occurrence of dynamic stall (Buchner *et. al*, 2018).

These technical limitations offer a potential research pathway that we intend to explore. Particularly, the characterization of the noise generated by an airfoil under dynamic stall has received little attention (Mayer *et. al*, 2020). Addressing the problem of dynamic stall noise will not only benefit the development of quieter wind turbines, but will also be relevant to urban air mobility. For instance, the new VTOL suite of services such as passenger air taxis and cargo drones calls for quieter engineering solutions. Thus, this research could provide directions for technical optimizations and modification of the relevant policies related to urban air mobility and wind farms. Interestingly, one of the first studies regarding dynamic stall noise is that from Nagarajan *et. al* (2006b), the main developer of the LES code we use in this work.

Working on ways to develop VAWT that can reach parity on energy output with traditional turbines while ensuring structural integrity, Fouest and Mulleners (2022) showed that light dynamic stall offers the best compromise between torque production and structural resilience. However, the nature of the pitching moment response during light dynamic stall can lead to negative aerodynamic damping, which results in stall flutter. Thus, the aerodynamic damping needs to be investigated carefully. In the future, we want to run simulations under motion kinematics that configure light stall regimes to explore this topic further. By changing the motion kinematics, we also seek to study thrust and propulsive efficiency of the airfoil. This is intimately related to the Knoller–Betz or

Katzmayr effect.

References

ABADI, M.; AGARWAL, A.; BARHAM, P.; BREVDO, E.; CHEN, Z.; CITRO, C.; CORRADO, G.S.; DAVIS, A.; DEAN, J.; DEVIN, M.; GHEMAWAT, S.; GOODFELLOW, I.; HARP, A.; IRVING, G.; ISARD, M.; JIA, Y.; JOZEFOWICZ, R.; KAISER, L.; KUDLUR, M.; LEVENBERG, J.; MANÉ, D.; MONGA, R.; MOORE, S.; MURRAY, D.; OLAH, C.; SCHUSTER, M.; SHLENS, J.; STEINER, B.; SUTSKEVER, I.; TALWAR, K.; TUCKER, P.; VANHOUCKE, V.; VASUDEVAN, V.; VIÉGAS, F.; VINYALS, O.; WARDEN, P.; WATTENBERG, M.; WICKE, M.; YU, Y. and ZHENG, X. TensorFlow: Large-scale machine learning on heterogeneous systems. 2015. Software available from tensorflow.org.

ACHILLE, A.; ROVERE, M. and SOATTO, S. Critical learning periods in deep neural networks. arXiv, 2019.

AHMED, S.E.; PAWAR, S.; SAN, O.; RASHEED, A.; ILIESCU, T. and NOACK, B.R. On closures for reduced order models—a spectrum of first-principle to machine-learned avenues. **Physics of Fluids**, vol. 33, n. 9, 091301, 2021.

ALVAREZ, C.A. and FRANKLIN, E.M. Role of transverse displacements in the formation of subaqueous barchan dunes. **Phys. Rev. Lett.**, vol. 121, 164503, 2018.

ALVAREZ, C.A. and FRANKLIN, E.M. Horns of subaqueous barchan dunes: A study at the grain scale. **Phys. Rev. E**, vol. 100, 042904, 2019.

ALVAREZ, C.A. and FRANKLIN, E.M. Shape evolution of numerically obtained subaqueous barchan dunes. **Phys. Rev. E**, vol. 101, 012905, 2020.

ALVAREZ, C.A. and FRANKLIN, E.M. Force distribution within a barchan dune. **Physics of Fluids**, vol. 33, n. 1, 013313, 2021.

ANDERSON, J.M.; STREITLIEN, K.; BARRETT, D.S. and TRIANTAFYLLOU, M.S. Oscillating foils of high propulsive efficiency. **Journal of Fluid Mechanics**, vol. 360, 41–72, 1998.

ANSELL, P.J. and MULLENERS, K. Multiscale vortex characteristics of dynamic stall from empirical mode decomposition. **AIAA Journal**, vol. 58, n. 2, 600–617, 2020.

ARIS, R. **Vectors, Tensors and the Basic Equations of Fluid Mechanics**. Dover Publications, 1989.

ASSIS, W.R. and FRANKLIN, E.M. Morphodynamics of barchan-barchan interactions investigated at the grain scale. **Journal of Geophysical Research: Earth Surface**, vol. 126, n. 8, e2021JF006237, 2021. E2021JF006237 2021JF006237.

BAIK, Y.S.; BERNAL, L.P.; GRANLUND, K. and OL, M.V. Unsteady force generation and vortex dynamics of pitching and plunging aerofoils. **Journal of Fluid Mechanics**, vol. 709, 37–68, 2012.

BEAHAN, J.J.; SHIH, C.; KROTHAPALLI, A.; KUMAR, R. and CHANDRASEKHARA, M.S. Compressible dynamic stall control using high momentum microjets. **Experiments in Fluids**, vol. 55, n. 9, 1813, 2014.

BEAM, R.M. and WARMING, R.F. An implicit factored scheme for the compressible Navier-Stokes equations. **AIAA Journal**, vol. 16, n. 4, 393–402, 1978.

BENTON, S.I. and VISBAL, M.R. High-frequency forcing to mitigate unsteady separation from a bursting separation bubble. **Physical Review Fluids**, vol. 3, 013907, 2018a.

BENTON, S.I. and VISBAL, M.R. Understanding abrupt leading edge separation as a mechanism for the onset of dynamic stall. In **2018 AIAA Aerospace Sciences Meeting**. 2018b.

BENTON, S.I. and VISBAL, M.R. Extending the reynolds number range of high-frequency control of dynamic stall. **AIAA Journal**, vol. 57, n. 7, 2675–2681, 2019a.

BENTON, S.I. and VISBAL, M.R. The onset of dynamic stall at a high, transitional reynolds number. **Journal of Fluid Mechanics**, vol. 861, 860–885, 2019b.

BENTON, S.I. and VISBAL, M.R. Effects of compressibility on dynamic-stall onset using large-eddy simulation. **AIAA Journal**, vol. 58, n. 3, 1194–1205, 2020.

BERNARDOS, L.; RICHEZ, F.; GLEIZE, V. and GEROLYMOS, G.A. Algebraic nonlocal transition modeling of laminar separation bubbles using k-w turbulence models. **AIAA Journal**, vol. 57, n. 2, 553–565, 2019.

BHASKARAN, R. and LELE, S.K. Large eddy simulation of free-stream turbulence effects on heat transfer to a high-pressure turbine cascade. **Journal of Turbulence**, , n. 11, N6, 2010.

BIRD, H. and RAMESH, K. Theoretical and computational studies of a rectangular finite wing oscillating in pitch and heave. In **6th European Conference on Computational Mechanics (ECCM 6) and 7th European Conference on Computational Fluid Dynamics (ECFD 7)**. 2018.

BIRD, H.J.A. and RAMESH, K. Unsteady lifting-line theory and the influence of wake vorticity on aerodynamic loads. **Theoretical and Computational Fluid Dynamics**, vol. 35, n. 5, 609–631, 2021.

BOTELHO, A.; AREZES, P.; BERNARDO, C.; DIAS, H. and PINTO, L.M.C. Effect of wind farm noise on local residents' decision to adopt mitigation measures. **International Journal of Environmental Research and Public Health**, vol. 14, n. 7, 2017.

BOURKE, M.C. Barchan dune asymmetry: Observations from mars and earth. **Icarus**, vol. 205, n. 1, 183–197, 2010. MRO/HiRISE Studies of Mars.

BOWLES, P.; COLEMAN, D.; CORKE, T. and THOMAS, F. Compressibility effects on aerodynamic damping during dynamic stall events. In **Vertical Flight Society's Annual Forum 68**, 68-2012-000347. 2012.

BOWLES, P.O., **Wind Tunnel Experiments on the Effect of Compressibility on the Attributes of Dynamic Stall**, PhD Thesis, University of Notre Dame, 2012.

BRUNTON, S.L. Applying machine learning to study fluid mechanics. **Acta Mechanica Sinica**, vol. 37, n. 12, 1718–1726, 2021.

BRUNTON, S.L.; NOACK, B.R. and KOUMOUTSAKOS, P. Machine learning for fluid mechanics. **Annual Review of Fluid Mechanics**, vol. 52, n. 1, 477–508, 2020.

BUCHNER, A.J.; BUCHMANN, N.; KILANY, K.; ATKINSON, C. and SORIA, J. Stereoscopic and tomographic piv of a pitching plate. **Experiments in Fluids**, vol. 52, n. 2, 299–314, 2012.

BUCHNER, A.J.; SORIA, J.; HONNERY, D. and SMITS, A.J. Dynamic stall in vertical axis wind turbines: scaling and topological considerations. **Journal of Fluid Mechanics**, vol. 841, 746–766, 2018.

CAI, S.; WANG, Z.; FUEST, F.; JEON, Y.J.; GRAY, C. and KARNIADAKIS, G.E. Flow over an espresso cup: inferring 3-d velocity and pressure fields from tomographic background oriented schlieren via physics-informed neural networks. **Journal of Fluid Mechanics**, vol. 915, A102, 2021. A102.

CARTA, F. A comparison of the pitching and plunging response of an oscillating airfoil. In **NASA Contractor Report 3172**. 1979.

CHANDRASEKHARA, M.S. Compressible dynamic stall vorticity flux control using a dynamic camber airfoil. **Sadhana**, vol. 32, n. 1, 93–102, 2007.

CHANDRASEKHARA, M.S. and CARR, L.W. Flow visualization studies of the Mach number effects on dynamic stall of an oscillating airfoil. **Journal of Aircraft**, vol. 27, n. 6, 516–522, 1990.

CHANDRASEKHARA, M.S.; CARR, L.W. and WILDER, M.C. Interferometric investigations of compressible dynamic stall over a transiently pitching airfoil. **AIAA Journal**, vol. 32, n. 3, 586–593, 1994.

CHARRU, F.; ANDREOTTI, B. and CLAUDIN, P. Sand ripples and dunes. **Annual Review of Fluid Mechanics**, vol. 45, n. 1, 469–493, 2013.

CHEN, J.; RAIOLA, M. and DISCETTI, S. Pressure from data-driven estimation of velocity fields using snapshot piv and fast probes. **Experimental Thermal and Fluid Science**, vol. 136, 110647, 2022.

CHOLLET, F. Building powerful image classification models using very little data. Keras Blog, 2016a.

CHOLLET, F. Xception: Deep learning with depthwise separable convolutions. arXiv, 2016b.

CHOLLET, F. *et. al.* Keras. `https://keras.io`, 2015.

CHOUDHURI, P.G. and KNIGHT, D.D. Effects of compressibility, pitch rate, and reynolds number on unsteady incipient leading-edge boundary layer separation over a pitching airfoil. **Journal of Fluid Mechanics**, vol. 308, 195–217, 1996.

CHOUDHURI, P.G.; KNIGHT, D.D. and VISBAL, M.R. Two-dimensional unsteady leading-edge separation on a pitching airfoil. **AIAA Journal**, vol. 32, n. 4, 673–681, 1994.

CHOWDHURY, N.E.; SHAKIB, M.A.; XU, F.; SALEHIN, S.; ISLAM, M.R. and BHUIYAN, A.A. Adverse environmental impacts of wind farm installations and alternative research pathways to their mitigation. **Cleaner Engineering and Technology**, vol. 7, 100415, 2022.

CLEVERT, D.A.; UNTERTHINER, T. and HOCHREITER, S. Fast and accurate deep network learning by exponential linear units (elus). arXiv, 2015.

COLEMAN, D.G.; THOMAS, F.O.; GORDEYEV, S. and CORKE, T.C. Parametric modal decomposition of dynamic stall. **AIAA Journal**, vol. 57, n. 1, 176–190, 2019.

COLOMBINI, M. A decade's investigation of the stability of erodible stream beds. **Journal of Fluid Mechanics**, vol. 756, 1–4, 2014.

CORKE, T.C. and THOMAS, F.O. Dynamic stall in pitching airfoils: Aerodynamic damping and compressibility effects. **Annual Review of Fluid Mechanics**, vol. 47, n. 1, 479–505, 2015.

CORNEJO MACEDA, G.Y.; LI, Y.; LUSSEYRAN, F.; MORZYŃSKI, M. and NOACK, B.R. Stabilization of the fluidic pinball with gradient-enriched machine learning control. **Journal of Fluid Mechanics**, vol. 917, A42, 2021. A42.

COSTES, M.; RICHEZ, F.; PAPE, A.L. and GAVÉRIAUX, R. Numerical investigation of three-dimensional effects during dynamic stall. **Aerospace Science and Technology**, vol. 47, 216 – 237, 2015.

DAI, K.; BERGOT, A.; LIANG, C.; XIANG, W.N. and HUANG, Z. Environmental issues associated with wind energy – a review. **Renewable Energy**, vol. 75, 911–921, 2015.

DARAKANANDA, D. and ELDREDGE, J.D. A versatile taxonomy of low-dimensional vortex models for unsteady aerodynamics. **Journal of Fluid Mechanics**, vol. 858, 917–948, 2019.

DEMO, N.; TEZZELE, M. and ROZZA, G. PyDMD: Python Dynamic Mode Decomposition. **The Journal of Open Source Software**, vol. 3, n. 22, 530, 2018.

DEPARDAY, J. and MULLENERS, K. Modeling the interplay between the shear layer and leading edge suction during dynamic stall. **Physics of Fluids**, vol. 31, n. 10, 107104, 2019.

DOLIGALSKI, T.L.; SMITH, C.R. and WALKER, J.D.A. Vortex interactions with walls. **Annual Review of Fluid Mechanics**, vol. 26, n. 1, 573–616, 1994.

DONG, Z.; CHEN, G.; HE, X.; HAN, Z. and WANG, X. Controlling blown sand along the highway crossing the taklimakan desert. **Journal of Arid Environments**, vol. 57, n. 3, 329–344, 2004.

DONG, Z.; WANG, X. and CHEN, G. Monitoring sand dune advance in the taklimakan desert. **Geomorphology**, vol. 35, n. 3, 219–231, 2000.

DOZAT, T. Incorporating nesterov momentum into adam. In **ICLR Workshop**. 2016.

DREWITT, A.L. and LANGSTON, R.H.W. Assessing the impacts of wind farms on birds. **Ibis**, vol. 148, n. s1, 29–42, 2006.

DUNNE, R.; SCHMID, P.J. and MCKEON, B.J. Analysis of flow timescales on a periodically pitching/surging airfoil. **AIAA Journal**, vol. 54, n. 11, 3421–3433, 2016.

DURAISAMY, K.; IACCARINO, G. and XIAO, H. Turbulence modeling in the age of data. **Annual Review of Fluid Mechanics**, vol. 51, n. 1, 357–377, 2019.

EIVAZI, H.; VEISI, H.; NADERI, M.H. and ESFAHANIAN, V. Deep neural networks for nonlinear model order reduction of unsteady flows. **Physics of Fluids**, vol. 32, n. 10, 105104, 2020.

EKATERINARIS, J.A.; CHANDRASEKHARA, M.S. and PLATZER, M.F. Analysis of low reynolds number airfoil flows. **Journal of Aircraft**, vol. 32, n. 3, 625–630, 1995.

EKATERINARIS, J.A. and PLATZER, M.F. Computational prediction of airfoil dynamic stall. **Progress in Aerospace Sciences**, vol. 33, n. 11, 759 – 846, 1998.

ELDREDGE, J.; WANG, C. and OL, M. **A Computational Study of a Canonical Pitch-Up, Pitch-Down Wing Maneuver**. 2009.

ELDREDGE, J.D. and JONES, A.R. Leading-edge vortices: Mechanics and modeling. **Annual Review of Fluid Mechanics**, vol. 51, n. 1, 75–104, 2019.

ELFERING, K.H. and GRANLUND, K.O. Lift equivalence and cancellation for airfoil surge–pitch–plunge oscillations. **AIAA Journal**, vol. 58, n. 11, 4629–4643, 2020.

ERICSSON, L.E. Challenges in high-alpha vehicle dynamics. **Progress in Aerospace Sciences**, vol. 31, n. 4, 291–334, 1995.

EVANS, W.T. and MORT, K.W. Analysis of computed flow parameters for a set of sudden stalls in low speed two-dimensional flow. In **NACA Tech. Rep TN D-85**. 1959.

FALLER, W.; SCHRECK, S. and LUTTGES, M. Real-time prediction and control of three-dimensional unsteady separated flow fields using neural networks. In **32nd Aerospace Sciences Meeting and Exhibit**. 1994.

FOUEST, S.L.; DEPARDAY, J. and MULLENERS, K. The dynamics and timescales of static stall. **Journal of Fluids and Structures**, vol. 104, 103304, 2021.

FOUEST, S.L. and MULLENERS, K. The dynamic stall dilemma for vertical-axis wind turbines. arXiv, 2022.

FUKAMI, K.; FUKAGATA, K. and TAIRA, K. Assessment of supervised machine learning methods for fluid flows. **Theoretical and Computational Fluid Dynamics**, vol. 34, n. 4, 497–519, 2020.

FUKAMI, K.; HASEGAWA, K.; NAKAMURA, T.; MORIMOTO, M. and FUKAGATA, K. Model order reduction with neural networks: Application to laminar and turbulent flows. **SN Computer Science**, vol. 2, n. 6, 467, 2021.

GARDNER, A.; RICHTER, K.; MAI, H. and NEUHAUS, D. Experimental investigation of high-pressure pulsed blowing for dynamic stall control. **CEAS Aeronaut J**, vol. 5, n. 2, 185–198, 2014a.

GARDNER, A.D.; KLEIN, C.; SACHS, W.E.; HENNE, U.; MAI, H. and RICHTER, K. Investigation of three-dimensional dynamic stall on an airfoil using fast-response pressure-sensitive paint. **Experiments in Fluids**, vol. 55, n. 1807, 1–14, 2014b.

GAVISH, M. and DONOHO, D.L. The optimal hard threshold for singular values is $4/\sqrt{3}$. **IEEE Transactions on Information Theory**, vol. 60, n. 8, 5040–5053, 2014.

GENDRICH, C.P.; KOOCHESFAHANI, M.M. and VISBAL, M.R. Effects of Initial Acceleration on the Flow Field Development Around Rapidly Pitching Airfoils. **Journal of Fluids Engineering**, vol. 117, n. 1, 45–49, 1995.

GLOROT, X. and BENGIO, Y. Understanding the difficulty of training deep feedforward neural networks. In **Proceedings of the Thirteenth International Conference**

on Artificial Intelligence and Statistics, vol. 9 of *Proceedings of Machine Learning Research*, pp. 249–256. PMLR, 2010.

GOODFELLOW, I.; POUGET-ABADIE, J.; MIRZA, M.; XU, B.; WARDE-FARLEY, D.; OZAIR, S.; COURVILLE, A. and BENGIO, Y. Generative adversarial nets. In **Advances in Neural Information Processing Systems**, vol. 27. Curran Associates, Inc., 2014.

GRANLUND, K.O.; OL, M.V. and BERNAL, L.P. Unsteady pitching flat plates. **Journal of Fluid Mechanics**, vol. 733, R5, 2013. R5.

GREENBERG, J.M. Airfoil in sinusoidal motion in a pulsating stream. In **NACA TN 1326**. 1947.

GREENBLATT, D. and WYGNANSKI, I. Dynamic stall control by periodic excitation, part 1: Naca 0015 parametric study. **Journal of Aircraft**, vol. 38, n. 3, 430–438, 2001.

GUASTONI, L.; GÜEMES, A.; IANIRO, A.; DISCETTI, S.; SCHLATTER, P.; AZIZPOUR, H. and VINUESA, R. Convolutional-network models to predict wall-bounded turbulence from wall quantities. **Journal of Fluid Mechanics**, vol. 928, A27, 2021. A27.

GUI, J.; SUN, Z.; WEN, Y.; TAO, D. and YE, J. A review on generative adversarial networks: Algorithms, theory, and applications. **IEEE Transactions on Knowledge and Data Engineering**, pp. 1–1, 2021.

GUPTA, R. and ANSELL, P.J. Unsteady flow physics of airfoil dynamic stall. **AIAA Journal**, vol. 57, n. 1, 165–175, 2019.

GUPTA, R. and ANSELL, P.J. Flow evolution and unsteady spectra of dynamic stall at transitional reynolds numbers. **AIAA Journal**, vol. 58, n. 8, 3272–3285, 2020.

GURSUL, I. and CLEAVER, D. Plunging oscillations of airfoils and wings: Progress, opportunities, and challenges. **AIAA Journal**, vol. 57, n. 9, 3648–3665, 2019.

GÜEMES, A.; DISCETTI, S.; IANIRO, A.; SIRMACEK, B.; AZIZPOUR, H. and VINUESA, R. From coarse wall measurements to turbulent velocity fields through deep learning. **Physics of Fluids**, vol. 33, n. 7, 075121, 2021.

HA, C.M. Neural networks approach to aiaa aircraft control design challenge. **Journal of Guidance, Control, and Dynamics**, vol. 18, n. 4, 731–739, 1995.

HE, G.; DEPARDAY, J.; SIEGEL, L.; HENNING, A. and MULLENERS, K. Stall delay and leading-edge suction for a pitching airfoil with trailing-edge flap. **AIAA Journal**, vol. 58, n. 12, 5146–5155, 2020.

HE, K.; ZHANG, X.; REN, S. and SUN, J. Deep residual learning for image recognition. In **2016 IEEE Conference on Computer Vision and Pattern Recognition (CVPR)**, pp. 770–778. 2016.

HERSEN, P.; DOUADY, S. and ANDREOTTI, B. Relevant length scale of barchan dunes. **Phys. Rev. Lett.**, vol. 89, 264301, 2002.

HIRATO, Y.; SHEN, M.; GOPALARATHNAM, A. and EDWARDS, J.R. Flow criticality governs leading-edge-vortex initiation on finite wings in unsteady flow. **Journal of Fluid Mechanics**, vol. 910, A1, 2021.

JIN, X.; CHENG, P.; CHEN, W.L. and LI, H. Prediction model of velocity field around circular cylinder over various reynolds numbers by fusion convolutional neural networks based on pressure on the cylinder. **Physics of Fluids**, vol. 30, n. 4, 047105, 2018.

JIN, X.; LAIMA, S.; CHEN, W.L. and LI, H. Time-resolved reconstruction of flow field around a circular cylinder by recurrent neural networks based on non-time-resolved particle image velocimetry measurements. **Experiments in Fluids**, vol. 61, n. 4, 114, 2020.

JONES, A.R. and CETINER, O. Overview of unsteady aerodynamic response of rigid wings in gust encounters. **AIAA Journal**, vol. 59, n. 2, 731–736, 2021.

JOVANOVIć, M.R.; SCHMID, P.J. and NICHOLS, J.W. Sparsity-promoting dynamic mode decomposition. **Physics of Fluids**, vol. 26, n. 2, 024103, 2014.

JUMPER, E.J.; SCHRECK, S.J. and DIMMICK, R.L. Lift-curve characteristics for an airfoil pitching at constant rate. **Journal of Aircraft**, vol. 24, n. 10, 680–687, 1987.

KARANIKAS, N.; STEELE, S.; BRUSCHI, K.; ROBERTSON, C.; KASS, J.; POPOVICH, A. and MACFADYEN, C. Occupational health hazards and risks in the wind industry. **Energy Reports**, vol. 7, 3750–3759, 2021.

KARIM, M.A. and ACHARYA, M. Suppression of dynamic-stall vortices over pitching airfoils by leading-edge suction. **AIAA Journal**, vol. 32, n. 8, 1647–1655, 1994.

KAUFMANN, K.; MERZ, C.B. and GARDNER, A.D. Dynamic stall simulations on a pitching finite wing. **Journal of Aircraft**, vol. 54, n. 4, 1303–1316, 2017.

KAWTHAR-ALI, M. and ACHARYA, M. Artificial neural networks for suppression of the dynamic-stall vortex over pitching airfoils. In **34th Aerospace Sciences Meeting and Exhibit**. 1996.

KIDANEMARIAM, A.G. and UHLMANN, M. Direct numerical simulation of pattern formation in subaqueous sediment. **Journal of Fluid Mechanics**, vol. 750, R2, 2014. R2.

KIDANEMARIAM, A.G. and UHLMANN, M. Formation of sediment patterns in channel flow: minimal unstable systems and their temporal evolution. **Journal of Fluid Mechanics**, vol. 818, 716–743, 2017.

KINGMA, D.P. and BA, J. Adam: A method for stochastic optimization. In **ICLR**. 2015.

KOCHKOV, D.; SMITH, J.A.; ALIEVA, A.; WANG, Q.; BRENNER, M.P. and HOYER, S. Machine learning-accelerated computational fluid dynamics. **Proceedings of the National Academy of Sciences**, vol. 118, n. 21, e2101784118, 2021.

KOU, J. and ZHANG, W. Data-driven modeling for unsteady aerodynamics and aeroelasticity. **Progress in Aerospace Sciences**, vol. 125, 100725, 2021.

KRIZHEVSKY, A.; SUTSKEVER, I. and HINTON, G.E. Imagenet classification with deep convolutional neural networks. In **Advances in Neural Information Processing Systems**, vol. 25. Curran Associates, Inc., 2012.

KUTZ, J.N. Deep learning in fluid dynamics. **Journal of Fluid Mechanics**, vol. 814, 1–4, 2017.

KUTZ, J.N.; FU, X. and BRUNTON, S.L. Multiresolution dynamic mode decomposition. **SIAM Journal on Applied Dynamical Systems**, vol. 15, n. 2, 713–735, 2016.

LECUN, Y.; BOTTOU, L.; BENGIO, Y. and HAFFNER, P. Gradient-based learning applied to document recognition. **Proceedings of the IEEE**, vol. 86, n. 11, 2278–2324, 1998.

LEE, H.; SIMONE, N.; SU, Y.; ZHU, Y.; RIBEIRO, B.L.R.; FRANCK, J.A. and BREUER, K. Leading edge vortex formation and wake trajectory: Synthesizing measurements, analysis, and machine learning. **Phys. Rev. Fluids**, vol. 7, 074704, 2022.

LEE, T. and GERONTAKOS, P. Investigation of flow over an oscillating airfoil. **Journal of Fluid Mechanics**, vol. 512, 313–341, 2004.

LELE, S.K. Compact finite difference schemes with spectral-like resolution. **Journal of Computational Physics**, vol. 103, n. 1, 16 – 42, 1992.

LI, D.; KOMPERDA, J.; GHIASI, Z.; PEYVAN, A. and MASHAYEK, F. Compressibility effects on the transition to turbulence in a spatially developing plane free shear layer. **Theoretical and Computational Fluid Dynamics**, vol. 33, n. 6, 577–602, 2019.

LING, J.; KURZAWSKI, A. and TEMPLETON, J. Reynolds averaged turbulence modelling using deep neural networks with embedded invariance. **Journal of Fluid Mechanics**, vol. 807, 155–166, 2016.

LINSE, D.J. and STENGEL, R.F. Identification of aerodynamic coefficients using computational neural networks. **Journal of Guidance, Control, and Dynamics**, vol. 16, n. 6, 1018–1025, 1993.

LIU, Y.; LU, Y.; WANG, Y.; SUN, D.; DENG, L.; WANG, F. and LEI, Y. A cnn-based shock detection method in flow visualization. **Computers Fluids**, vol. 184, 1–9, 2019.

LOMBARDI, A.J.; BOWLES, P.O. and CORKE, T.C. Closed-loop dynamic stall control using a plasma actuator. **AIAA Journal**, vol. 51, n. 5, 1130–1141, 2013.

LONG, J.; SHELHAMER, E. and DARRELL, T. Fully convolutional networks for semantic segmentation. In **2015 IEEE Conference on Computer Vision and Pattern Recognition (CVPR)**, pp. 3431–3440. 2015.

LORBER, P.F. and CARTA, F.O. Airfoil dynamic stall at constant pitch rate and high reynolds number. **Journal of Aircraft**, vol. 25, n. 6, 548–556, 1988.

LUI, H.F.S. and WOLF, W.R. Construction of reduced-order models for fluid flows using deep feedforward neural networks. **Journal of Fluid Mechanics**, vol. 872, 963–994, 2019.

LUMLEY, J.L. The structure of inhomogeneous turbulent flows. **Atmospheric turbulence and radio wave propagation**, pp. 166–178, 1967.

MALLIK, W. and RAVEH, D.E. Aerodynamic damping investigations of light dynamic stall on a pitching airfoil via modal analysis. **Journal of Fluids and Structures**, vol. 98, 103111, 2020.

MANCINI, P.; MANAR, F.; GRANLUND, K.; OL, M.V. and JONES, A.R. Unsteady aerodynamic characteristics of a translating rigid wing at low reynolds number. **Physics of Fluids**, vol. 27, n. 12, 123102, 2015.

MASSA, L.; KUMAR, R. and RAVINDRAN, P. Dynamic mode decomposition analysis of detonation waves. **Physics of Fluids**, vol. 24, n. 6, 066101, 2012.

MATHEW, J.; LECHNER, R.; FOYSI, H.; SESTERHENN, J. and FRIEDRICH, R. An explicit filtering method for large eddy simulation of compressible flows. **Physics of Fluids**, vol. 15, n. 8, 2279–2289, 2003.

MAULIK, R.; SAN, O.; RASHEED, A. and VEDULA, P. Subgrid modelling for two-dimensional turbulence using neural networks. **Journal of Fluid Mechanics**, vol. 858, 122–144, 2019.

MAYER, Y.; ZANG, B. and AZARPEYVAND, M. A preliminary study of dynamic stall noise. In **AIAA Scitech 2020 Forum**. 2020.

MCALISTER, K.W. and CARR, L.W. Water tunnel visualizations of dynamic stall. **Journal of Fluids Engineering**, vol. 101, 376–380, 1979.

MCCROSKEY, W. The phenomenon of dynamic stall. In **NASA Tech. Report TM-81264**. 1981.

MCGOWAN, G.; GOPALARATHNAM, A.; OL, M.; EDWARDS, J. and FREDBERG, D. Computation vs. experiment for high-frequency low-reynolds number airfoil pitch and plunge. In **46th AIAA Aerospace Sciences Meeting and Exhibit**. 2008.

MCGOWAN, G.Z.; GRANLUND, K.; OL, M.V.; GOPALARATHNAM, A. and EDWARDS, J.R. Investigations of lift-based pitch-plunge equivalence for airfoils at low reynolds numbers. **AIAA Journal**, vol. 49, n. 7, 1511–1524, 2011.

MELIUS, M.; CAL, R.B. and MULLENERS, K. Dynamic stall of an experimental wind turbine blade. **Physics of Fluids**, vol. 28, n. 3, 034103, 2016.

MENDIBLE, A.; BRUNTON, S.L.; ARAVKIN, A.Y.; LOWRIE, W. and KUTZ, J.N. Dimensionality reduction and reduced-order modeling for traveling wave physics. **Theoretical and Computational Fluid Dynamics**, vol. 34, n. 4, 385–400, 2020.

MIOTTO, R.; WOLF, W.; GAITONDE, D. and VISBAL, M. Analysis of the onset and evolution of a dynamic stall vortex on a periodic plunging aerofoil. **Journal of Fluid Mechanics**, vol. 938, A24, 2022. A24.

MIOTTO, R.F. and WOLF, W. Compressibility effects on the onset of dynamic stall in a periodic plunging airfoil. In **18th Brazilian Congress of Thermal Sciences and Engineering**. 2020.

MIOTTO, R.F.; WOLF, W.; DE SANTANA, L.D. and VENNER, C.H. Application of amiet's theory for noise prediction of general airfoil profiles subjected to spanwise-varying inflow conditions. In **2018 AIAA/CEAS Aeroacoustics Conference**. 2018a.

MIOTTO, R.F.; WOLF, W.; GAITONDE, D. and VISBAL, M.R. Pitch-plunge equivalence in dynamic stall of ramp motion airfoils. In **AIAA AVIATION 2021 FORUM**. 2021a.

MIOTTO, R.F.; WOLF, W.; GAITONDE, D.V. and VISBAL, M. An investigation of compressibility effects on dynamic stall for a periodic plunging airfoil at moderate reynolds number. In **AIAA Scitech 2021 Forum**. 2021b.

MIOTTO, R.F.; WOLF, W.R. and DE SANTANA, L.D. Leading-edge noise prediction of general airfoil profiles with spanwise-varying inflow conditions. **AIAA Journal**, vol. 56, n. 5, 1711–1716, 2018b.

MOHAN, A.T.; GAITONDE, D.V. and VISBAL, M.R. Model reduction and analysis of deep dynamic stall on a plunging airfoil. **Computers & Fluids**, vol. 129, 1 – 19, 2016.

MONAZZAM, M.R.; ZAKERIAN, S.A.; KAZEMI, Z.; EBRAHIMI, M.H.; GHALJAHI, M.; MEHRI, A.; AFKHAMINIA, F. and ABBASI, M. Investigation of occupational noise annoyance in a wind turbine power plant. **Journal of Low Frequency Noise, Vibration and Active Control**, vol. 38, n. 2, 798–807, 2019.

MULD, T.W.; EFRAIMSSON, G. and HENNINGSON, D.S. Flow structures around a high-speed train extracted using proper orthogonal decomposition and dynamic mode decomposition. **Computers & Fluids**, vol. 57, 87–97, 2012.

MULLENERS, K. and RAFFEL, M. The onset of dynamic stall revisited. **Experiments in Fluids**, vol. 52, 779–793, 2012.

MÜLLER-VAHL, H.F.; NAYERI, C.N.; PASCHEREIT, C.O. and GREENBLATT, D. Dynamic stall control via adaptive blowing. **Renewable Energy**, vol. 97, 47 – 64, 2016.

NAGARAJAN, S., **Leading Edge Effects in Bypass Transition**, PhD Thesis, Stanford University, 2004.

NAGARAJAN, S.; HAHN, S. and LELE, S. Prediction of sound generated by a pitching airfoil: A comparison of rans and les. In **12th AIAA/CEAS Aeroacoustics Conference**. 2006a.

NAGARAJAN, S.; HAHN, S. and LELE, S. **Prediction of Sound Generated by a Pitching Airfoil: A Comparison of RANS and LES**. 2006b.

NAGARAJAN, S.; LELE, S.K. and FERZIGER, J.H. A robust high-order compact method for large eddy simulation. **Journal of Computational Physics**, vol. 191, n. 2, 392–419, 2003.

NARSIPUR, S.; HOSANGADI, P.; GOPALARATHNAM, A. and EDWARDS, J.R. Variation of leading-edge suction during stall for unsteady aerofoil motions. **Journal of Fluid Mechanics**, vol. 900, A25, 2020.

NOGUEIRA, P.A.S.; SIROTTO, J.R.L.N.; MIOTTO, R.F.; CAVALIERI, A.V.G.; CORDIOLI, J.A. and WOLF, W.R. Acoustic radiation of subsonic jets in the vicinity of an inclined flat plate. **The Journal of the Acoustical Society of America**, vol. 146, n. 1, 50–59, 2019.

OBAYASHI, W.; AONO, H.; TATSUKAWA, T. and FUJII, K. Feature extraction of fields of fluid dynamics data using sparse convolutional autoencoder. **AIP Advances**, vol. 11, n. 10, 105211, 2021.

OL, M.; ALTMAN, A.; ELDREDGE, J.; GARMANN, D. and LIAN, Y. Résumé of the AIAA FDTC low reynolds number discussion group's canonical cases. In **48th AIAA Aerospace Sciences Meeting**. 2010.

OL, M.; DONG, H. and WEBB, C. Motion kinematics vs. angle of attack effects in high-frequency airfoil pitch/plunge. In **38th Fluid Dynamics Conference and Exhibit**. 2008.

OL, M.V.; ELDREDGE, J.D. and WANG, C. High-amplitude pitch of a flat plate: An abstraction of perching and flapping. **International Journal of Micro Air Vehicles**, vol. 1, n. 3, 203–216, 2009.

PANDEY, S.; SCHUMACHER, J. and SREENIVASAN, K.R. A perspective on machine learning in turbulent flows. **Journal of Turbulence**, vol. 21, n. 9-10, 567–584, 2020.

PRANDTL, L. Über flüssigkeitsbewegung bei sehr kleiner Reibung. **Intern. Math. Kongr.**, vol. 2, 484–491, 1904.

PRANGEMEIER, T.; RIVAL, D. and TROPEA, C. The manipulation of trailing-edge vortices for an airfoil in plunging motion. **Journal of Fluids and Structures**, vol. 26, n. 2, 193–204, 2010.

PRUSKI, B.J. and BOWERSOX, R.D.W. Leading-edge flow structure of a dynamically pitching NACA 0012 airfoil. **AIAA Journal**, vol. 51, n. 5, 1042–1053, 2013.

RABAULT, J.; REN, F.; ZHANG, W.; TANG, H. and XU, H. Deep reinforcement learning in fluid mechanics: A promising method for both active flow control and shape optimization. **Journal of Hydrodynamics**, vol. 32, n. 2, 234–246, 2020.

RAIBAUDO, C.; ZHONG, P.; NOACK, B.R. and MARTINUZZI, R.J. Machine learning strategies applied to the control of a fluidic pinball. **Physics of Fluids**, vol. 32, n. 1, 015108, 2020.

RAISSI, M.; PERDIKARIS, P. and KARNIADAKIS, G. Physics-informed neural networks: A deep learning framework for solving forward and inverse problems involving nonlinear partial differential equations. **Journal of Computational Physics**, vol. 378, 686–707, 2019.

RAISSI, M.; YAZDANI, A. and KARNIADAKIS, G.E. Hidden fluid mechanics: Learning velocity and pressure fields from flow visualizations. **Science**, vol. 367, n. 6481, 1026–1030, 2020.

RAMESH, K. On the leading-edge suction and stagnation-point location in unsteady flows past thin aerofoils. **Journal of Fluid Mechanics**, vol. 886, A13, 2020. A13.

RAMESH, K.; GOPALARATHNAM, A.; GRANLUND, K.; OL, M.V. and EDWARDS, J.R. Discrete-vortex method with novel shedding criterion for unsteady aerofoil flows with intermittent leading-edge vortex shedding. **Journal of Fluid Mechanics**, vol. 751, 500–538, 2014.

RAMESH, K.; GRANLUND, K.; OL, M.V.; GOPALARATHNAM, A. and EDWARDS, J.R. Leading-edge flow criticality as a governing factor in leading-edge vortex initiation in unsteady airfoil flows. **Theoretical and Computational Fluid Dynamics**, vol. 32, n. 2, 109–136, 2018.

RAMOS, B.L.O., **High-fidelity simulation and flow control of a plunging airfoil under deep dynamic stall**, PhD Thesis, University of Campinas, 2019.

RAMOS, B.L.O.; WOLF, W.R.; YEH, C.A. and TAIRA, K. Active flow control for drag reduction of a plunging airfoil under deep dynamic stall. **Physical Review Fluids**, vol. 4, 074603, 2019.

RIVAL, D. and TROPEA, C. Characteristics of pitching and plunging airfoils under dynamic-stall conditions. **Journal of Aircraft**, vol. 47, n. 1, 80–86, 2010.

RONNEBERGER, O.; FISCHER, P. and BROX, T. U-net: Convolutional networks for biomedical image segmentation. In **Medical Image Computing and Computer-Assisted Intervention – MICCAI 2015**, pp. 234–241. Springer International Publishing, Cham, 2015. ISBN 978-3-319-24574-4.

ROWLEY, C.W. and DAWSON, S.T. Model reduction for flow analysis and control. **Annual Review of Fluid Mechanics**, vol. 49, n. 1, 387–417, 2017.

RUNYON, K.; BRIDGES, N.; AYOUB, F.; NEWMAN, C. and QUADE, J. An integrated model for dune morphology and sand fluxes on mars. **Earth and Planetary Science Letters**, vol. 457, 204–212, 2017.

SANGWAN, J.; SENGUPTA, T.K. and SUCHANDRA, P. Investigation of compressibility effects on dynamic stall of pitching airfoil. **Physics of Fluids**, vol. 29, n. 7, 076104, 2017.

SAUERMANN, G.; ROGNON, P.; POLIAKOV, A. and HERRMANN, H. The shape of the barchan dunes of southern morocco. **Geomorphology**, vol. 36, n. 1, 47–62, 2000.

SCHARNOWSKI, S. and KÄHLER, C.J. On the loss-of-correlation due to piv image noise. **Experiments in Fluids**, vol. 57, n. 7, 119, 2016.

SCHATZ, V.; TSOAR, H.; EDGETT, K.S.; PARTELI, E.J.R. and HERRMANN, H.J. Evidence for indurated sand dunes in the martian north polar region. **Journal of Geophysical Research: Planets**, vol. 111, n. E4, 2006.

SCHMID, P.J. Dynamic mode decomposition of numerical and experimental data. **Journal of Fluid Mechanics**, vol. 656, 5–28, 2010.

SCHRECK, S.J.; FALLER, W.E. and LUTTGES, M.W. Neural network prediction of three-dimensional unsteady separated flowfields. **Journal of Aircraft**, vol. 32, n. 1, 178–185, 1995.

SCHRECK, S.J.; FALLER, W.E. and ROBINSON, M.C. Unsteady separation processes and leading edge vortex precursors: Pitch rate and reynolds number influences. **Journal of Aircraft**, vol. 39, n. 5, 868–875, 2002.

SEDKY, G.; JONES, A.R. and LAGOR, F.D. Lift regulation during transverse gust encounters using a modified goman–khrabrov model. **AIAA Journal**, vol. 58, n. 9, 3788–3798, 2020a.

SEDKY, G.; LAGOR, F. and JONES, A.R. The unsteady aerodynamics of a transverse wing-gust encounter with closed-loop pitch control. In **AIAA Scitech 2020 Forum**. 2020b.

SEENA, A. and SUNG, H.J. Dynamic mode decomposition of turbulent cavity flows for self-sustained oscillations. **International Journal of Heat and Fluid Flow**, vol. 32, n. 6, 1098 – 1110, 2011.

SEMERARO, O.; BELLANI, G. and LUNDELL, F. Analysis of time-resolved PIV measurements of a confined turbulent jet using POD and Koopman modes. **Experiments in Fluids**, vol. 53, n. 5, 1203–1220, 2012.

SHAFFER, J.A. and BUHL, D.A. Effects of wind-energy facilities on breeding grassland bird distributions. **Conservation Biology**, vol. 30, n. 1, 59–71, 2016.

SHIH, C.; LOURENCO, L.M. and KROTHAPALLI, A. Investigation of flow at leading and trailing edges of pitching-up airfoil. **AIAA Journal**, vol. 33, n. 8, 1369–1376, 1995.

SHORTEN, C. and KHOSHGOFTAAR, T.M. A survey on image data augmentation for deep learning. **Journal of Big Data**, vol. 6, n. 1, 60, 2019.

SHYY, W.; LIAN, Y.; TANG, J.; VIIERU, D. and LIU, H. **Aerodynamics of Low Reynolds Number Flyers**. Cambridge Aerospace Series. Cambridge University Press, 2007.

SIMONYAN, K. and ZISSERMAN, A. Very deep convolutional networks for large-scale image recognition. In **ICLR**. 2015.

STRICKLAND, J.H. and GRAHAM, G.M. Force coefficients for a NACA 0015 airfoil undergoing constant pitch-rate motions. **AIAA Journal**, vol. 25, n. 4, 622–624, 1987.

STROFER, C.M.; WU, J.L.; XIAO, H. and PATERSON, E. Data-driven, physics-based feature extraction from fluid flow fields using convolutional neural networks. **Communications in Computational Physics**, vol. 25, n. 3, 2019.

SYNGE, J.L. and SCHILD, A. **Tensor calculus**. Dover Publications, 1978.

SZEGEDY, C.; LIU, W.; JIA, Y.; SERMANET, P.; REED, S.; ANGUELOV, D.; ERHAN, D.; VANHOUCKE, V. and RABINOVICH, A. Going deeper with convolutions. In **2015 IEEE Conference on Computer Vision and Pattern Recognition (CVPR)**, pp. 1–9. 2015.

SZEGEDY, C.; VANHOUCKE, V.; IOFFE, S.; SHLENS, J. and WOJNA, Z. Rethinking the inception architecture for computer vision. In **2016 IEEE Conference on Computer Vision and Pattern Recognition (CVPR)**, pp. 2818–2826. 2016.

TAHA, H. and REZAEI, A.S. Viscous extension of potential-flow unsteady aerodynamics: the lift frequency response problem. **Journal of Fluid Mechanics**, vol. 868, 141–175, 2019.

TAHA, H.E. and REZAEI, A.S. State-space modeling of viscous unsteady aerodynamic loads. **AIAA Journal**, vol. 60, n. 4, 2251–2265, 2022.

TAIRA, K.; BRUNTON, S.L.; DAWSON, S.T.M.; ROWLEY, C.W.; COLONIUS, T.; MCKEON, B.J.; SCHMIDT, O.T.; GORDEYEV, S.; THEOFILIS, V. and UKEILEY, L.S. Modal analysis of fluid flows: An overview. **AIAA Journal**, vol. 55, n. 12, 4013–4041, 2017.

TAIRA, K.; HEMATI, M.S.; BRUNTON, S.L.; SUN, Y.; DURAISAMY, K.; BAGHERI, S.; DAWSON, S.T.M. and YEH, C.A. Modal analysis of fluid flows: Applications and outlook. **AIAA Journal**, vol. 58, n. 3, 998–1022, 2020.

TAN, M. and LE, Q. EfficientNet: Rethinking model scaling for convolutional neural networks. In **Proceedings of the 36th International Conference on Machine Learning**, vol. 97 of *Proceedings of Machine Learning Research*, pp. 6105–6114. PMLR, 2019.

TRUESDELL, C. **The Kinematics of Vorticity**. Indiana University publications: Science series. Indiana University Press, 1954.

TU, J.H.; ROWLEY, C.W.; LUCHTENBURG, D.M.; BRUNTON, S.L. and KUTZ, J.N. On dynamic mode decomposition: Theory and applications. **Journal of Computational Dynamics**, vol. 1, n. 2, 391–421, 2014.

VAN DER KINDERE, J.W.; LASKARI, A.; GANAPATHISUBRAMANI, B. and DE KAT, R. Pressure from 2D snapshot PIV. **Experiments in Fluids**, vol. 60, n. 2, 32, 2019.

VAN DOMMELEN, L. and SHEN, S. The spontaneous generation of the singularity in a separating laminar boundary layer. **Journal of Computational Physics**, vol. 38, n. 2, 125 – 140, 1980.

VAN GENT, P.L.; MICHAELIS, D.; VAN OUDHEUSDEN, B.W.; WEISS, P.É.; DE KAT, R.; LASKARI, A.; JEON, Y.J.; DAVID, L.; SCHANZ, D.; HUHN, F.; GESEMANN, S.; NOVARA, M.; MCPHADEN, C.; NEETESON, N.J.; RIVAL, D.E.; SCHNEIDERS, J.F.G. and SCHRIJER, F.F.J. Comparative assessment of pressure field reconstructions from particle image velocimetry measurements and lagrangian particle tracking. **Experiments in Fluids**, vol. 58, n. 4, 33, 2017.

VAN OUDHEUSDEN, B.W. PIV-based pressure measurement. **Measurement Science and Technology**, vol. 24, n. 3, 032001, 2013.

VINOKUR, M. Conservation equations of gasdynamics in curvilinear coordinate systems. **Journal of Computational Physics**, vol. 14, n. 2, 105–125, 1974.

VISBAL, M.R. High-fidelity simulation of transitional flows past a plunging airfoil. **AIAA Journal**, vol. 47, n. 11, 2685–2697, 2009.

VISBAL, M.R. Numerical investigation of deep dynamic stall of a plunging airfoil. **AIAA Journal**, vol. 49, n. 10, 2152–2170, 2011.

VISBAL, M.R. Analysis of the onset of dynamic stall using high-fidelity large-eddy simulations. In **52nd Aerospace Sciences Meeting**. 2014.

VISBAL, M.R. and GAITONDE, D.V. On the use of higher-order finite-difference schemes on curvilinear and deforming meshes. **Journal of Computational Physics**, vol. 181, n. 1, 155 – 185, 2002.

VISBAL, M.R. and GARMANN, D.J. Analysis of dynamic stall on a pitching airfoil using high-fidelity large-eddy simulations. **AIAA Journal**, vol. 56, n. 1, 46–63, 2018.

VISBAL, M.R. and GARMANN, D.J. Pitch/plunge equivalence for dynamic stall of unswept finite wings. **AIAA Journal**, pp. 1–11, 2022.

VISBAL, M.R. and SHANG, J.S. Investigation of the flow structure around a rapidly pitching airfoil. **AIAA Journal**, vol. 27, n. 8, 1044–1051, 1989.

WANG, H.; LIU, Y. and WANG, S. Dense velocity reconstruction from particle image velocimetry/particle tracking velocimetry using a physics-informed neural network. **Physics of Fluids**, vol. 34, n. 1, 017116, 2022.

WANG, M. and DENG, W. Deep visual domain adaptation: A survey. **Neurocomputing**, vol. 312, 135–153, 2018.

WANG, R.; KASHINATH, K.; MUSTAFA, M.; ALBERT, A. and YU, R. Towards physics-informed deep learning for turbulent flow prediction. arXiv, 2019.

WENZEL, J.L. and DE MORAESFRANKLIN, E. Velocity fields and particle trajectories for bed load over subaqueous barchan dunes. **Granular Matter**, vol. 21, n. 3, 75, 2019.

WILLARD, J.; JIA, X.; XU, S.; STEINBACH, M. and KUMAR, V. Integrating scientific knowledge with machine learning for engineering and environmental systems. **ACM Comput. Surv.**, 2022.

WRAY, A.A. Very low storage time advancement schemes. In **NASA Technical Report 1999-209349**. 1986.

WU, J.L.; XIAO, H. and PATERSON, E. Physics-informed machine learning approach for augmenting turbulence models: A comprehensive framework. **Phys. Rev. Fluids**, vol. 3, 074602, 2018.

WU, J.Z.; MA, H.Y. and ZHOU, M.D. **Vorticity and Vortex Dynamics**. Springer, 2006.

WU, X.; ZHANG, X.; TIAN, X.; LI, X. and LU, W. A review on fluid dynamics of flapping foils. **Ocean Engineering**, vol. 195, 106712, 2020.

XIA, X. and MOHSENI, K. Unsteady aerodynamics and vortex-sheet formation of a two-dimensional airfoil. **Journal of Fluid Mechanics**, vol. 830, 439–478, 2017.

XU, X. and LAGOR, F.D. Quasi-steady effective angle of attack and its use in lift-equivalent motion design. **AIAA Journal**, vol. 59, n. 7, 2613–2626, 2021.

YANG, J.; DONG, Z.; LIU, Z.; SHI, W.; CHEN, G.; SHAO, T. and ZENG, H. Migration of barchan dunes in the western quruq desert, northwestern china. **Earth Surface Processes and Landforms**, vol. 44, n. 10, 2016–2029, 2019.

YANG, Y. and SOATTO, S. FDA: Fourier Domain Adaptation for Semantic Segmentation. In **2020 IEEE/CVF Conference on Computer Vision and Pattern Recognition (CVPR)**, pp. 4084–4094. 2020.

YE, S.; ZHANG, Z.; SONG, X.; WANG, Y.; CHEN, Y. and HUANG, C. A flow feature detection method for modeling pressure distribution around a cylinder in non-uniform flows by using a convolutional neural network. **Scientific Reports**, vol. 10, n. 1, 4459, 2020.

YOUNG, J.; LAI, J.C.S. and PLATZER, M.F. A review of progress and challenges in flapping foil power generation. **Progress in Aerospace Sciences**, vol. 67, 2–28, 2014.

YU, H.T. and BERNAL, L.P. Effects of pivot location and reduced pitch rate on pitching rectangular flat plates. **AIAA Journal**, vol. 55, n. 3, 702–718, 2017.

YU, Y.; AMANDOLESE, X.; FAN, C. and LIU, Y. Experimental study and modelling of unsteady aerodynamic forces and moment on flat plate in high amplitude pitch ramp motion. **Journal of Fluid Mechanics**, vol. 846, 82–120, 2018.

ZEILER, M.D.; KRISHNAN, D.; TAYLOR, G.W. and FERGUS, R. Deconvolutional networks. In **2010 IEEE Computer Society Conference on Computer Vision and Pattern Recognition**, pp. 2528–2535. 2010.

ZHOU, Y.; FAN, D.; ZHANG, B.; LI, R. and NOACK, B.R. Artificial intelligence control of a turbulent jet. **Journal of Fluid Mechanics**, vol. 897, A27, 2020. A27.

ZHUANG, F.; QI, Z.; DUAN, K.; XI, D.; ZHU, Y.; ZHU, H.; XIONG, H. and HE, Q. A comprehensive survey on transfer learning. **Proceedings of the IEEE**, vol. 109, n. 1, 43–76, 2021.

APPENDIX A - Tensor formalism

In applying a numerical technique to solve the Navier-Stokes equations (or any other physical problem), it is more convenient to represent the equations in a form ideally suited to that particular numerical technique. Hence, we may base ourselves on fundamental principles to cast the equations in a more general form than those dictated by the requirements of an analytical solution.

In order to satisfy conditions on boundaries of arbitrary shape, the generalised curvilinear coordinates are often applied, allowing the direct application of finite difference formulas. Since tensor calculus provides a symbolism which avoids reference to particular coordinate systems, we make use of its formalism to express the equations to be solved numerically. The reader not familiarized with tensor calculus is referred to Synge and Schild (1978) and Aris (1989) for details.

Suppose that x^1, x^2, x^3 are rectangular Cartesian coordinates and let ξ^1, ξ^2, ξ^3 be any system of curvilinear coordinates in a Riemannian space. Hence, we define the covariant and contravariant metric tensors, respectively, as follows

$$g_{ij} \triangleq \frac{\partial x^k}{\partial \xi^i}\frac{\partial x^k}{\partial \xi^j} \quad \text{and} \quad g^{ij} \triangleq \frac{\partial \xi^i}{\partial x^k}\frac{\partial \xi^j}{\partial x^k} \ ,$$

such that

$$\frac{\partial x^i}{\partial \xi^j} = g_{mj}\frac{\partial \xi^m}{\partial x^i} \quad \text{and} \quad \frac{\partial \xi^i}{\partial x^j} = g^{mi}\frac{\partial x^j}{\partial \xi^m} \ .$$

With no loss of generality, we take g_{ij} symmetric, *i.e.* $g_{ij} = g_{ji}$.

The governing equations given by Eqs. 2.1, 2.2 and 2.3 for a curvilinear coordinate system are rewritten respectively as

$$\frac{\partial \rho}{\partial t} + (\rho u^i)_{|i} = 0 \ , \tag{A.1}$$

$$\begin{aligned}\frac{\partial}{\partial t}(\rho u^i) + (\rho u^i u^j + g^{ij}p - \tau^{ij})_{|j} = {} & 2\rho g^{ij}\varepsilon_{jkl}u^k\Omega^l - \rho g_{jk}(\Omega^i\Omega^j\Xi^k - \Xi^i\Omega^j\Omega^k) \\ & + \rho g^{ij}\varepsilon_{jkl}\Xi^k\dot{\Omega}^l - \rho\ddot{\Xi}^i \ ,\end{aligned} \tag{A.2}$$

and

$$\frac{\partial E}{\partial t} + \Big[(E+p)u^j - \tau^{ij}g_{ik}u^k + Q^j\Big]_{|j} = \rho\left(u^j + \hat{\Xi}^j + g^{ij}\varepsilon_{ikl}\Omega^k\Xi^l\right)\left(\ddot{\Xi}^j + g^{jq}\varepsilon_{qrs}\dot{\Omega}^r\hat{\Xi}^s\right) \ , \tag{A.3}$$

where

$$E = \frac{p}{\gamma - 1} + \frac{1}{2}\rho g_{ij}\left[u^i u^j + \left(\dot{\Xi}^i + g^{iq}\varepsilon_{qrs}\Omega^r\Xi^s\right)\left(\dot{\Xi}^j + g^{jl}\varepsilon_{lmn}\Omega^m\Xi^n\right)\right] ,$$

$$Q^j = -\frac{\mu}{\mathrm{Re}\,\mathrm{Pr}} g^{ij} T_{|i} ,$$

and

$$\begin{aligned} \tau^{ij} &= \frac{\mu}{\mathrm{Re}}\left(g^{jk}{u^i}_{|k} + g^{ik}{u^j}_{|k} - \frac{2}{3}g^{ij}{u^k}_{|k}\right) + \frac{\beta}{\mathrm{Re}} g^{ij}{u^k}_{|k} \\ &= \frac{1}{\mathrm{Re}}\left[2\mu S^{ij} + \left(\beta - \frac{2}{3}\mu\right) g^{ij}{u^k}_{|k}\right] , \end{aligned} \tag{A.4}$$

with

$$S^{ij} = \frac{1}{2}\left(g^{jk}{u^i}_{|k} + g^{ik}{u^j}_{|k}\right) .$$

Here, the vertical stroke stands for the covariant derivative. Note that these previous equations are directly obtained from that written in the physical space through the process of lowering and raising of suffixes, and that the Kronecker delta consequently vanishes (*e.g.*, $(pg^{ik}{\delta^j}_k)_{|j} = (g^{ij}p)_{|j}$).

Introducing the Christoffel symbols of the first type

$$[ij, k] = \frac{1}{2}\left(\frac{\partial g_{jk}}{\partial \xi^i} + \frac{\partial g_{ik}}{\partial \xi^j} - \frac{\partial g_{ij}}{\partial \xi^k}\right) ,$$

and of the second type

$$\begin{Bmatrix} k \\ ij \end{Bmatrix} = g^{kp}[ij, p] ,$$

the conservation equations in curvilinear coordinates are read in a non-Euclidian Riemannian space as

$$\frac{\partial \rho}{\partial t} + \frac{\partial}{\partial \xi^i}(\rho u^i) + \begin{Bmatrix} i \\ ik \end{Bmatrix}\rho u^k = 0 ,$$

$$\begin{aligned} &\frac{\partial}{\partial t}(\rho u^i) + \frac{\partial}{\partial \xi^j}(\rho u^i u^j + g^{ij}p - \tau^{ij}) + \begin{Bmatrix} i \\ jk \end{Bmatrix}(\rho u^k u^j + g^{jk}p - \tau^{kj}) + \\ &\begin{Bmatrix} j \\ jk \end{Bmatrix}(\rho u^i u^k + g^{ik}p - \tau^{ik}) = 2\rho g^{ij}\varepsilon_{jkl}u^k\Omega^l - \rho g_{jk}(\Omega^i\Omega^j\Xi^k - \Xi^i\Omega^j\Omega^k) + \\ &\qquad \rho g^{ij}\varepsilon_{jkl}\Xi^k\dot{\Omega}^l - \rho\ddot{\Xi}^i , \end{aligned}$$

and

$$\frac{\partial E}{\partial t} + \frac{\partial}{\partial \xi^j}\left[(E+p)u^j\right] + \begin{Bmatrix} j \\ jk \end{Bmatrix}(E+p)u^k - g_{ik}u^k\left(\frac{\partial \tau^{ij}}{\partial \xi^j} + \begin{Bmatrix} i \\ jl \end{Bmatrix}\tau^{lj} + \begin{Bmatrix} j \\ jl \end{Bmatrix}\tau^{il}\right)$$
$$-\tau^{ij}\left(\frac{\partial}{\partial \xi^j}(g_{ik}u^k) - \begin{Bmatrix} l \\ ij \end{Bmatrix}g_{lk}u^k\right) - \frac{\mu}{\mathrm{Re}\,\mathrm{Pr}}\left[\frac{\partial}{\partial \xi^j}\left(g^{ij}\frac{\partial T}{\partial \xi^i}\right) + \begin{Bmatrix} j \\ jk \end{Bmatrix}g^{ik}\frac{\partial T}{\partial \xi^i}\right] =$$
$$\rho\left(u^j + \hat{\Xi}^j + g^{ij}\varepsilon_{ikl}\Omega^k\Xi^l\right)\left(\ddot{\Xi}^j + g^{jq}\varepsilon_{qrs}\dot{\Omega}^r\hat{\Xi}^s\right) \;,$$

with

$$\tau^{ij} = \frac{1}{\mathrm{Re}}\left[2\mu S^{ij} + g^{ij}\left(\beta - \frac{2}{3}\mu\right)\left(\frac{\partial u^k}{\partial \xi^k} + \begin{Bmatrix} k \\ kl \end{Bmatrix}u^l\right)\right]$$

and

$$S^{ij} = \frac{1}{2}\left[g^{jk}\left(\frac{\partial u^i}{\partial \xi^k} + \begin{Bmatrix} i \\ kl \end{Bmatrix}u^l\right) + g^{ik}\left(\frac{\partial u^j}{\partial \xi^k} + \begin{Bmatrix} j \\ kl \end{Bmatrix}u^l\right)\right] \;.$$

Call $g = \det|g_{ij}| = J^2$, where $J = \det|\partial x^i/\partial \xi^j|$ is the Jacobian. After applying the Voss-Weyl formula for the divergence, the Navier-Stokes equations reduce to

$$\frac{\partial}{\partial t}(g^{1/2}\rho) + \frac{\partial}{\partial \xi^i}(g^{1/2}\rho u^i) = 0 \;, \tag{A.5}$$

$$\frac{\partial}{\partial t}(g^{1/2}\rho u^i) + \frac{\partial}{\partial \xi^j}\left[g^{1/2}\left(\rho u^i u^j + g^{ij}p - \tau^{ij}\right)\right] + \begin{Bmatrix} i \\ jk \end{Bmatrix}g^{1/2}(\rho u^k u^j + g^{jk}p - \tau^{kj}) =$$
$$2g^{1/2}\rho g^{ij}\varepsilon_{jkl}u^k\Omega^l - g^{1/2}\rho g_{jk}(\Omega^i\Omega^j\Xi^k - \Xi^i\Omega^j\Omega^k) + g^{1/2}\rho g^{ij}\varepsilon_{jkl}\Xi^k\dot{\Omega}^l - g^{1/2}\rho\ddot{\Xi}^i \;, \tag{A.6}$$

and

$$\frac{\partial}{\partial t}(g^{1/2}E) + \frac{\partial}{\partial \xi^j}\left\{g^{1/2}\left[(E+p)u^j - \tau^{ij}g_{ik}u^k - \frac{\mu}{\mathrm{Re}\,\mathrm{Pr}}g^{ij}\frac{\partial T}{\partial \xi^i}\right]\right\} =$$
$$g^{1/2}\rho\left(u^j + \hat{\Xi}^j + g^{ij}\varepsilon_{ikl}\Omega^k\Xi^l\right)\left(\ddot{\Xi}^j + g^{jq}\varepsilon_{qrs}\dot{\Omega}^r\hat{\Xi}^s\right) \;. \tag{A.7}$$

with

$$\tau^{ij} = \frac{1}{\mathrm{Re}}\left[2\mu S^{ij} + g^{ij}\left(\beta - \frac{2}{3}\mu\right)\left(\frac{\partial u^k}{\partial \xi^k} + \frac{1}{g^{1/2}}\frac{\partial g^{1/2}}{\partial \xi^k}u^k\right)\right]$$

and

$$S^{ij} = \frac{1}{2}\left[g^{jk}\left(\frac{\partial u^i}{\partial \xi^k} + \begin{Bmatrix} i \\ kl \end{Bmatrix}u^l\right) + g^{ik}\left(\frac{\partial u^j}{\partial \xi^k} + \begin{Bmatrix} j \\ kl \end{Bmatrix}u^l\right)\right] \;.$$

Equations A.5, A.6 and A.7 are the ones solved by our LES code. However, while the use of curvilinear systems with fully tensorial components simplifies the handling of boundary conditions, the presence of an undifferentiated term appearing together with the Christoffel symbol prevents the achievement of overall conservation of mass, momentum and energy in flows with discontinuities. Equation A.6 is, then, said to be in a *weak* conservation-law form, and it would lead to an inferior shock capturing capability Vinokur (1974). This condition can be problematic for dynamic stall applications. That is because the high suction due to the airfoil motion usually induces a rapid and local acceleration of the flow, which can lead to the formation of shock waves even if at low-speed freestream conditions, where the flow field could safely be viewed as incompressible.

Even though we address compressibility effects, our focus is on low-Reynolds aerodynamics. Hence, it is important to pay attention to the fact that shock waves are rarely encountered in realistic applications of low-Reynolds aerodynamics. Another justification for avoiding shock waves here is the fact that they would change the dynamic stall inception mechanisms, making it hard to assess what the phenomenological differences due to Mach number variations actually are. We accomplished this by choosing proper values for the flow conditions and kinematic parameters based on those commonly used in the literature. Nonetheless, it is still valid to discuss the implications of the weak conservation-law form and how we can get around this.

The undifferentiated term in Eq. A.6 is analogous to fictitious centrifugal and Coriolis forces which result from the curvature of the coordinate system, and it is unavoidable if the equation is expressed in a fully tensorial form. However, the existence of a conservation law is related to the isotropicity and homogeneity of the space-time and to the invariance of a given action under the transformation of spatiotemporal coordinates Vinokur (1974). So that, it is a consequence of the underlying symmetries of the system as stated by Noether's theorem.

For generalised coordinate systems, it follows that the metric tensor g_{ij} is forminvariant under infinitesimal transformations $\xi^i \to \xi'^i = \xi^i + \eta^i(\xi^j)$ if there exist a vector η_i that satisfies the Killing equation ($\eta_{r|s} + \eta_{s|r} = 0$). This equation admits six independent solutions, corresponding to the translations and rotations of the flow. Nonetheless, the angular momentum is already conserved for perfect fluids and the rotational Killing vectors may be ignored.

The strong conservation-law form of the momentum equation is obtained by the contraction of the flux tensors with the translational Killing vector such that

$$\begin{aligned}\eta_i \frac{\partial}{\partial t}(\rho u^i) + \eta_i {\Pi^{ij}}_{|j} &= \frac{\partial}{\partial t}(\rho \eta_i u^i) + (\eta_i \Pi^{ij})_{|j} - \eta_{i|j}\Pi^{ij} \\ &= \frac{\partial}{\partial t}(\rho \eta_i u^i) + (\eta_i \Pi^{ij})_{|j} = \eta_i \,(\text{r.h.s.}) \;.\end{aligned}$$

In this case, we choose η_i as the basis vector of the transformation, $\eta_i = \mathbf{g}_i$, with $\mathbf{g}_i$ satisfying $g_{ij} = \mathbf{g}_i \cdot \mathbf{g}_j$. Moreover, $\mathbf{g}_i$ is related to the Cartesian quantities by $\mathbf{g}_i =$

$\partial x^j/\partial \xi^i \, \mathbf{e}_j$, where $\mathbf{e}_j$ forms the basis of the Cartesian system. Hence, we are left with

$$\frac{\partial}{\partial t}\Big(g^{1/2}\rho\mathbf{u}\Big) + \frac{\partial}{\partial \xi^j}\Big[g^{1/2}\Big(\rho\mathbf{u}u^j + \mathbf{g}^j p - \mathbf{g}_i\,\tau^{ij}\Big)\Big] = 2\,\mathbf{g}_i\,g^{1/2}\rho g^{ij}\varepsilon_{jkl}u^k\Omega^l - \\ \mathbf{g}_i\,g^{1/2}\rho g_{jk}(\Omega^i\Omega^j\Xi^k - \Xi^i\Omega^j\Omega^k) + \mathbf{g}_i\,g^{1/2}\rho g^{ij}\varepsilon_{jkl}\Xi^k\dot{\Omega}^l - \mathbf{g}_i\,g^{1/2}\rho\ddot{\Xi}^i \ , \qquad \text{(A.8)}$$

where $\mathbf{u} = u^i\mathbf{g}_i = u^i\,\partial x^j/\partial\xi^i\,\mathbf{e}_j$ is the Cartesian velocity vector and $\mathbf{g}^j = \partial\xi^j/\partial x^i\,\mathbf{e}^i$.

The viscous term in Eq. A.8 is written, in terms of the Cartesian components, as

$$\tau^{ij} = \frac{1}{\mathrm{Re}}\left[2\mu S^{ij} + \left(\beta - \frac{2}{3}\mu\right)g^{ij}\frac{\partial\mathbf{u}}{\partial\xi^k}\cdot\mathbf{g}^k\right] \ ,$$

with

$$S^{ij} = \frac{1}{2}\left(g^{jk}\frac{\partial\mathbf{u}}{\partial\xi^k}\cdot\mathbf{g}^i + g^{ik}\frac{\partial\mathbf{u}}{\partial\xi^k}\cdot\mathbf{g}^j\right) \ .$$

When deriving the viscous term above, we used the fact that $u^j = \mathbf{u}\cdot\mathbf{g}^j$ and that

$$\frac{\partial\mathbf{g}^j}{\partial\xi^k} = -\begin{Bmatrix} j \\ kl \end{Bmatrix}\mathbf{g}^l \ .$$

The resulting equation might be analagous to momentum equation usually employed in CFD codes written in the generalized curvilinear form.

Instead of solving for Eq. A.8, we rewrite this equation in contravariant form since it is more suitable for the staggered grid implementation. Hence, we have that

$$\frac{\partial}{\partial t}\Big(g^{1/2}\rho u^m\Big) + \mathbf{g}^m\cdot\frac{\partial}{\partial\xi^j}\Big[\mathbf{g}_i\,g^{1/2}\Big(\rho u^i u^j + g^{ij}p - \tau^{ij}\Big)\Big] = 2\,g^{1/2}\rho g^{mj}\varepsilon_{jkl}u^k\Omega^l - \\ g^{1/2}\rho g_{jk}(\Omega^m\Omega^j\Xi^k - \Xi^m\Omega^j\Omega^k) + g^{1/2}\rho g^{mj}\varepsilon_{jkl}\Xi^k\dot{\Omega}^l - g^{1/2}\rho\ddot{\Xi}^m \ , \quad \text{(A.9)}$$

where the viscous stress and the strain rate tensors are evaluated, respectively, as

$$\tau^{ij} = \frac{1}{\mathrm{Re}}\left[2\mu S^{ij} + \left(\beta - \frac{2}{3}\mu\right)g^{ij}u^k{}_{|k}\right] \ , \qquad \text{(A.10)}$$

and

$$S^{ij} = \frac{1}{2}\left(g^{jk}u^i{}_{|k} + g^{ik}u^j{}_{|k}\right) \ .$$

APPENDIX B - Analysis of vorticity transport for the periodic motion

In this section, we assess how vorticity is affected by compressibility effects during the onset and development of dynamic stall. To this end, we consider the periodic case of Chapter 3 since it is there that the dynamic stall onset is discussed in depth. Assuming a constant viscosity, which is reasonable for the present investigations at low and moderate Mach numbers, the vorticity transport equation for a compressible flow is given by

$$\begin{aligned}\frac{D\omega_i}{Dt} &= \frac{\partial \omega_i}{\partial t} + u_j \frac{\partial \omega_i}{\partial x_j} \\ &= \omega_j \frac{\partial u_i}{\partial x_j} - \omega_i \frac{\partial u_j}{\partial x_j} - \varepsilon_{ijk} \frac{\partial}{\partial x_j}\left(\frac{1}{\rho}\right)\frac{\partial p}{\partial x_k} + \frac{\mu}{\rho}\frac{\partial^2 \omega_i}{\partial x_j \partial x_j} + \varepsilon_{ijk}\frac{\partial}{\partial x_j}\left(\frac{1}{\rho}\right)\frac{\partial \tau_{lk}}{\partial x_l}. \qquad \text{(B.1)}\end{aligned}$$

Here, the terms appearing in the right hand side of the vorticity equation are, respectively, vortex stretching, volumetric dilatation, baroclinic torque, viscous diffusion and shear stress-density gradient torque. In compressible flows, density inhomogeneities may yield the generation/destruction of vorticity due to possible additional rotation being created as inertial forces accelerate fluid elements of different densities. This effect is represented by the baroclinic term, which arises from the misalignment of the material acceleration (via pressure gradient) and density gradient vectors. Also, another two extra terms exist compared to the incompressible case, being the volumetric dilatation and the shear stress-density gradient torque. The contributions of the individual terms appearing in Eq. B.1 are investigated here and presented in Figs. B.1 and B.2, in which we highlight time instants at the onset of dynamic stall and during its transport over the airfoil suction side. Note that the spanwise averaged results do not facilitate an explicit accounting of the vortex stretching term that affects the 3D results and is hence not considered. We also leave the convection term out to focus only on those terms that act as sources and sinks in a Lagrangian description of the vorticity evolution. With the aim to better visualize the contributions to the vorticity field, the z-vorticity contours are also plotted in both figures, resulting in the shaded green and pink regions appearing in the subplots. These regions indicate positive (pink) and negative (green) z-vorticity and can be better visualized in the plot of shear stress-density gradient (far right), since this latter term is almost nonexistent in the present contour scales, leaving the shaded contours clearer. All source (sink) terms are plotted in red (blue) colors on top of the z-vorticity contours.

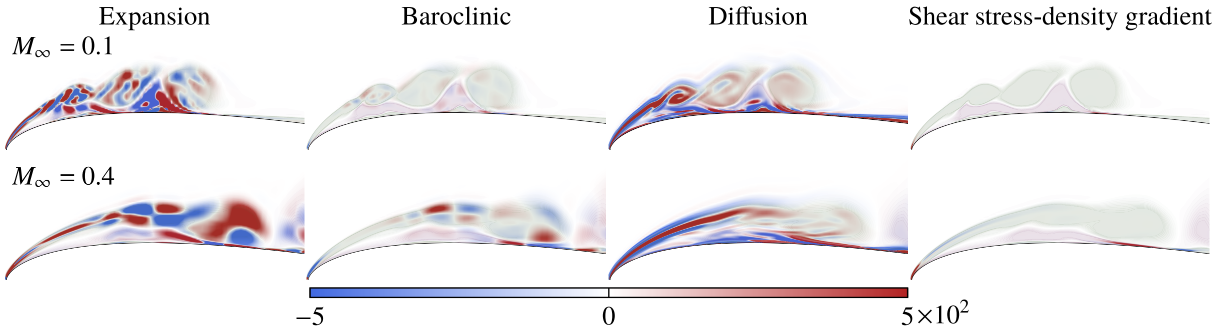

Figure B.1: Vorticity transport in the leading-edge region ($x/c \leq 0.25$) at $t = 4.6$ for $M_\infty = 0.1$ (top) and $M_\infty = 0.4$ (bottom). Green and pink contour shades indicate negative and positive fields of z-vorticity, respectively.

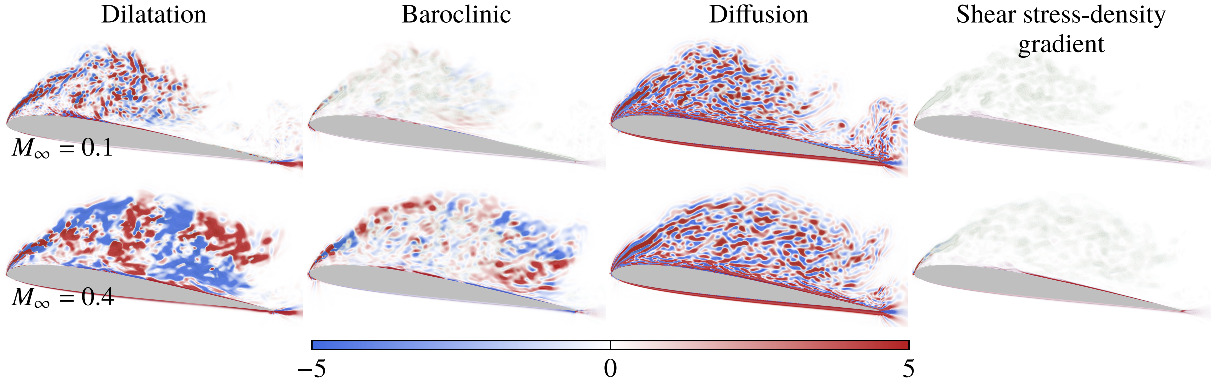

Figure B.2: Vorticity transport at $t = 6.5$ for $M_\infty = 0.1$ (top) and $M_\infty = 0.4$ (bottom). Green and pink contours indicate negative and positive fields of z-vorticity, respectively.

From Fig. B.1, we see that the dilatation and diffusion terms dominate the evolution of vorticity for the lower Mach number case. While the former appears due to compressibility effects, the latter is related to incompressible mechanisms. The dilatation term is composed of small scale structures inside the shear layer and the diffusion term is smoother, being more relevant near the wall and along the thin shear layer at the leading edge. A similar behavior is observed for the higher Mach number flow but the spatial scales in the dilatation term are larger for this case. When compressibility is increased, the impact of the baroclinic torque also becomes more relevant. For $M_\infty = 0.4$, this term opposes that due to dilatation, indicating that the former acts as a stabilizing term for the latter. A comparison of the diffusion terms, on the other hand, shows that the diffusion levels are similar for both Mach numbers and concentrated either in the viscous interface aft of the airfoil leading edge or in localized spots near the wall. This indicates that the primary role of viscous diffusion is to transport vorticity from the higher vorticity regions to the outside irrotational flow or to the zero vorticity line. Finally, the shear stress density gradient has a negligible contribution to the spanwise vorticity, as shown in the figure.

Figure B.2 presents the spatial distribution of the vorticity sources and sinks at a later time instant. Here, the DSV is already formed, being transported over the airfoil. Compressibility impacts the behavior of the dilatation term considerably. For the lower Mach number case, it is composed of more isotropic small-scale fluctuations while, for the higher Mach number flow, fluctuations show a more coherent pattern with larger structures. As previously noted, the baroclinic torque is pronounced only for the higher Mach number case. For this term, coherent patterns are observed along the boundaries of the DSV and they are in phase opposition with the vorticity dilatation. The diffusion term is composed of isotropic fluctuations along the entire DSV independently of compressibility, and the shear stress-density gradient again has a negligible impact on the vorticity evolution. The present analysis of the sources and sinks of vorticity facilitates a further assessment of compressibility effects on the onset and evolution of the dynamic stall vortex.

APPENDIX C - Analysis of non-inertial forces

In Chapter 4, the equivalence between pitch and plunge was investigated under constant ramp motions. While for plunging motion there exists only the translational acceleration, the constant rate pitching cases are directly affected by Coriolis and centripetal accelerations. For this reason, it is important to discern how each pseudo-force contributes to the flow dynamics. To this end, consider the material derivative of the velocity $\boldsymbol{u}'$ of a fluid particle, which is written as

$$\frac{\mathrm{D}\boldsymbol{u}'}{\mathrm{D}t} = \frac{\mathrm{D}\dot{\boldsymbol{x}}'}{\mathrm{D}t} = \ddot{\boldsymbol{x}}' = \frac{\partial \dot{\boldsymbol{x}}'}{\partial t} + \boldsymbol{\omega}' \wedge \dot{\boldsymbol{x}}' + \operatorname{grad} \tfrac{1}{2}\dot{x}'^2 \ . \tag{C.1}$$

This expression is valid for either a moving or a stationary frame, provided that all quantities are measured in relation to that frame (in a fixed frame, the quantities would not be primed). In practical applications, it is desired to measure forces apparent to observers stationary with respect to the airfoil, which is in relative motion to the reference (fixed) frame. In this case, $\ddot{\boldsymbol{x}}$ must include quantities measured at the two distinct frames, which are in relative motion. To do that, let Cartesian axes be employed in each frame and primes denote quantities associated with the airfoil system (moving frame). Let $\boldsymbol{X}$ and $\boldsymbol{\Omega}$ denote the position and angular velocity of the airfoil, respectively. Then, the accelerations can be compared for the two frames as

$$\ddot{\boldsymbol{x}} = \frac{\partial \dot{\boldsymbol{X}}}{\partial t} + \frac{\partial \boldsymbol{\Omega}}{\partial t} \wedge \boldsymbol{x}' + \boldsymbol{\Omega} \wedge (\boldsymbol{\Omega} \wedge \boldsymbol{x}') + 2\boldsymbol{\Omega} \wedge \dot{\boldsymbol{x}}' + \ddot{\boldsymbol{x}}' \ . \tag{C.2}$$

Assuming that the moving frame does not have linear and rotational accelerations, i.e., $\partial \dot{\boldsymbol{X}}/\partial t = 0$ and $\partial \boldsymbol{\Omega}/\partial t = 0$ (this represents our constant-ramp pitching airfoil), and substituting the term $\ddot{\boldsymbol{x}}'$ from Eq. C.1 in Eq. C.2, we have

$$\ddot{\boldsymbol{x}} = \frac{\partial \dot{\boldsymbol{x}}'}{\partial t} + (\boldsymbol{\omega}' + 2\boldsymbol{\Omega}) \wedge \dot{\boldsymbol{x}}' + \operatorname{grad} \tfrac{1}{2}[\dot{x}'^2 + (\boldsymbol{\Omega} \cdot \boldsymbol{x}')^2 - \Omega^2 x'^2] \ . \tag{C.3}$$

Thus, the acceleration for an observer at the moving frame (Eq. C.1) has the same form as that in a inertial frame (Eq. C.3). To obtain this expression, we use the fact that the centrifugal acceleration is independent of the flow and conservative, which implies that $\boldsymbol{\Omega} \wedge (\boldsymbol{\Omega} \wedge \boldsymbol{x}') = \operatorname{grad} \phi_c$. The term $\phi_c = \frac{1}{2}[(\boldsymbol{\Omega} \cdot \boldsymbol{x}')^2 - \Omega^2 x'^2]$ is the centrifugal potential and it acts in the sense of reducing the apparent squared speed $\dot{x}'^2$, since $\phi_c \leq 0$. The vector $\boldsymbol{\omega}' + 2\boldsymbol{\Omega} = \boldsymbol{\omega}$ is the absolute vorticity, which indicates that the apparent local angular velocity $\frac{1}{2}\boldsymbol{\omega}'$ is increased by $\boldsymbol{\Omega}$.

The centrifugal potential can be absorbed into an equivalent pressure term ($p_e =$

$p + \rho\,\phi_c)$ in the Navier-Stokes equations and, since $\phi_c \leq 0$, it reduces the equivalent pressure. Since the centrifugal term acts as a potential forcing, it does not generate vorticity directly, but rather alters the vorticity distribution and strength of the DSV through pressure variations.

The Coriolis force, on the other hand, generates a non-conservative field. To better understand how the Coriolis acceleration $\boldsymbol{a}' = -2\boldsymbol{\Omega} \wedge \dot{\boldsymbol{x}}'$ serves as an internal source of relative vorticity, let us consider the rate of change of circulation of a closed material surface $\mathcal{S}$. Knowing that $\operatorname{curl} \boldsymbol{a}' = -2\boldsymbol{\mathcal{D}}' \cdot \boldsymbol{\Omega}$, where $\boldsymbol{\mathcal{D}}' = \mathbf{I} \operatorname{div} \dot{\boldsymbol{x}}' - (\operatorname{grad} \dot{\boldsymbol{x}}')^{\mathrm{T}}$ is the surface deformation-rate tensor (Wu *et. al*, 2006), the Stokes theorem yields

$$\frac{\mathrm{d}\Gamma'}{\mathrm{d}t} = \int_{\mathcal{S}} \operatorname{curl} \boldsymbol{a}' \cdot \mathrm{d}\boldsymbol{S} = -2\boldsymbol{\Omega} \cdot \int_{\mathcal{S}} \mathrm{d}\boldsymbol{S} \cdot \boldsymbol{\mathcal{D}}' \ , \tag{C.4}$$

where $\mathrm{d}\boldsymbol{S}$ is the material surface element, with normal pointing outward. To evaluate this integral, we rely on the kinematics of surface integrals. According to Truesdell (1954), the material derivative of the flux of an arbitrary continuously differentiable tensor field $\boldsymbol{\Phi}'$ across a material surface $\mathcal{S}$ is given by

$$\frac{\mathrm{D}}{\mathrm{D}t} \int_{\mathcal{S}} \mathrm{d}\boldsymbol{S} \cdot \boldsymbol{\Phi}' = \int_{\mathcal{S}} \left[\mathrm{d}\boldsymbol{S} \cdot \left(\dot{\boldsymbol{\Phi}}' + \boldsymbol{\Phi}' \operatorname{div} \dot{\boldsymbol{x}}' \right) - \operatorname{grad} \dot{\boldsymbol{x}}' \cdot \mathrm{d}\boldsymbol{S} \cdot \boldsymbol{\Phi}' \right] \ .$$

By taking $\boldsymbol{\Phi}'$ as the identity matrix $\mathbf{I}$, we get

$$\frac{\mathrm{D}}{\mathrm{D}t} \int_{\mathcal{S}} \mathrm{d}\boldsymbol{S} = \int_{\mathcal{S}} \mathrm{d}\boldsymbol{S} \cdot \left[\mathbf{I} \operatorname{div} \dot{\boldsymbol{x}}' - (\operatorname{grad} \dot{\boldsymbol{x}}')^{\mathrm{T}} \right] = \int_{\mathcal{S}} \mathrm{d}\boldsymbol{S} \cdot \boldsymbol{\mathcal{D}}' \ . \tag{C.5}$$

Substituting Eq. C.5 into C.4 leads to

$$\frac{\mathrm{d}\Gamma'}{\mathrm{d}t} = -2\boldsymbol{\Omega} \cdot \frac{\mathrm{D}}{\mathrm{D}t} \int_{\mathcal{S}} \mathrm{d}\boldsymbol{S} = -2\boldsymbol{\Omega} \cdot \frac{\mathrm{d}\boldsymbol{S}}{\mathrm{d}t} = -2\Omega \frac{\mathrm{d}\mathcal{S}_{\perp}}{\mathrm{d}t} \ , \tag{C.6}$$

where $\boldsymbol{S}$ is the material surface spanned by the closed circulation loop, and $\mathcal{S}_{\perp}$ is the area enclosed by the projection of $\boldsymbol{S}$ upon a plane perpendicular to $\boldsymbol{\Omega}$.

In the present two-dimensional problem, one can think, for example, of a cylindrical surface over the airfoil with its end caps. Then, the projected surface would be a circular region surrounding the airfoil. Since the projected material surface $\mathcal{S}_{\perp}$ changes in time due to velocity variations along the airfoil in the non-inertial frame of reference, Eq. C.6 establishes that a variation in the circulation will occur inside the closed region.

The rationale behind the analysis of the non-inertial terms is that if pitch and plunge are equivalent, then these non-inertial contributions should also be similar between the two constructed motions. The opposite also holds; if the equivalence breaks, then different pseudo-forces should be driving the flow to different states. However, despite acting as a source of net vorticity, we observed that the contribution of the Coriolis force to the momentum equation is negligible (not shown here). In fact, all pseudo-forces (translational, Coriolis and centrifugal) were found to be relatively small. This fact suggests that the differences between pitch and plunge cannot be directly explained in terms of these pseudo-forces, which is quite intriguing as the only differences between these two classes of motion reside fundamentally in the non-inertial terms. In Chapter 4, we discussed that the trailing-edge system differs between pitch and plunge, but the cause of such discrepancies is not yet fully understood. For this reason, this topic deserves further investigation.

APPENDIX D - Barchan dunes

Barchan dunes, or simply barchans, are crescent-shaped dunes resulting from the transport of grains, usually sand, by a one-directional fluid flows in a mode of transport called bedload (Charru *et. al*, 2013). Their migratory behavior occurs in different environments and scales and may pose risks to human activity with regard to the accretion on roads, railways and communication lines (Dong *et. al*, 2000, 2004). Due to its ubiquitous nature and impact on the landscape, the morphodynamics of barchans has been the subject of research through field measurements on Earth (Sauermann *et. al*, 2000; Yang *et. al*, 2019; Bourke, 2010) and Mars (Bourke, 2010; Schatz *et. al*, 2006; Runyon *et. al*, 2017). But often, these measurements involve large time and length scales and uncontrolled conditions, which makes it difficult to track the evolution of the bedform over a long period of time. Moreover, thus far, little information can be extracted from Aeolian and Martian barchans at the grain scale.

Given the smaller and faster scales of subaqueous barchans, the initial and long-time evolution of the barchan morphology (Hersen *et. al*, 2002; Runyon *et. al*, 2017) and the typical trajectories and velocities of moving grains (Alvarez and Franklin, 2018; Wenzel and de Moraes Franklin, 2019; Alvarez and Franklin, 2019) could be obtained from controlled experimental studies carried out in water channels and tanks. Such level of understanding of how dunes perform at smaller scales is crucial to improving dune models that couple local sand motion with turbulent flow across a complex topography (Assis and Franklin, 2021). In addition to experiments in water, numerical simulations have also been employed to address grain scale dynamics. Kidanemariam and Uhlmann (2014, 2017) used direct numerical simulations (DNS) to fully solve the flow around each grain, being the most accurate representation of the physics where sediment transport takes place. However, in their method, the time required for obtaining developed barchans is seldom reached due to the exceedingly high computational cost involved (Colombini, 2014). In recent work, Alvarez and Franklin (2020, 2021) used LES to compute the flow around dunes at a much lower computational cost. Not only they were able to accurately reproduce previous experimental data, but also the numerical results revealed quantities not accessible from experiments, such as the resultant force acting on each grain. These forces represent an important step towards a realistic representation of fluid-sediment interactions and can, in principle, support or invalidate existing models down to the grain scale.

In this part of the work, we propose a framework whereby numerical simulation data is leveraged to extract relevant information from experimental visualizations of barchans.

To this end, we uniquely treat the image semantic segmentation as an image-to-image translation task that infers semantic labels of structures from the input images in a supervised way. Particularly, given the source domain of numerically simulated images of dune morphology, we train a U-net (Ronneberger *et. al*, 2015) to generate synthetic force distribution at the grain scale. Then, global photometric statistics of experimental images are manipulated using the Fourier Domain Adaptation method proposed by Yang and Soatto (2020) to improve the alignment of the low-level statistics between the source and target distributions. This is especially important since the networks do not transfer well across different low-level statistics (Achille *et. al*, 2019).

The U-net was trained for 103 epochs yielding a loss of 0.0023 with mean squared error of 0.0047 and a validation loss of 0.0033 with mean squared error of 0.0067. Our dataset contains nearly 1800 images devided into train (1400 images), validation (160) and test (180) sets. Some results performed on the test set are displayed on Fig. D.1. The agreement between the predicted and annotated forces suggests that our simple encoder-decoder model is effective at managing the categorical interpretation of the barchan dunes. We believe that some defective regions in the synthetic images can be improved by increasing the number of training data or applying a more complex network.

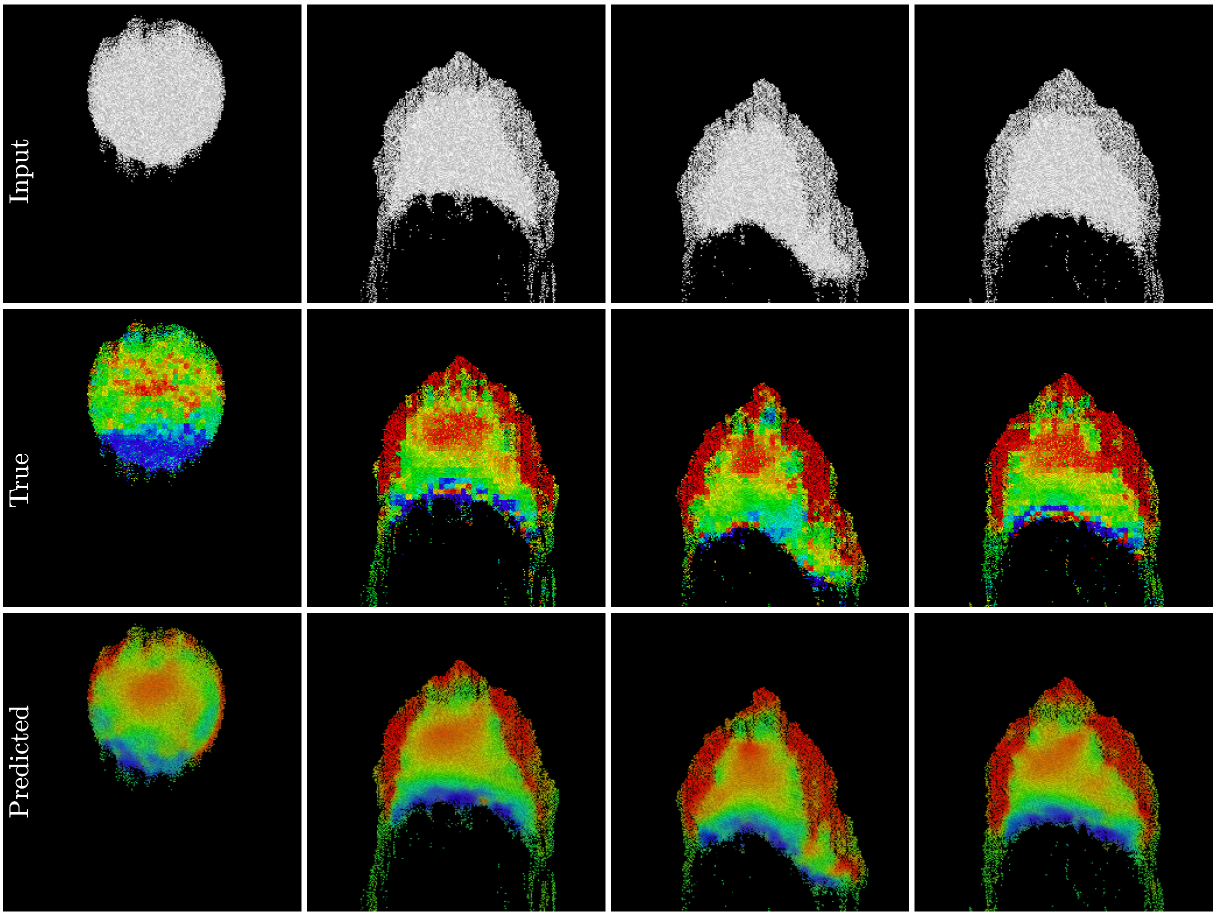

Figure D.1: Dune morphology (first row), the corresponding force distribution (middle row) and that predicted by the CNN (bottom row).